Thermal Effects on the Rotating Neutron Stars

THESIS

Submitted in partial fulfillment
of the requirements for the degree of
DOCTOR OF PHILOSOPHY

By

KRISHNA PRAKASH NUNNA
ID No. 2015PHXF0015H

Under the supervision of

Prof. SARMISTHA BANIK

BITS Pilani
Pilani | Dubai | Goa | Hyderabad

BIRLA INSTITUTE OF TECHNOLOGY AND SCIENCE, PILANI
September 2020

BIRLA INSTITUTE OF TECHNOLOGY AND SCIENCE, PILANI

Certificate

This is to certify that the thesis titled "**Thermal Effects on the Rotating Neutron Stars**" submitted by KRISHNA PRAKASH NUNNA, ID No. 2015PHXF0015H for award of Ph.D. of the Institute embodies original work done by him under my supervision.

Sarmistha Banik

Signature of Supervisor
Prof. SARMISTHA BANIK
Associate Professor,
Birla Institute of Technology and
Science-Pilani,
Hyderabad Campus
Date: 18.9.2020

Acknowledgements

Firstly, I would like to express my sincere gratitude to my supervisor Prof. Sarmistha Banik for the continuous support during my PhD tenure and related research. Her research experience helped me to choose and solve research problems effectively.

Besides my supervisor, I would like to thank my Doctoral Advisory Committee members: Prof. Thiruvikraman and Dr. Sashideep Gutti for their insightful comments and encouragement.

My sincere thanks also goes to Prof. Debades Bandyopadhyay, Prof. Debarati Chatterjee, Dr. Neelam Dhanda and Dr. Somnath Mukhopadyay who helped me in broadening my thinking with stimulating discussions.

I thank my colleagues Dr. Smruti Smitha Lenka, Dr. Nagendra Prasad, Mr. Veera Reddy, Mr. Ravi Teja, Mr. Rahul Thakur, Mr. Sateesh for interesting conversations, sharing knowledge, and for all the fun we have had in the last five years.

I would like to thank Prof Subash N. Karbelkar, Dr. Satyanarayana Murthy, Mr. Upender Reddy, Mr. Shaik Shukur. They helped me to understand the experiments in the undergraduate Physics laboratory.

I would like to thank my Institute BITS-Pilani, Hyderabad campus for giving me an opportunity to carry out my research work.

Last but not the least, I would like to thank my family: my parents and sister for supporting me continuously throughout writing this thesis and my life in general.

Thank you

Krishna Prakash Nunna

Abstract

Neutron stars are believed to be born in supernova explosions triggered by the collapse of the iron core in massive stars. Almost all physical properties of neutron stars are extreme compared to other objects in the universe except black hole. Mass of the Neutron star ranges from one to two solar mass and the radius is around R $\sim$ 10 kms. Matter density inside the core of a neutron star is a few times the normal nuclear matter density $2.7 \times 10^{14} g/cm^3$. Because of such high densities at center of the core, apart from nucleons(neutrons and protons) other exotic matter such as Bose-Einstein condensation of antikaons(K^-) mesons and hyperons may exist.

First of all we consider a neutrino-free hot neutron star that contains antikaon condensates in its core and is at finite entropy per baryon. We find the equation of state(EoS) for a range of entropies and antikaon optical potentials and generate the mass profile of static as well as rotating stars. We construct the EoS in the frame work of relativistic mean field(RMF) model with density dependent couplings(DD2). Rotation induces many changes in the stellar equilibrium, and hence its structural properties evolve. We estimate the properties of rotating hot neutrons by constructing equilibrium sequences at constant angular momentum. We report the effect of rotation on the mass and shape of a hot neutron star for different EoS and thermodynamic conditions. Temperature profile of hot, static neutron star is also explored. We also make a crude estimate of the amplitude of gravitational waves emitted by an axisymmetric rotating NS with high magnetic field.

Next we estimate the properties of differentially rotating neutron star. One of the probable remnants of binary neutron star merger is a differentially rotating hot hypermassive neutron star. The stability of the merger remnant depends crucially on the underlying EoS and thus provides a method to probe the nature of dense matter in NSs. In this work, we search for possible signatures of strangeness containing matter in the NS interior on the secular stability of the merger remnant. We also use recently proposed methods to make a rough estimate the collapse time of the merger remnant and the threshold mass above which the merger promptly collapses to a black hole.

Contents

List of Tables

List of Figures

Abbreviations

a	Degree of differential rotation
AXMSP	Accreting X-ray milli second Pulsars
BGSM	Bonazzola, Gourgoulhon, Salgado, & Marck
BH	Black Hole
CCSN	Core Collapse Supernovae
cm	Centimetre
DD	Density Dependent
EoS	Equation of State
g	gram
GR	General Relativity
GRB	Gamma Ray Burst
GRV2 & GRV3	General Relativistic Virial identities
GW	Gravitational Waves
Hz	Hertz
HMNS	Hyper massive neutron star
KEH	Komatsu, Eriguchi, & Hachisu
kg	Kilogram
km	Kilometre
LIGO	Laser Interferometer Gravitational-Wave Observatory
LORENE	Langage Objet pour la Relativité NumériquE
m	metre
MeV	Mega electron Volt
MM	Multi-messenger
MSP	Milli second pulsars
NICER	Neutron star Interior Composition Explorer

NS	Neutron Star
PNS	Protoneutron Star
PSR	Pulsar
RMF	Relativistic Mean Field
s	Entropy per baryon
TOV	Tolman Oppenheimer Volkoff
TP	Turning Point
T/W	Ratio of Kinetic energy to Gravitational potential energy of the rotating star
ZAMO	Zero Angular Momentum Observers

Physical Constants

Boltzmann Constant	k_B	$=$	1
Gravitational Constant	G	$=$	1
Speed of Light	c	$=$	1
Solar Mass	M_{solar}	$=$	2×10^{30}kg

Chapter 1

Introduction

1.1 Birth of the Neutron Stars

After the discovery of neutron, Landau in the year 1932 proposed the existence of stars made of neutrons. In 1934 Fritz Zwicky and Walter Baade [1] speculated that neutron stars (NS) might be formed in Type II supernova explosions. Five years later Oppenheimer and Volkoff estimated maximum mass of the NS to be around $0.7M_{solar}$. In 1967 Jocelyn Bell and Anthony Hewish discovered the first pulsar, an object in the outer space that emits very regular pulses of radio energy. A year later Gold [2] proved that rotating pulsar indeed is a neutron star with magnetic field.

NSs are the one of the densest objects in the universe. They are ideal astrophysical laboratories for testing theories of dense matter physics and provide connections among nuclear physics, particle physics and astrophysics. They are created in the gravitational core collapse of the massive stars ($8M_{solar} \sim 10M_{solar}$) at the end of their lifetime. How a main sequence star comes to supernova phase is interesting. Main sequence stars are born as a result of gravitational collapse of molecular hydrogen clouds. As a result of compression, density and temperature increase creating thermal pressure gradient which balances gravity. During the process of compression, temperature rises to the ignition point, where hydrogen fuses into helium; thus releasing large amount of energy to balance gravitational contraction. When all the hydrogen gets converted into helium, the core starts contracting. As a result temperature rises again so that fusion of helium into carbon starts. This cycle of fusion, converting elements with lower atomic number into ones with higher atomic number continues till the core reaches iron. Now iron being one of the tightly bound of all nuclei, the fusion stops. No further energy is released to arrest the gravitational contraction. Hence, the core contracts under its own gravity raising the temperature, paving the way for γ-rays production, which can photo-disintegrate iron nuclei

as

$$\begin{aligned} {}^{56}Fe + \gamma &\rightarrow 13\,{}^{4}He + 4n \\ {}^{4}He + \gamma &\rightarrow 2p + 2n. \end{aligned} \tag{1.1}$$

Free electrons combine with protons to form neutrons and electron neutrinos. As the density inside core rises to a value $\sim 10^{12} g/cm^3$ neutrinos get trapped, as their diffusion time becomes larger than collapse time. When baryon density reaches nuclear saturation density($\sim 10^{14} g/cm^3$), neutrons become degenerate. At this stage collapse is halted, due to repulsive nuclear interaction along with thermal pressure, where the temperature is around $T \sim 50$ MeV. The infalling core material rebounds from the stiffened core sending a shock wave originating from the interior of core. As the shock moves in outward direction, it loses its energy to neutrinos and by photo-disintegration of all nuclei on the way. The shock gets stalled after traveling a few hundred kilometers from the core. The infalling matter from outer layers gets arrested because of the stalled shock front turning the latter into an accretion shock. The infalling matter heats the region of the accretion shock. As the trapped neutrinos diffuse out, a fraction of them interacts with the top layers of the atmosphere, heating the accreting matter, eventually depositing enough energy to re-ignite the shock and successfully drive the explosion. If the remnant core exceeds the Chandrasekhar limit, it collapses to a black hole (BH). Otherwise a neutron star(NS) is born.

1.2 NS Equation of state

NS encompasses a wide range of densities from the density of iron nucleus at the crust of it to several times normal nuclear matter density in the core. The relationship between pressure, density, and temperature is described by the equation of state (EoS) of dense matter. The structure of NSs is usually studied by modeling the homogeneous matter of the core by a suitable EoS, based on a many-body theory or relativistic mean field theory, and the crust by a functional based on a more phenomenological approach. We discuss how the crust and core of a NS is modeled.

1.2.1 Crust

Neutron star crust can be divided into two parts - outer and inner crusts. The outer crust spans over the density range from $10^4 g/cm^3$ to $\sim 10^{11} g/cm^3$ and is composed of nuclei and electrons. Outer crust theoretical modeling was done by Baym, Pethick, and Sutherland (BPS)[3]. The procedure to estimate equilibrium nuclei in the crust is as follows: Nuclei are arranged in a lattice to minimize the coulomb interaction. The Wigner-Seitz approximation is adopted in this calculation. Each lattice volume is replaced by a spherical cell and contains one nucleus at the

center. Each cell is taken to be charge neutral such that Z number of electrons are present in it. The Coulomb interaction between cells is neglected. To find an equilibrium nucleus (A,Z) at a given pressure P one has to minimize the Gibbs free energy per nucleon with respect to mass number A and atomic number Z. A sequence of nuclei starting from ^{56}Fe are found in this process. As density increases, the nuclei become more and more neutron rich. The edge of the outer crust is defined when neutrons drip out of nuclei as the neutron chemical potential equals to bare neutron mass.

The inner crust extends from the neutron drip density upto the density at which the matter becomes uniform. The inner crust is composed of nuclei immersed in neutron and electron gas. The matter is β-equilibrated and charge neutral and the nuclei are also in mechanical equilibrium with the neutron gas. In this density regime, the system displays rich and complex structures which result from the competition between nuclear and coulomb interactions. The matter is highly non-uniform in neutron star crusts. Neutron-rich nuclear clusters dissolve into neutrons and protons to produce a uniform nuclear matter, at the crust-core interface where the matter density is $\sim 2.7 \times 10^{14} g/cm^3$ [4].

Below this density, matter consists of light and heavy nuclei together with unbound but interacting nucleons. Such a low temperature ($\sim$ 10 MeV) matter can be described by nuclear statistical equilibrium (NSE) model [5] where the nuclear chemical equilibrium is regulated by the modified the Saha equation. The thermodynamic quantities such as pressure, energy density, etc., are obtained from the total canonical partition function given by,

$$Z(T, V, \{N_i\}) = Z_{nuc} \prod_{A,Z} Z_{A,Z} \; Z_{Coul} \tag{1.2}$$

with V denoting the volume of the system. The Helmholtz free energy has contribution from nucleons, nucleus and Coulomb interaction and is obtained from the partition function as $F(T, V, \{N_i\}) = -T \ln Z$. Finally, one can write the expressions of number density, pressure and energy density [5].

1.2.2 Core

Outer core has density range $0.5\rho_0 \leq \rho \leq 2\rho_0$, where ρ_0 is the normal nuclear matter density 2.7×10^{14} g/cm^3. Its matter consists of neutrons(n) with a small per cent admixture of protons (p), electrons (e), and possibly muons (μ). The state of this matter is determined by the conditions of electric neutrality and β equilibrium, supplemented by a microscopic model of many-body nucleon interaction.

The matter inside the core of a neutron star is super dense. Here, the baryon number density (n_B) can reach up to a few times of normal nuclear matter density (n_0), which is unlike anything

found on Earth. The behaviour of matter up to nuclear densities has been studied and is well documented by numerous nuclear physics experiments. Lack of experimental data at higher matter densities means we do not completely understand the properties of matter at super nuclear densities. Consequently, there exist huge uncertainties in understanding the behaviour of matter at high densities such as those present in NS cores.

At this density an equilibrium mixture of neutrons, protons, and electrons is expected to exist. The reactions which lead to the β-equilibrium in the system are,

$$n \rightarrow p + e^{-} + \bar{\nu_e} \tag{1.3}$$

$$p + e^{-} \rightarrow n + \nu_e \tag{1.4}$$

Further Neutrinos escape freely from the star. Therefore, the condition of chemical equilibrium is,

$$\mu_n = \mu_e + \mu_p. \tag{1.5}$$

Exotic Matter in the NS core

The major constituents of matter with density just below n_0, are protons, neutrons and leptons. The interior composition of NSs is still a mystery, as the nature of cold and dense matter beyond saturation density is not accessible to terrestrial experiments, and one must resort to theoretical models for their description. While nuclear experiments provide clues about the nature of matter close to nuclear matter saturation density n_0, heavy ion collisions provide information about hot and dense matter at a few times n_0. Although such experiments can help to constrain parameters of theoretical models, they must be extrapolated to the regime of low temperatures, higher densities and finite neutron-proton asymmetry to describe NS matter.

Strangeness is well established in heavy-ion experiments, where strange particles (hyperons, kaons) have been observed to appear for brief intervals of time. The high densities in the NS core are believed to favour the appearance of strange particles (hyperons, condensates of mesons or even deconfined quarks), which could then exist as stable constituents due to chemical equilibrium via non-leptonic weak interaction processes. The appearance of such additional degrees of freedom should result in reduction of the pressure and consequently a softer EoS or pressure-density relationship.

Hyperons:

The presence of hyperons in neutron stars was considered for the first time in the pioneering work of Ambartsumyan and Saakyan in 1960 [6]. With increasing density, new degrees of freedom in the form of hyperons are expected to appear in addition to nucleons according to Pauli principle. At the high density core, the Fermi energy of nucleons occupying highest energy state can exceed

the mass of hyperons. The weak interaction allows the transformation of some of the nucleons to hyperons which is energetically favorable in dense matter. Conversion of baryons into hyperons relieves the Fermi pressure exerted by the baryons, hence equation of state will get softened. Baryons get transformed into hyperons through this particle reaction nucleons get transformed into hyperons through weak interactions:

$$N + N \rightarrow N + \Lambda + K. \tag{1.6}$$

The kaon in the above reaction is free to decay unless driven by some phase transition (i.e. Bose-Einstein condensation). For example,

$$K^0 \rightarrow 2\gamma, \tag{1.7}$$

$$K^- \rightarrow \mu^- + \bar{\nu}, \tag{1.8}$$

$$\mu^- + K^+ \rightarrow \mu^- + \mu^+ + \nu \rightarrow 2\gamma + \nu. \tag{1.9}$$

Contrary to terrestrial conditions, where hyperons are unstable and decay into nucleons through the weak interaction, the equilibrium conditions in neutron stars can make the inverse process happen, so the formation of hyperons becomes energetically favorable.

However, the hyperons relieve the Fermi pressure exerted by the nucleons, hence the EoS gets softened. The presence of the hyperons lowers the maximum mass of the neutron star sequence. This might however be incompatible with the recent observation of large NS masses $\sim 2M_{solar}$ [7, 8]. There have been many suggestions in the recent past to solve this apparent dilemma [9, 10, 11, 12, 13, 14, 15, 16], which revealed the unforeseen role played by interactions among strange particles and could still produce a NS within the observational mass constraint.

Bose-Einstein condensates of anti-kaons: It was first proved by Kaplan and Nelson within a chiral $SU(3)_L \times SU(3)_R$ model that K^- mesons may undergo Bose-Einstein condensation in dense matter formed in heavy ion collisions[17]. In this model baryons directly couple with anti-kaons(K^-). K^- condensation in the core of neutron stars was studied extensively using chiral models [18] and mean field models [19]. The attractive interaction in nuclear matter reduces the in-medium energy of (anti)kaons; which at higher density eventually falls below the chemical potential of the leptons(electrons) and replaces them, through the equations

$$n \leftrightarrows p + K^-, e^- \leftrightarrows K^- + \nu_e. \tag{1.10}$$

With the replacement of electrons with anti-kaons the EoS becomes soften, as a result the maximum mass of the NS decreases. The threshold of anti-kaon condensates depends sensitively on the optical potential, whose value in nuclear medium is not known exactly. Typical threshold

density of K^- condensation in nucleons-only neutron star matter was about 3–4 times normal nuclear matter density [19, 20].

1.3 NS Structure

1.3.1 Static

For an isolated, static, spherically symmetric star, the well known Tolman-Oppenheimer-Volkoff (TOV) i.e. the conservation of mass and hydrostatic equilibrium equations are supplemented by the EoS of the dense matter. The mass-radius relation for a static NS can be obtained theoretically by solving the TOV equations imposing the boundary condition that pressure vanishes on the surface of the star. This also gives an upper bound to the mass of a static NS. However, at finite temperature the pressure never really vanishes and hence the surface of the NS cannot be determined definitely. The maximum mass reached in a sequence is also a function of the constituent composition as well as the temperature profile inside a NS.

1.3.2 Rotating

In general, the equilibrium of a rotating NS depends on the rotational effects considerably. Soon after the CCSN explosion, the neutrino-trapped PNS is expected to be rotating differentially due to lack of enough viscous forces [21, 22]. Differentially rotating stars can support significantly more mass in equilibrium than static or rigidly rotating stars [23]. Keeping in mind the uncertainty in initial rotational state of collapsing core, the actual degree of non-uniformity in rotation of a PNS is unknown. As they settle into β-equilibrium, viscosity dampens the differential rotation. Apart from the slight differential rotation following glitches, NS are expected to rotate uniformly [24]. A uniformly rotating star can accommodate more mass than non-rotating star by almost by 20% [25, 26, 27]. We discuss the rotating NS in details in the subsequent chapters in this thesis.

1.4 NS Observables

The microscopic EoS of dense matter is one of the key ingredients that governs the global astrophysical NS observables, such as its mass, radius or moment of inertia. Solving equations of hydrostatic equilibrium, one can obtain the mass and radius of a NS given its EoS. A softer EoS implies lower pressure at a given density and therefore result in lower NS mass. Thus NS observations can help to constrain its internal structure and composition and hence the EoS of dense matter. In this section we discuss the present observations of NS.

1.4.1 The Pulsars

NSs are mostly observed in radio and are known as pulsars (PSRs). Pulsar observation has come a long way since the first PSR was detected by Jocelyn Bell Burnell and Antony Hewish in the year 1967 [28]. Till date, more than 2500 PSRs have been observed in our galaxy [29], out of which a large fraction has time period between 0.1 to 10 seconds and are known as ordinary PSRs. The millisecond pulsars (MSP) on the other hand are part of binary systems and are rapidly spinning stars that are powered by the flow of matter and momentum from their companion stars. The 24 known AXMSP (accreting X-ray milli second PSRs) have an average time period of ~ 3 ms. When X-ray emission ceases, these stars emit radio waves. There are ~ 300 recycled radio MSP in our galaxy[30]. The fastest known pulsar, PSR J1748-2446ad [31], has a rotation period of 1.397 ms and a frequency of 716 Hz. In addition, some young PSRs are also observed to be rotating with fast velocities. For example, the Crab pulsar rotates once in 33 ms and is known to emit giant radio pulses. The frequency of a rotating star is limited by the mass-shedding phenomenon only. At mass shedding limit a rigidly-rotating NS rotates with maximum frequency possible which is defined as its Kepler frequency.

1.4.2 Mass and radius of the Neutron star

NSs are the nature's laboratories for studying such highly dense matter. One indirect way to study the properties of such matter is by knowing the mass profile of a NS. The NS mass is fairly established by many observational studies. The maximum masses observed till now are $1.928 \pm 0.017\ M_{solar}$ and $2.01 \pm 0.04\ M_{solar}$ for PSRs J1614-2230 and J0348+0432 respectively [7, 8, 32]. Any cold EoS intending to describe the matter inside the core of a NS must be able to reach upto this level. This constraint in itself rules out many of the proposed EoS for NS. Knowing mass alone is, however, insufficient to rigidly pinpoint towards underlying EoS and a knowledge of NS radius is very much required. A quest to understand the NS EoS is a wide open field of research at present and provides an important link in comprehending the behaviour of matter at high densities.

Apart from NS masses, there are several other observational signatures of strange matter in NSs. Until now, there existed inherent uncertainties in the determination of a NS radius observationally. The recently launched NICER (Neutron star Interior Composition Explorer) mission aims to measure radii upto 5% precision in the near future, and has already started providing interesting constraints on the dense matter EoS [33]. Estimates of NS radii have also been obtained in the recent past from the double pulsar J0737-3039 system [34], which is well constrained from the measurement of its post-Keplerian parameters.

1.4.3 Gravitational wave Observations

Detection of Gravitational Wave (GW) signal from the inspiral of binary neutron stars by the Advanced LIGO (Laser Interferometer Gravitational wave observatory) and Advanced VIRGO (from the European Gravitational Observatory) has provided a new way to understand the interior of the neutron star, which otherwise is not possible with the current experimental facilities available on earth. Till now two such events were detected(GW 170817, GW 190425), GW 170817 was accompanied by a gamma ray burst GRB 170817A, detected by Fermi-GBM, 1.74 s after the coalescence. These corroborate the hypothesis of a neutron star merger and provide the first direct evidence of a link between the NS mergers and short gamma-ray bursts. For GW 190425 no gamma ray bursts were detected. Detection of a waveform prior to the merger allows us to determine chirp mass $M_c = (M_1 M_2)^{3/5}/M^{1/5}$, where M_1 and M_2 are the masses of coalescing NSs. From the phase part of the waveform one can estimate tidal deformability of NS, that on the other hand can set limits on the neutron star radius[35]. Spin priors can affect the inference of tidal and EoS parameters, and low-spin results are generally more constrained. For GW 170817 the component masses are found to be in the range 1.17-1.60 M_{solar} and radius to be in the range of 12-13 km. For GW 190425 the component masses are found to be in the range 1.46-1.87 M_{solar} and the radii to be only below 15 km [36].

One of the most promising tools that has emerged in the recent past is that of oscillation modes in NSs that emit GW. Unlike electromagnetic signals that are related to surface phenomena, GW can directly probe the NS interior composition. Several studies have shown [37] that unstable modes such as r-modes and w-modes contain signatures of strange matter in the NS core that can be extracted from the GW signal when detected.

The outcome of the NS merger in GW170817 is highly debated, given the uncertainties associated with the detection of the post-merger GWs. Post-merger searches by the LIGO-VIRGO collaboration did not find evidence for GW from the remnant [35, 38, 39]. One possible outcome is a differentially-rotating hot hyper-massive NS [40]. The stability of the conjectured hyper-massive merger remnant is extremely interesting as it depends crucially on the dense matter EoS as well as the differential rotation velocity profile. Several works in the literature have explored the equilibrium solutions of differentially rotating NSs [41, 42].

1.5 Objective of my Work

In this thesis we study the role of strange particles for rotating relativistic NSs. Equilibrium models of static, uniformly and differentially rotating compact stars are numerically computed applying several realistic EoS. We consider both cold as well hot NS at constant entropy per particle for the study.

Properties of rapidly rotating hot neutron stars with antikaon condensates at constant entropy per baryon

The hot, lepton-rich remnant born subsequent to the supernova explosion (type II) are called proto-neutron stars(PNS). Neutrinos trapped during the catastrophic implosion diffuse out on the time scale of a few tens of seconds. We study the equilibrium properties of such a hot NS rotating uniformly once the neutrinos diffuse out. We first construct EoS for NS containing thermal kaons (K^T) and (K^-) condensates in its core. The finite entropy EoS for NS is constructed within the frame work of the relativistic mean-field theoretical model with density-dependent couplings. Choosing a constant specific entropy ensures the fall of temperature from the core to the surface of a NS. All these EoS's are tabulated at a range of constant specific entropy(s) and for different optical potentials($U_{\bar{K}}$).

Next the gravitational masses for different baryon densities are generated at constant total entropy(S), which can be expressed as $S = s \times M_B$, for the static NSs. Gravitational mass will be higher for higher value of entropy. We also study the effect of K^- condensation for all possible parameter ranges and compare them with the observational mass constraints[7, 8]. We also probe the particle fraction and temperature profile for all these parameters. Next we extend these studies to a rapidly rotating NS and investigate how the maximum mass of a given sequence varies with an increase in the corresponding angular momentum. We study the effect of rotation on the equilibrium structure of a NS in the form of isocontours of its fluid energy density. From the contour plots, we visualise how the optical potential influences the compactness or the shape of the NS. Also, we see the deformation of a spherically symmetric star with the increase of rotation frequency and temperature.

At the end, we make a rough estimate of GW amplitude emitted by a NS having strong magnetic field (B).

Signatures of strangeness in neutron star merger remnants

The recent detection of gravitational waves from the merger of neutron-star binaries [35] has ushered in a new era of multi-messenger astronomy. When two NSs merge, they produce a merger remnant that either collapses promptly to a black hole, or a metastable object, e.g., a hyper-massive neutron star (HMNS) eventually collapsing to a BH on a secular timescale. The stability of neutron stars is well-understood in general relativity for uniformly rotating models. Friedman et al. [43] showed that along a sequence of nonrotating relativistic stars, secular instability sets in at the maximum of this sequence, i.e. the turning point. We extend the onset of dynamical instability for uniformly rotating neutron stars to differentially rotating stars.

HMNS is supported against collapse with the help of differential rotation and thermal pressure. We compute different equilibrium models of differentially rotating relativistic NSs of type A in the classification of Ansorg et al. [44], and evolve selected models along sequences of constant angular momentum, using the "j-constant" law to model differential rotation. Our objective is to study the effect of strangeness in NS mergers and also calculate lifetimes of the HMNS. We construct various mass sequences for a NS, rotating differentially and find the onset of secular instability. We do this calculation for a number of EoS, for various degree of differential rotation. In addition, we check the validity of universal relations for cold NS proposed by Weih et. al[45] with our finite entropy EoS. In fact several authors showed that "quasi-universal" relations can be found when calculating the turning-point mass [27, 46, 47] for uniformly rotating NSs. The universal relation for differential rotation in turn allows us to compute the maximum mass allowed by differential rotation, in terms of the maximum mass of the nonrotating configuration. Finally we calculate the collapse time of the HMNS using the relation proposed by Lucca and Sagunski [48]. This can be applied to get a new insight into the NS interiors and constrain the properties of dense matter.

Chapter 2

Formalism

2.1 Introduction

Matter density in the core of a neutron star is a few times the normal nuclear matter density, i.e. $2.7 \times 10^{14} g/cm^3$. Our knowledge about nuclear matter is confined up to this saturation density. Exact nature of this high-density many body system in the interior of the NS is unknown to us. Various theoretical models have been proposed to explain the internal structure and characteristics of NS. Among them the most used one is the Walecka model[49, 50]. We adopt this relativistic field theoretical model for the description of neutron star matter. It is a phenomenological description of the nuclear many-body problem and is fully Lorentz invariant. Here the nucleons are treated as point-like particles and are described by Dirac equation. In the Walecka model, nucleon-nucleon interaction is mediated by the exchange of scalar (σ), vector (ω) mesons. Later, it was extended to incorporate ρ meson to take care of the isospin asymmetry of the system[51]. In a phenomenological theory the couplings of interacting mesons with nucleons are determined to reproduce the experimental data at saturation density such as saturation density, binding energy, symmetry energy, incompressibility and the effective nucleon mass. All the phenomenological models are fitted to those properties at the saturation density and then extrapolated to high density regime to describe the highly dense NS matter. Extrapolating the nuclear matter properties to high density leads to uncertainties. In most of the relativistic mean field (RMF) calculations, several combinations of non-linear self interaction terms for scalar and vector fields are introduced to account for the high density behaviour. However, instabilities and higher order field dependence at high density may introduce some uncertainties.

Traditional RMF models incorporate the interaction of nucleons and mesons in a pure phenomenological way. A more elaborate but more fundamental approach is based on derivation in-medium interaction microscopically. A fully covariant and consistent field theory requires to treat the interaction vertices as a functional of the field operators. Therefore, we consider a

more suitable approach by Typel et. al where density-dependence is introduced through the meson-baryon couplings [52, 53, 54]. This is widely known as DD2 model. The relativistic EoS model with linear couplings and density dependent parametrization was already in use [52, 55, 56]. In DD2, experimental nuclear masses are used[54]. The DD2 EoS model agrees well with the predictions of Chiral EFT [57], and also with nuclear physics experiments (heavy ion collision analysis, dipole polarizability analysis etc.) as well as various astrophysical observations.

Nuclear symmetry energy i.e the energy associated with isospin asymmetry is a very important factor in determining the stiffness EoS at high densities. The symmetry energy(S_ν) and its density dependence (L) near the saturation density n_0 can be constrained from experimental results as 29 MeV $< S_\nu <$ 32.7 MeV and 40.5 MeV $< L <$ 61.9 MeV respectively [57, 58]. The values $S_\nu = 31.67$ MeV and $L = 55.04$ MeV for DD2 model are well within these bounds.

In this chapter we first describe RMF theory based on the Walecka model. This model was first conceived for nucleons and extended to include other baryons of the octet (Λ, Σ, Ξ). Also, we consider the antikaon condensates at the high density matter and discuss the formalism to include them at the same footing as the baryons. We consider nuclear matter as a static (in the rest frame of nuclear matter) and uniform system in the ground state. We derive various physical quantities of the NS constituents for cold as well as hot dense matter. Solving the equations of motions we get a realistic equation of state (EoS) i.e., the relation between the internal pressure and the energy density or mass/number density of the NS matter. Next we briefly discuss various model parameters supported by theory, phenomenology and experimental data.

The above theoretical models could be supported by the observational results. For this, one calculates the structure of a neutron star. The structure of a static and spherically symmetric neutron star is obtained from Einstein's equation using Schwarzschild metric. This leads to the coupled non-linear differential equations known as Tolman-Oppenheimer-Volkoff (TOV) equations. For the tabulated EoS, the TOV equations are integrated outwards from the origin (r = 0) to the point r = R where the pressure goes to zero. This value r=R defines the radius of the star. Solutions of TOV equations yield a sequence of neutron stars. Their mass-radius can be compared to the observed data.

The focus of this thesis work is rotating NSs. NS are born at the aftermath of core collapse supernova explosion (CCSN) of a relatively massive main-sequence star. Soon after the CCSN explosion, the neutrino-trapped PNS is expected to be rotating differentially due to lack of enough viscous forces [21, 22]. As they settle into β-equilibrium, viscosity dampens the differential rotation. Apart from the slight differential rotation following glitches, NS are expected to rotate uniformly [24]. Here, we first consider an idealised scenario of uniform and rigid rotation about an axisymmetric axis which represents an approximation to the actual rotational state of a hot NS [59]. The equilibrium structures of the rotating NS is studied numerically by the code Lorene

[60]. Next the investigation is extended to differential rotation. The field equations, derived in the 3+1 formulation is discussed in details and several equilibrium quantities of the rapidly rotating NS are mentioned. The two and three dimensional Virial identities (GRV2 and GRV3) are used to check the accuracy of computed numerical solutions.

2.2 Relativistic Mean Field Model with Density-dependent couplings

2.2.1 Hadronic Phase

The dense matter inside the NS core is modeled based on the Walecka model, where the baryons in the dense interior of a NS interact through the exchange particles σ, ω, and ρ. The scalar σ and the vector ω mesons take care of the long range attractive and short range repulsive nature of the nuclear force respectively. The isovector ρ meson is added to the original Walecka model to take care of the isospin asymmetry. The Lagrangian density consists of terms related to the free Dirac nucleons of rest mass m_B, the free mesons, and the interaction among them.

$$\begin{aligned}\mathscr{L}_B &= \sum_B \bar{\psi}_B \left(i\gamma_\mu\partial^\mu - m_B + g_{\sigma B}\sigma - g_{\omega B}\gamma_\mu\omega^\mu - g_{\rho B}\gamma_\mu\boldsymbol{\tau}_B\cdot\boldsymbol{\rho}^\mu\right)\psi_B \\ &\quad + \frac{1}{2}\left(\partial_\mu\sigma\partial^\mu\sigma - m_\sigma^2\sigma^2\right) - \frac{1}{4}\omega_{\mu\nu}\omega^{\mu\nu} + \frac{1}{2}m_\omega^2\omega_\mu\omega^\mu - \frac{1}{4}\boldsymbol{\rho}_{\mu\nu}\cdot\boldsymbol{\rho}^{\mu\nu} + \frac{1}{2}m_\rho^2\boldsymbol{\rho}_\mu\cdot\boldsymbol{\rho}^\mu. \quad (2.1)\end{aligned}$$

Here ψ_B denotes the Dirac spinor for baryon B, τ_B the isospin operator; the field strength tensors for the vector mesons are given by $\omega^{\mu\nu} = \partial^\mu\omega^\nu - \partial^\nu\omega^\mu$ and $\boldsymbol{\rho}^{\mu\nu} = \partial^\mu\boldsymbol{\rho}^\nu - \partial^\nu\boldsymbol{\rho}^\mu$. The coupling strength of the mesons with baryons is specified by $g_{\alpha B}(\hat{n})$ where $\alpha = \sigma,\ \omega$ and ρ. The meson-exchange model can explain the dense matter upto saturation density. To represent the behaviour of the matter above saturation density, the $g_{\alpha B}(\hat{n})$'s are made density-dependent. The density operator $\hat{n}$ is given by, $\hat{n}=\sqrt{\hat{j}_\mu\hat{j}^\mu}$, where $\hat{j}_\mu = \bar{\psi}\gamma_\mu\psi$ [53, 54].

The above model has been extended to accommodate the whole baryon octet. Their interaction is considered through meson exchange in similar fashion as the nucleon-nucleon interaction. However, an additional interacting vector meson ϕ is included here for the hyperon-hyperon interaction only [61, 62]. The Lagrangian density for hyperon-hyperon interaction is,

$$\mathscr{L}_{YY} = \sum_B \bar{\psi}_B(g_{\phi B}\gamma_\mu\phi^\mu)\psi_B - \frac{1}{4}\phi_{\mu\nu}\phi^{\mu\nu} + \frac{1}{2}m_\phi^2\phi_\mu\phi^\mu\ . \quad (2.2)$$

Leptons are treated as non-interacting particles and described by the Lagrangian density

$$\mathscr{L}_l = \sum_l \bar{\psi}_l(i\gamma_\mu\partial^\mu - m_l)\psi_l. \quad (2.3)$$

Substituting the total Lagrangian density ($\mathscr{L} = \mathscr{L}_B + \mathscr{L}_l + \mathscr{L}_{YY}$) in Euler-Lagrangian equation

$$\partial^\mu \left[\frac{\partial \mathscr{L}}{\partial(\partial^\mu \phi)}\right] - \frac{\partial \mathscr{L}}{\partial \phi} = 0, \tag{2.4}$$

we obtain equation of motion for meson fields ϕ.

$$\begin{aligned}
\partial^\mu(\partial_\mu\sigma) + m_\sigma^2\sigma &= \sum_B g_{\sigma B}\bar{\psi}_B\psi_B \\
\partial^\nu\omega_{\mu\nu} + {m_\omega}^2\omega_\mu &= \sum_B g_{\omega B}\bar{\psi}_B\gamma_\mu\psi_B \\
\partial^\nu\rho_{\mu\alpha\nu} + {m_\rho}^2\rho_{\mu\alpha} &= \frac{1}{2}\sum_B g_{\rho B}\bar{\psi}_B\gamma_\mu\tau_{\alpha B}\psi_B. \\
\partial^\nu\phi_{\mu\nu} + {m_\phi}^2\phi_\mu &= \sum_B g_{\phi B}\bar{\psi}_B\gamma_\mu\psi_B.
\end{aligned} \tag{2.5}$$

and equation of motion for baryon B

$$[i\gamma^\mu\partial_\mu - \gamma^\mu\Sigma_B - (m_B - g_{\sigma B}\sigma)]\psi_B = 0. \tag{2.6}$$

Exact solution for the meson field Eqs. 2.23 are complicated because of the presence of source terms on the right hand side. Also coupling constants $g_{\omega B}, g_{\sigma B}, g_{\rho B}$ are too large to use perturbative approach. At high densities meson fields are replaced by their expectation values, i.e, $\sigma \to <\sigma>$, $\omega_\mu \to <\omega_\mu>$, $\rho_\mu \to <\rho_\mu>$, $\phi_\mu \to <\phi_\mu>$. Substitution of meson fields by expectation values is called Mean Field Approximation. In the rest frame of the matter the space components of ω_μ, ρ_μ, ϕ_μ vanish, the third component of isovector ρ meson only couples to nucleons because of the expectation values of the sources of charged ρ mesons vanish in the ground state of the system.

In Eq. 2.6 the term $\Sigma_B = \Sigma_B^{(0)} + \Sigma_B^{(r)}$ is the vector self-energy. The first term $\Sigma_B^{(0)}$ consists of usual non-vanishing components of vector mesons, i.e., $\Sigma_B^{(0)} = g_{\omega B}\omega_0 + g_{\rho B}\tau_{3B}\rho_{03} + g_{\phi B}\phi_0$, while the second term is the rearrangement term. $\Sigma_B^{(r)}$ arises due to density dependence of meson-baryon couplings[15] and assumes the form

$$\Sigma_B^{(r)} = \sum_B [-g'_{\sigma B}\sigma n_B^s + g'_{\omega B}\omega_0 n_B + g'_{\rho B}\tau_{3B}\rho_{03}n_B + g'_{\phi B}\phi_0 n_B] \ . \tag{2.7}$$

In the Eq. 2.7 $g'_{\alpha B} = \frac{\partial g_{\alpha B}}{\partial n_B}$, $\alpha = \sigma,\ \omega,\ \rho,\ \phi$.

The dense matter in the NS interior is highly degenerate and its properties are strongly determined by the Pauli principle. All the energy states below the Fermi energy E_F are occupied. At T=0, the Fermi distribution function $f(E) = \frac{1}{e^{\beta(E-E_F)}+1}$ behaves like a step function i.e. $\lim_{T\to 0} f(E) = \theta(E_F - E)$. Hence, the number density and scalar number density for the baryon

B are given by

$$n_B = \langle \bar{\psi}_B \gamma_0 \psi_B \rangle = \frac{2J_B+1}{2\pi^2} \int_0^{k_{F_B}} k^2 dk = \frac{k_{F_B}^3}{3\pi^2} \tag{2.8}$$

$$\begin{aligned} n_B^s &= <\bar{\psi}_B \psi_B> = \frac{2J_B+1}{2\pi^2} \int_0^{k_{F_B}} \frac{m_B^*}{(k^2+m_B^{*2})^{1/2}} k^2 \, dk \\ &= \frac{m_B^*}{2\pi^2} \left[k_{F_B} \sqrt{{k_{F_B}}^2 + m_B^{*2}} - m_B^{*2} ln \frac{k_{F_B} + \sqrt{{k_{F_B}}^2 + m_B^{*2}}}{m_B^*} \right]. \end{aligned} \tag{2.9}$$

In the above equations, J_B=1/2 for the Fermions, k_{F_B} is the Fermi momentum and $m_B^* = m_B - g_{\sigma B}\sigma$ is the effective mass of the baryon.

2.2.2 EoS of Cold Nuclear matter

EoS is a relation between energy density and pressure. Expressions for Energy density and pressure are obtained from energy-momentum tensor, defined by

$$\Gamma_{\mu\nu} = -g_{\mu\nu}\mathscr{L}_B + \frac{\partial \mathscr{L}_B}{\partial(\partial^\mu \psi)}(\partial_\nu \psi). \tag{2.10}$$

The energy density and pressure due to baryons are given by

$$\begin{aligned} \varepsilon_B &= <\Gamma_{00}> = -\langle \mathscr{L}_{\mathscr{B}} \rangle + \left\langle \bar{\psi}_B \gamma_0 \partial_0 \psi_B \right\rangle \\ P_B &= <\Gamma_{ii}> = -\langle \mathscr{L}_{\mathscr{B}} \rangle + \frac{1}{3} \left\langle \bar{\psi}_B \gamma_i \partial_i \psi_B \right\rangle. \end{aligned} \tag{2.11}$$

The factor 1/3 takes care of the isotropy of the system.

The baryon field Eq. 2.6 and meson field Eqs. 2.23 are solved simultaneously along with the constraints of i)conservation of total baryon number ($\sum_B n_B$ = constant) ii)charge neutrality ($n_p = n_l$) iii)β-equilibrium ($\mu_i = b_i\mu_n - q_i\mu_l$, where b_i is the baryon number of the i-th particle and q_i its charge, μ_n and μ_l are the chemical potential of neutron and leptons respectively). The value of the fields are substituted back into Eqs. 2.11, so that the final expressions for the energy density and pressure can be obtained as

$$\begin{aligned} \varepsilon_B &= \frac{1}{2}m_\sigma^2\sigma^2 + \frac{1}{2}m_\omega^2\omega_0^2 + \frac{1}{2}m_\rho^2\rho_{03}^2 + \frac{1}{2}m_\phi^2\phi_0^2 + \\ &\sum_B \frac{2J_B+1}{2\pi^2} \int_0^{k_{F_B}} (k^2+m_B^{*2})^{1/2} k^2 \, dk + \sum_l \frac{1}{\pi^2} \int_0^{K_{F_l}} (k^2+m_l^2)^{1/2} k^2 \, dk. \end{aligned} \tag{2.12}$$

$$P_B = -\frac{1}{2}m_\sigma^2\sigma^2 + \frac{1}{2}m_\omega^2\omega_0^2 + \frac{1}{2}m_\phi^2\phi_0^2 + \frac{1}{2}m_\rho^2\rho_{03}^2 + \Sigma_B^{(r)}\sum_B n_B + \frac{1}{3}\sum_B \frac{2J_B+1}{2\pi^2}\int_0^{k_{F_B}} \frac{k^4\, dk}{(k^2+m_B^{*2})^{1/2}} + \frac{1}{3}\sum_l \frac{1}{\pi^2}\int_0^{k_{F_l}} \frac{k^4\, dk}{(k^2+m_l^2)^{1/2}} \,. \quad (2.13)$$

The pressure(P_B)is related to the energy density (ε_B) through the Gibbs-Duhem relation

$$P_B = \sum_i \mu_i n_i - \varepsilon_B. \quad (2.14)$$

The rearrangement term does not appear in the energy density term explicitly. However, it contributes to the pressure term through the baryon chemical potentials and accounts for the energy-momentum conservation and thermodynamic consistency of the system [52, 55, 63].

2.2.3 EoS of Hot Nuclear matter

The number density of the baryon at finite temperature is given by,

$$n_B = 2\int \frac{d^3k}{(2\pi)^3}\left(\frac{1}{e^{\beta(E^*-\nu_B)}+1} - \frac{1}{e^{\beta(E^*+\nu_B)}+1}\right). \quad (2.15)$$

Here, $\beta = 1/T$ and $E^* = \sqrt{(k^2+m_B^{*2})}$. Scalar density for nucleons on the other hand is,

$$n_B^S = 2\int \frac{d^3k}{(2\pi)^3}\frac{m_B^*}{E^*}\left(\frac{1}{e^{\beta(E^*-\nu_B)}+1} + \frac{1}{e^{\beta(E^*+\nu_B)}+1}\right) \,. \quad (2.16)$$

The Eqs. 2.12 and 2.13 at finite temperature (T) are modified to

$$\epsilon_B = \frac{1}{2}m_\sigma^2\sigma^2 + \frac{1}{2}m_\omega^2\omega_0^2 + \frac{1}{2}m_\rho^2\rho_{03}^2 + \frac{1}{2}m_\phi^2\phi_0^2 + 2\sum_B \int \frac{d^3k}{(2\pi)^3}E^*\left(\frac{1}{e^{\beta(E^*-\nu_B)}+1} + \frac{1}{e^{\beta(E^*+\nu_B)}+1}\right) \,. \quad (2.17)$$

and

$$P_B = -\frac{1}{2}m_\sigma^2\sigma^2 + \frac{1}{2}m_\omega^2\omega_0^2 + \frac{1}{2}m_\rho^2\rho_{03}^2 + \frac{1}{2}m_\phi^2\phi_0^2 + \Sigma_B^{(r)}\sum_B n_B + 2T\sum_B \int \frac{d^3k}{(2\pi)^3}[ln(1+e^{-\beta(E^*-\nu_B)}) + ln(1+e^{-\beta(E^*+\nu_B)})]. \quad (2.18)$$

The entropy density ($\mathscr{S}_B$) of baryons is related to energy density and pressure through Gibbs-Duhem relation $\mathscr{S}_B = \beta\left(\epsilon_B + P_B - \sum_i \mu_i n_i\right)$.

2.2.4 Anti-kaon condensation and the EoS

We consider antikaon-baryon interaction on the same footing as the baryon-baryon interaction. The Lagrangian density for antikaons in the minimal coupling scheme can be expressed as[64]

$$\mathscr{L}_K = D^*_\mu \bar{K} D^\mu K - m^{*2}_K \bar{K} K. \tag{2.19}$$

The covariant derivative is given by $D_\mu = \partial_\mu + ig_{\omega K}\omega_\mu + ig_{\rho K}\boldsymbol{\tau}_K \cdot \boldsymbol{\rho}_\mu + ig_{\phi K}\phi_\mu$ and $m^*_K = m_K - g_{\sigma K}\sigma$ is the effective mass of antikaons where m_K is the bare kaon mass. The isospin doublet for kaons is, $K \equiv (K^+, K^0)$ and that for antikaons is $\bar{K} \equiv (K^-, \bar{K^0})$. It is to be noted that the antikaon-baryon couplings are density independent. The in-medium energy of the $K^\pm$ mesons is given by,

$$\omega_{K^\pm} = \sqrt{(k^2 + {m^*_K}^2)} \pm (g_{\omega K}\omega_0 + g_{\rho K}\rho_{03}). \tag{2.20}$$

For s-wave(k=0) condensation, the momentum dependence vanishes in $\omega_{K^\pm}$. The threshold condition for s-wave K^- condition is $\mu_{K^-} = \omega_{K^-}$. The K^- condensation in medium is governed by the particle reaction $n \leftrightarrow p + K^-$. The threshold condition is given by,

$$\mu_{K^-} = \mu_n - \mu_p = \mu_e. \tag{2.21}$$

From the Eq.2.20, we can observe that ω_{K^+} value never decreases to meet the threshold condition $\omega_{K^+} = \mu_e$. But ω_{K^-} decreases from its vacuum value m_K with increasing density as the meson field grows and thus only k^- condensates appear in the system[18]. Also, the threshold condition (Eq.2.21) is met only if the interaction of mesons in nuclear medium is attractive, which reduces its effective mass. Various experimental data confirm that the antikaons experience an attractive potential and kaons have a repulsive interaction in nuclear matter [15].

The scalar and vector densities of antikaon condensates at $T = 0$ for s-wave($k = 0$) are same and given by[65],

$$n_{K^-,\bar{K^0}} = 2(\omega_{K^-,\bar{K^0}} + g_{\omega K}\omega_0 + g_{\phi K}\omega_0 \pm g_{\rho K}\rho_{03})\bar{K}K. \tag{2.22}$$

The energy density of antikaons at T = 0 is given by $\epsilon_K = {m^*}_K(n_{K^-} + n_{\bar{K}^0})$.

Antikaon condensates do not contribute to pressure, but implicitly change the rearrangement term, given by Eq.2.7 through meson fields. The meson field equations in presence of antikaon condensates in the mean field approximation have an additional contribution from antikaon

condensates and are given by

$$\begin{aligned} m_\sigma^2\sigma &= \sum_B g_{\sigma B} n_B^s + g_{\sigma K}\sum_K n_K \\ m_\omega^2\omega_0 &= \sum_B g_{\omega B} n_B - g_{\omega K}\sum_K n_K \\ m_\rho^2\rho_{03} &= \sum_B g_{\rho B}\tau_{3B} n_B + g_{\rho K}\sum_K \tau_{3K} n_K \\ m_\phi^2\phi_0 &= \sum_B g_{\phi B} n_B - g_{\phi K}\sum_K n_K. \end{aligned} \tag{2.23}$$

The energy density of K^- condensates at finite temperature can be expressed as

$$\begin{aligned} \epsilon_K &= m_K^* n_K^C + \left(g_{\omega K}\omega_0 + \frac{1}{2}g_{\rho K}\rho_{03}\right) n_K^T \\ &\quad + \int \frac{d^3k}{(2\pi)^3}\left(\frac{\omega_{K^-}}{e^{\beta(\omega_{K^-}-\mu_{K^-})}-1} + \frac{\omega_{K^+}}{e^{\beta(\omega_{K^+}+\mu_{K^+})}-1}\right) . \end{aligned} \tag{2.24}$$

The net antikaon number density at finite temperature is given by, $n_K = n_K^C + n_K^T$, where, n_K^C gives the K^- condensate density. Here, n_K^T represents the thermal density and is given by,

$$n_K^C = 2\left(\omega_{K^-} + g_{\omega K}\omega_0 + \frac{1}{2}g_{\rho K}\rho_{03}\right)\bar{K}K = 2m_K^*\bar{K}K \ . \tag{2.25}$$

$$n_K^T = \int \frac{d^3k}{(2\pi)^3}\left(\frac{1}{e^{\beta(\omega_{K^-}-\mu)}-1} - \frac{1}{e^{\beta(\omega_{K^+}+\mu)}-1}\right) . \tag{2.26}$$

2.2.5 The leptons

Apart from nucleons and K^- mesons, NS also has non-interacting leptons in the system. Leptons being Fermions, their physical properties such as number density, energy density and pressure are calculated following a similar method as that used for baryons, using the Lagrangian density

$$\mathscr{L}_l = \sum_l \bar{\psi}_l\left(i\gamma_\mu\partial^\mu - m_l\right)\psi_l \ . \tag{2.27}$$

Here, ψ_l $(l \equiv e, \mu)$ denotes the lepton spinor. In a NS, when the electron chemical potential μ_e becomes equal to the muon mass, the electrons are converted to muons by $e^- \rightarrow \mu^- + \bar{\nu}_\mu + \nu_e$. Therefore, in a NS the onset of muons is determined by the condition $\mu_e = \mu_\mu$. The muons are usually ignored in hot dense matter owing to their high rest mass ($m_\mu \sim 105.66 MeV/c^2$), which suppresses their formation. However, at high temperatures the electron chemical potential exceeds m_μ leading to a significant number of muons. Nevertheless, in our study, the energetically favoured antikaon condensates replace the leptons as soon as they are formed. We have ignored

the μ^+s, as their formation is highly suppressed. The total energy density in the presence of K^- condensates is therefore, $\epsilon = \epsilon_N + \epsilon_K + \epsilon_l$.

We generate the EoS at constant entropy per baryon (s). The entropy density ($\mathscr{S}_N$) of nucleons and leptons is related to energy density and pressure through Gibbs-Duhem relation $\mathscr{S}_N = \beta\left(\epsilon_N + P_N - \sum_i \mu_i n_i\right)$, where, $i = n, p, l$. The entropy density of antikaons is, $\mathscr{S}_K = \beta\left(\epsilon_K + P_K - \mu_K n_K\right)$, where, $n_K = n_K^C + n_K^T$. The entropy per baryon is given by $s = \mathscr{S}/n_b$, where n_b is the total baryon density. The total entropy per baryon has contribution from the nucleons, antikaons and leptons i.e., $s = (\mathscr{S}_N + \mathscr{S}_K + \mathscr{S}_l)/n_b$.

2.2.6 Some important features of the formalism

Matching different parts of the EoS In this section, we briefly discuss matching of low density and high density parts of EoS. High density and Low density parts of EoS are joined by following matching procedure of Banik et al. [66]. Although the above procedure allows smooth transition between the different parts of EoS around nuclear saturation density, it is not completely consistent as emphasised in Marques et al. [67]. Fortin et al. [68] have shown that the core-crust matching does not have any effect on the maximum mass allowed for the star, but the uncertainty in radius calculations can be $\sim 4\%$ depending on the way core-crust matching is done. Low density part of EoS consists of non-uniform matter of light and heavy nuclei along with unbound nucleons at low temperatures and densities that are below nuclear saturation. Interaction among the unbound nucleons are described by considering the same Lagrangian density as in Eq. 2.1 and using the density dependent formalism [5, 54]. As the hyperons and K^- condensates appear only at high densities and at relatively high temperatures, the nuclei and exotic matter are never found to coexist. Therefore, we simply use the non-uniform part of the nucleons-only HS(DD2) EoS [5] following the standard prescription of minimisation of free energy as is prescribed in Banik et al. [66].

2.2.7 Model parameters

The nucleon-meson density-dependent couplings are determined following the prescription of Typel et al. [53, 54]. The functional dependence of the couplings on density was first introduced in [63] and is described as,

$$g_{\alpha B}(n_B) = g_{\alpha B}(n_0) f_\alpha(x). \tag{2.28}$$

with $x = n_B/n_0$, n_B being the baryon density. The function [63] for ω, σ is

$$f(x) = a_\alpha \frac{1 + b_\alpha(x + d_\alpha)^2}{1 + c_\alpha(x + d_\alpha)^2}$$

TABLE 2.1: Parameters of the meson-nucleon couplings in DD2 model

meson α	$g_{\alpha B}$	a_α	b_α	c_α	d_α
ω	13.342362	1.369718	0.496475	0.817753	0.638452
σ	10.686681	1.357630	0.634442	1.005358	0.575810
ρ	3.626940	0.518903			

whereas for ρ it is $f(x) = \exp[-a_\alpha(x-1)]$. The saturation density n_0, the masses of $\alpha = \sigma, \omega$ and ρ mesons, their couplings $g_{\alpha B}(n_0)$ and the coefficients a_α, b_α, c_α, d_α are found by fitting the finite nuclei properties [53, 54] and are listed in Table 2.1. The RMF model with density-dependent parameter set has the saturation density $n_0 = 0.149065 fm^{-3}$, binding energy per nucleon -16.02 MeV and incompressibility $K = 242.7$ MeV, symmetry energy $S_\nu = 31.67$ MeV and slope parameter

$$L = 3n_0 \frac{dE_{sym}}{dn}|_{n=n_0,T=0} = 55.04 MeV.$$

This version of density-dependent model(DD2) differs form the previous model only by the use of experimental nuclear masses. The masses of neutron, proton, ω and ρ mesons are 939.56536, 938.27203, 783, 763 MeV respectively [54]. The number of parameters are reduced by constraining the functions as $f_\sigma(1) = f_\omega(1) = 1$, $f'_\sigma(0) = f'_\omega(0) = 0$ and $f_\sigma(1) = f_\omega(1) = 1$, $f''_\sigma(1) = f''_\omega(1)$ [53].

Next, we determine the Λ-meson couplings using the scaling factors [15, 61] and nucleon-meson couplings of Table 2.1. The Λ hyperons do not couple to ρ mesons, their couplings to vector mesons are determined from the SU(6) symmetry [61] as $g_{\phi\Lambda} = -\frac{\sqrt{2}}{3} g_{\omega N}$ and $g_{\omega\Lambda} = \frac{2}{3} g_{\omega N}$. Finally, the scalar meson (σ) coupling to Λ is obtained from the relation,

$$U_\Lambda^B(n_0) = -g_{\sigma\Lambda}\sigma + g_{\omega\Lambda}\omega_0 + \Sigma_B^{(r)}. \tag{2.29}$$

Here, $\Sigma_B^{(r)}$ involves only the contributions of nucleons. From the analysis of energy levels in Λ-hypernuclei, the potential depth of Λ ($U_\Lambda^B(n_0)$) in the saturated nuclear matter is taken as -30 MeV [69, 70]. This determines the scaling factor $R_{\sigma\Lambda} = \frac{g_{\sigma\Lambda}}{g_{\sigma B}} = 0.62008$.

The meson-antikaon couplings are not density-dependent. We compute the vector meson-antikaon couplings according to the quark model and isospin counting rule as was done for the meson-hyperon couplings.

$$g_{\omega K} = \frac{1}{3} g_{\omega B}; \qquad g_{\rho K} = g_{\rho B}\ \sqrt{2} \qquad \text{and} \qquad \sqrt{2}\ g_{\phi K} = 6.04. \tag{2.30}$$

The scalar coupling constant ($g_{\sigma K}$) is obtained from the real part of the K^- optical potential at the normal nuclear matter density, [19, 20, 52, 61]

$$U_{\bar{K}}(n_0) = -g_{\sigma K}\sigma - g_{\omega K}\omega_0\ + \Sigma_B^{(r)}\ . \tag{2.31}$$

TABLE 2.2: Parameters of the scalar σ meson -antikaon couplings in DD2 model

$U_{\bar{K}}$ in MeV	-60	-80	-100	-120	-140
$g_{\sigma\bar{K}}$	-1.24609	-0.72583	-0.20557	0.31469	0.83495

The study of kaon atoms clearly suggests an attractive antikaon nucleon optical potential. However, different experiments suggest a range of values for $U_{\bar{K}}$ from -50 to -200MeV and do not come to any definite consensus [71]. We chose a set of values of $U_{\bar{K}}$ from -60 to -150 MeV. The coupling constants for kaons with σ-meson, $g_{\sigma K}$ at the saturation density for different values of $U_{\bar{K}}$ for DD2 model is listed in Table 2.2.

2.3 Structural properties of NS

NSs are relativistic objects and computations of their structure should be carried out in a general-relativistic (GR) framework. A rotating star is accurately described by a stationary, axisymmetric solution to the Einstein field equation

$$G^{\mu\nu} = 8\pi T^{\mu\nu} \tag{2.32}$$

where $G^{\mu\nu}$ is the Einstein tensor, describing the curvature of spacetime and $T^{\mu\nu}$ is the stress energy tensor, describing matter/energy sources of spacetime curvature. For a perfect fluid, the stress-energy tensor is given by, $T^{\mu\nu} = (\epsilon + P)u^\mu u^\nu + Pg^{\mu\nu}$, where ϵ is energy density, P is pressure, both in the fluid frame and u^μ is the fluid 4-velocity, where $g^{\mu\nu}$ are the components of the metric.

2.3.1 Static structure of a spherically symmetric star

The Schwarzschild metric for a static star gives the following line element:

$$g_{\mu\nu}dx^\mu dx^\nu = -\exp^{2\nu(r)}\,dt^2 + \left(1 - \frac{2m(r)}{r}\right)^{-1} dr^2 + r^2 d\theta^2 + r^2 sin^2\theta d\phi^2. \tag{2.33}$$

m(r) is the gravitational mass inside a sphere radius r. In hydrostatic equilibrium, the structure of a spherically symmetric, static relativistic NS is determined by the Tolman-Oppenheimer-Volkoff (TOV) equations. The 4-velocity of the fluid in the expression of stress energy tensor $T^{\mu\nu}$, is related to the metric potential by $u^\mu = (\exp^{-\nu(r)}, 0, 0, 0)$. Tolman, Oppenheimer, and Volkoff basically reformulated Einstein's equation using Eq. 2.33 to get the ordinary differential

equations [72, 73]:

$$\begin{aligned} \frac{dm}{dr} &= 4\pi\epsilon r^2 \\ \frac{d\nu}{dr} &= \left(\frac{m(r)+4\pi r^3 P}{r(r-2m(r))}\right) \\ \frac{dP}{dr} &= -(\epsilon+P)\frac{d\nu}{dr}. \end{aligned} \tag{2.34}$$

The NS matter can be approximated as a perfect fluid at zero temperature except immediately after its birth, whose EoS can be written as $\epsilon = \epsilon(n_B)$ and $P = P(n_B)$, where n_B is the baryon number density in the fluid frame. This is known as barotropic EoS. Given a barotropic EoS, the stellar structure can be computed by numerically integrating Eqs. 2.34 from the centre at r=0 out to the star surface at r=R. The choice of boundary conditions are $P(r = R) = 0$, $P(r = 0) = P_c(\rho_c)$, $m(r = 0) = 0$, and $\nu(r = R) = \frac{1}{2}ln(1 - \frac{2M}{R})$. M is the enclosed gravitational mass given by M(R)=$4\pi \int_0^R \epsilon(r)r^2dr$.

2.3.2 3+1 Formalism

The 3+1 decomposition of Einstein equation is the standard formulation used in numerical relativity[60]. 3+1 formalism relies on slicing of spacetime by a family of spacelike hypersurfaces Σ_t. The parameter t labeling hypersurface Σ_t is a real parameter. The same t is identified as coordinate time and t can be considered as scalar field on manifold $\mathscr{M}$. Since Σ_t is spacelike, at each point on Σ_t it posses a unique unit timelike normal vector $\vec{n}$, which is future-oriented

$$\vec{n} \cdot \vec{n} = -1. \tag{2.35}$$

Gradient of t, ∇t is a 1-form that satisfies $\langle \nabla t, \vec{v} \rangle = 0$. The two normal vectors $\vec{\nabla}$ t and $\vec{n}$ are necessarily colinear:

$$\vec{n} = -N\vec{\nabla}t. \tag{2.36}$$

The proportionality coefficient N is called lapse function [74]. Since each hypersurface Σ_t is assumed to be spacelike, the metric γ is induced by $\boldsymbol{g}$. Considered a tensor field on $\mathscr{M}$, the components of γ are given in terms of the components of the normal via

$$\gamma_{\mu\nu} = g_{\mu\nu} + n_\mu n_\nu. \tag{2.37}$$

Energy-Momentum tensor $\mathbf{T}$ can be expressed as

$$\mathbf{T} = \mathbf{S} + \mathbf{n} \otimes \mathbf{P} + \mathbf{P} \otimes \mathbf{n} + E\mathbf{n} \otimes \mathbf{n}, \tag{2.38}$$

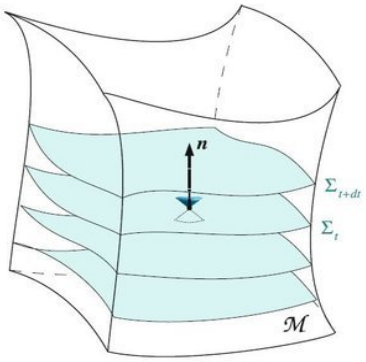

FIGURE 2.1: Foliation of spacetime $\mathscr{M}$ by a family of spacelike hypersurfaces $(\Sigma_t)_{t\in\mathbb{R}}$
Source:Fig 3.1 of the book 3+1 Formalism in General Relativity: Bases of Numerical Relativity

Where E is total energy density, $\mathbf{P}$ is momentum density 3-vector and S is stress tensor. These quantities can be measured by the ZAMO (Zero angular momentum observers), and their components are given by

$$\begin{aligned} E &= T_{\mu\nu}n^\mu n^\nu, \\ p_\alpha &= -T_{\mu\nu}n^\nu \gamma^\mu{}_\alpha, \\ S_{\alpha\beta} &= T_{\mu\nu}\gamma^\mu{}_\alpha \gamma^\nu{}_\beta. \end{aligned} \tag{2.39}$$

Next, we may decompose the basis vector ∂_t into its normal and tangent components

$$\partial_t = N\vec{n} + \vec{\beta}, \tag{2.40}$$

where $\beta := \beta^i \partial_i$ is called the shift vector. Since $\vec{\beta}$ is orthogonal to $\vec{n}$, i.e. the shift vector lies on the hypersurface Σ_t. Therefore the shift vector can be expressed explicitly as β = -$\gamma \cdot \partial_t$. The line element described by the metric tensor $\boldsymbol{g}$ thus becomes

$$ds^2 = -N^2 dt^2 + \gamma_{ij}(dx^i + \beta^i dt)(dx^j + \beta^j dt). \tag{2.41}$$

The intrinsic curvature of the hypersurface Σ_t is equipped with induced metric γ, whereas the extrinsic curvature describes the way Σ_t is embedded in to spacetime ($\mathscr{M}$, $\mathbf{g}$). It is measurable by the variation of the normal unit vector $\vec{n}$ as one moves on Σ_t. The extrinsic curvature tensor $\mathbf{K}$ is the bilinear form defined on Σ_t by

$$\mathbf{K}(\vec{u},\vec{v}) = -\vec{u}\cdot\nabla_{\vec{v}}\vec{n}. \tag{2.42}$$

The trace of $\boldsymbol{K}$ is

$$K = \gamma^{ij}K_{ij} = -\nabla_\mu n^\mu. \tag{2.43}$$

Projecting Einstein Eqs.2.32 i)twice onto Σ_t, ii) twice along $\vec{n}$ and iii) once on Σ_t and once along $\vec{n}$, one gets the following equations [75, 76].

$$\partial_t K_{ij} - \mathscr{L}_{\vec{\beta}}K_{ij} = -D_iDjN + N({}^3R_{ij} + KK_{ij} - 2K_{ik}K^k_j + 4\pi[(S-E)\gamma_{ij} - 2S_{ij}]) \tag{2.44}$$

$${}^3R + K^2 - K_{ij}K^{ij} = 16\pi E \tag{2.45}$$

$$D_jK^j_i - D_iK = 8\pi p_i \tag{2.46}$$

Where E, p_i and S_{ij} are the matter quantities relative to the ZAMO and are defined by Eq.2.39.

2.3.3 Stationary, axisymmetric and asymptotically flat circular spacetimes

Spacetime is said to be stationary if there exists a one-parameter group of isometries σ_t, whose orbits are timelike curves. Thus, every stationary spacetime possesses a timelike Killing vector field ξ^a. Similarly spacetime is axisymmetric if there exists a one-parameter group of isometries χ_ϕ whose orbits are closed spacelike curves, which implies the existence of a spacelike Killing field ψ^a whose integral curves are closed. Spacetime can be stationary and axisymmetric at the same time if it possesses both these symmetries and if, in addition, the rotations commute with time translations:

$$\sigma_t \circ \chi_\phi = \chi_\phi \circ \sigma_t. \tag{2.47}$$

Or equivalently we can write that the Killing vector fields ξ^a and ψ^a commute

$$[\vec{\boldsymbol{\xi}}, \vec{\boldsymbol{\psi}}] = 0. \tag{2.48}$$

The commutativity of ξ^a and ψ^a implies that we can choose spherical polar coordinates ($x^0 = t$, $x^1 = \phi$, $x^2 = r$, $x^3 = \theta$) so that both $\xi^a = (\partial_t)^a$ and $\psi^a = (\partial_\phi)^a$ are coordinate vector fields. A

stationary axisymmetric spacetime is asymptotically flat if at spatial infinity

$$\begin{aligned} \vec{\boldsymbol{\xi}} \cdot \vec{\boldsymbol{\xi}} &\to -1, \\ \vec{\boldsymbol{\xi}} \cdot \vec{\boldsymbol{\psi}} &\to 0, \\ \vec{\boldsymbol{\psi}} \cdot \vec{\boldsymbol{\psi}} &\to +\infty. \end{aligned} \tag{2.49}$$

A stationary (Killing vector $\vec{\xi}$) and axisymmetric (Killing vector $\vec{\psi}$) spacetime ruled by the Einstein equation is circular if the energy-momentum tensor T obeys

$$\begin{aligned} \xi^{\mu} T_{\mu}[^{\alpha} \xi^{\beta} \psi^{\gamma}] &= 0 \\ \psi^{\mu} T_{\mu}[^{\alpha} \xi^{\beta} \psi^{\gamma}] &= 0 \end{aligned} \tag{2.50}$$

where the square brackets denote a full antisymmetrization [77, 78, 79, 80, 81]. The circularity conditions (Eq. 2.50) imply

$$\vec{u} \in Vect(\vec{\xi}, \vec{\psi}). \tag{2.51}$$

Taking into account that $\vec{\boldsymbol{\xi}} = \vec{\partial_t}$ and $\vec{\boldsymbol{\psi}} = \vec{\partial_\phi}$, the above condition is equivalent to $u^r = 0$ and $u^\theta = 0$, or

$$\vec{u} = u^t(\vec{\xi} + \Omega \vec{\psi}) \tag{2.52}$$

where $\Omega := \frac{u^\phi}{u^t} = \frac{d\phi}{dt}$. The 4-velocity (Eq.2.52) describes a pure circular motion of the fluid around rotation axis.

2.3.4 Einstein equations for rotating stars

The line element for a rotating star in quasi-isotropic coordinates is given by

$$g_{\alpha\beta} dx^\alpha dx^\beta = -N^2 dt^2 + A^2 \left(dr^2 + r^2 d\theta^2 \right) + B^2 r^2 sin^2\theta (d\phi - \omega dt)^2. \tag{2.53}$$

where N, A, B and ω are four functions of (r, θ). Four Einstein equations for rotating star in 3+1 formalism are

$$\begin{aligned} \Delta_3 \nu &= 4\pi A^2 (E + S) + \frac{B^2 r^2 sin^2\theta}{2N^2} \partial\omega\partial\omega - \partial\nu\partial(\nu + lnB) \\ \tilde{\Delta}_3(\omega r sin\theta) &= -16\pi \frac{NA^2}{B^2} \frac{p_\varphi}{r sin\theta} + r sin\theta \partial\omega\partial(\nu - 3\ln B) \\ \Delta_2[(NB - 1) r sin\theta] &= 8\pi N A^2 B r sin\theta (S_r^r + S_\theta^\theta) \\ \Delta_2(lnA + \nu) &= 8\pi A^2 S_\varphi^\varphi + \frac{3B^2 r^2 sin^2\theta}{4N^2} \partial\omega\partial\omega - \partial\nu\partial\nu, \end{aligned} \tag{2.54}$$

where

$$\nu := \ln N \tag{2.55}$$

$$\Delta_2 := \frac{\partial^2}{\partial r^2} + \frac{1}{r}\frac{\partial}{\partial r} + \frac{1}{r^2}\frac{\partial^2}{\partial \theta^2} \tag{2.56}$$

$$\Delta_3 := \frac{\partial^2}{\partial r^2} + \frac{2}{r}\frac{\partial}{\partial r} + \frac{1}{r^2}\frac{\partial^2}{\partial \theta^2} + \frac{1}{r^2 tan\theta}\frac{\partial}{\partial \theta} \tag{2.57}$$

$$\tilde{\Delta}_3 := \Delta_3 - \frac{1}{r^2 sin^2\theta}. \tag{2.58}$$

Terms of the form $\partial\nu\partial\nu$ is defined as

$$\partial\nu\partial\nu := \frac{\partial\nu}{\partial r}\frac{\partial\nu}{\partial r} + \frac{1}{r^2}\frac{\partial\nu}{\partial\theta}\frac{\partial\nu}{\partial\theta}. \tag{2.59}$$

Due to the circularity hypothesis, the fluid 4-velocity with respect to ZAMO can be written as,

$$\vec{u} = \Gamma(\vec{n} + \vec{U}). \tag{2.60}$$

where, $\vec{n}$ are the 4-velocity of the ZAMO, $\Gamma = 1/\sqrt{(1-U^2)}$ and $\vec{U}$ are the Lorentz factor and 3-velocity of the fluid with respect to ZAMO respectively.

The equations of motion are the energy-momentum conservation law,

$$\nabla^\mu T_{\alpha\mu} = 0 \tag{2.61}$$

and the baryon number conservation law $\nabla^\mu(n_B u^\mu) = 0$. Inserting the perfect fluid form of $T_{\mu\nu}$ in Eq.2.61, expanding and projecting orthogonally to the fluid 4-velocity $\vec{U}$[via the projector $\perp^\alpha_\beta$], we get the relativistic Euler equation [82],

$$(\epsilon + P)u^\mu\nabla_\mu u_\alpha + (\delta^\mu_\alpha + u^\mu u_\alpha)\nabla_\mu P = 0. \tag{2.62}$$

Now using Gibbs-Duhem relation and first law of thermodynamics at zero temperature and using properties $u^\mu u_\mu = -1$ and $u^\mu\nabla_\alpha u_\mu = 0$, Eq.2.62 can be written as

$$u^\mu[\nabla_\mu(hu_\alpha) - \nabla_\alpha(hu_\mu)] = 0, \tag{2.63}$$

where $h := \frac{\epsilon+P}{n_B}$. First integral of motion (Eq.2.63) is expressed as

$$\nabla \ln\frac{h}{u^t} + \frac{l}{1-\Omega l}\nabla\Omega = 0, \tag{2.64}$$

where l is specific angular momentum. Eq.2.64 can be rewritten as

$$\nabla(H + \upsilon - \ln\Gamma) + F(\Omega)\nabla\Omega = 0, \tag{2.65}$$

where H:= $\ln\frac{h}{m_B}$, m_B being the mean baryon mass: $m_B \simeq 1.66\times10^{27}$ kg.

2.3.5 Rigid Rotation

If Ω = constant, then $\nabla\Omega = 0$ and Eq. 2.65 becomes

$$H + \nu - \ln\Gamma = const. \tag{2.66}$$

2.3.6 Differential Rotation

If $\nabla\Omega \neq 0$ in the Eq.2.65, the motion is considered as differential rotation. Then first integral of motion is given by

$$H + \nu - \ln\Gamma + \int_0^{\Omega} F(\Omega')d\Omega' = const, \tag{2.67}$$

where

$$F(\Omega) = \frac{B^2(\Omega - \omega)r^2 sin^2\theta}{N^2 - B^2(\Omega - \omega)^2 r^2 sin^2\theta}. \tag{2.68}$$

2.3.7 Rotation in Hot Stars

For hot stars equation of fluid motion is given by

$$\partial_i(H + \nu - \ln\Gamma) = \frac{Te^{-H}}{m_B}\partial_i s_B - F\partial_i\Omega. \tag{2.69}$$

If both T=0 and $\partial_i\Omega = 0$ then equation of motion turns out to be Eq.2.66. For T=0 equation of motion turns out to be Eq.2.67.

2.3.8 Numerical Process

In this section we will discuss BGSM algorithm[60] used to solve barotropic perfect fluid stars. BGSM algorithm can be applied to homoentropic fluid stars, where the specific entropy is constant which effectively makes the EoS of the star barotropic. Algorithm to construct rotating equilibrium model numerically is also called as self-consistent-field method. A simple sketch of it is given below:

First of all a finite temperature EoS of the form $[\varepsilon_B(H, s_B),\ P(H, s_B)]$ is chosen. We assume $H = 0$ corresponding to $P = 0$ on the surface, central value H_c of the log-enthalpy H and angular velocity Ω in case of rigid rotation or central angular velocity Ω_c for differentially rotating stars plus a rotation law of the form $F = F(\Omega)$. In addition, four metric functions N, ω, A, B are set to one. Next, U is initialised to zero and the profile of enthalpy is taken as $H = H_c(1 - \frac{r^2}{R^2})$ where the value of R is chosen around the expected radius of the final model. Then,

1.Compute $\varepsilon_B(H, s_B)$ and $P(H, s_B)$ from the EoS.

2.The energy-momentum tensor is expressed in terms of the matter sources E, p_φ, [Eqs. 2.39].

With the help of U, Γ, ε and P, compute the matter sources E, p_φ, S, S^r_r, S^θ_θ, S^φ_φ that appear in the right-hand side of Einstein equations Eqs. 2.54.
3.Solve Einstein Eqs.2.54, using the current values of ν, ω, A and B on their right-hand sides, there by obtaining new values of $N = \exp\nu$, ω, A and B.
4.From the expression $U = \frac{B}{N}(\Omega - \omega)r\sin\theta$, obtain the value of Lorentz factor through the formula $\Gamma = (1 - U^2)^{-1/2}$
5.The Eq.2.66 can be rewritten as $H = H_c + \nu_c - \nu + \ln\Gamma$ to compute H in all space. Go to step 1.
This numerical method gives a unique solution for a given value of input parameters(H_c, Ω) and a fixed EoS.

2.3.9 Equilibrium quantities of the rotating stars

In this section we will discuss about the equilibrium quantities of the rotating stars i.e, total baryon number, baryon mass, gravitational mass, angular momentum, virial identities, circumferential radius, T/W etc [24, 83, 84].

2.3.9.1 Baryon and Gravitational Mass

Total number of baryons in the star can be expressed in terms of baryon number density $(n_B = \frac{\epsilon+P}{m_B}\exp(-H))$ as follows:

$$\mathscr{N} = \int_{\Sigma_t} \Gamma n_B A^2 B r^2 \sin\theta dr d\theta d\phi. \tag{2.70}$$

We can convert $\mathscr{N}$ to baryonic mass (M_B), multiplying it by the mean baryon mass $m_B \approx 1.66 \times 10^{-27} kg$

$$M_B = m_B \mathscr{N}. \tag{2.71}$$

There are two major concepts of mass in general relativity [76, 85, 86]: i)The Komar mass which is applied only for stationary spacetimes, ii)The ADM mass which applies to any asymptotically flat spacetimes.

Komar Mass
For the given Killing vector, associated with stationary spacetime $\vec{\boldsymbol{\xi}}$, the Komar mass is

$$M = -\frac{1}{8\pi}\oint_{\mathscr{S}} \nabla^\mu \xi^\nu dS_{\mu\nu}, \tag{2.72}$$

where $\mathscr{S}$ is any closed 2-surface (sphere) and $dS_{\mu\nu}$ is the area-element 2-form normal to $\mathscr{S}$. If $\mathscr{S}$ is defined by r = constant, the area element is spanned by the coordinates (θ, ϕ) and is given by

$$dS_{\mu\nu} = (s_\mu n_\nu - s_\nu n_\mu)\sqrt{q}d\theta d\phi, \tag{2.73}$$

where the n_μ's are given by $n_\mu = (-N, 0, 0, 0)$, s_μ's are the covariant components of the unit normal $\vec{\mathbf{s}}$ of $\mathscr{S}$ in (Σ_t,γ) and is given by $s_\mu = (0, A, 0, 0)$. On the other hand, $q = A^2B^2r^4\sin^2\theta$ is the determinant of the components q_{ab} of the metric induced by γ on $\mathscr{S}$.
By using Gauss-Ostrogradski theorem, Eq.2.32 and Killing Eq. $\nabla_\alpha\xi_\beta + \nabla_\beta\xi_\alpha = 0$, Eq.2.72 can be written as

$$M = 2\int_{\Sigma_t}[\boldsymbol{T}(\vec{\boldsymbol{n}}, \vec{\boldsymbol{\xi}}) - \frac{1}{2}T\vec{\boldsymbol{n}}\cdot\vec{\boldsymbol{\xi}}]\sqrt{\gamma}drd\theta d\varphi, \tag{2.74}$$

where $\boldsymbol{T}$ is the energy-momentum tensor and $T := g^{\mu\nu}T_{\mu\nu}$ is the trace with respect to $\boldsymbol{g}$. By using Eq.2.38 for stress-energy tensor and making use of $\vec{\boldsymbol{\xi}} = N\vec{n} + \vec{\beta}$ with $\vec{\partial}_t = \vec{\boldsymbol{\xi}}$ in Eq.2.74 we get

$$M = \oint_{\sum_t}[N(E+S) + 2\omega B(E+P)Ur\sin\theta]A^2Br^2\sin\theta drd\theta d\phi, \tag{2.75}$$

where Σ_t is the hypersurface in four dimensional spacetime.

ADM Mass

The ADM mass has been introduced by Arnowitt, Deser & Misner [87] for any asymptotically flat spacelike hypersurface Σ_t. It is expressed as [76, 85]

$$M_{ADM} = \frac{1}{16\pi}\lim_{\mathscr{S}\to\infty}\oint_{\mathscr{S}}[D^j\gamma_{ij} - D_i(f^{kl}\gamma_{kl})]s^i\sqrt{q}\,d\theta d\varphi. \tag{2.76}$$

The expressions for gravitational mass in Eqs.2.74 and 2.76 look different, for stationary spacetime. The ADM mass is equal to Komar mass, provided Σ_t is orthogonal to Killing vector $\vec{\boldsymbol{\xi}}$ at spatial infinity, which implies

$$M_{ADM} = M. \tag{2.77}$$

Binding energy

The binding energy of the star is defined by as the difference between the gravitational mass and baryon mass

$$E_{bind} = M - M_B, \tag{2.78}$$

where $|E_{bind}|$ is the energy required to disperse all the constituent particles of the star to infinity. The star is bound if $E_{bind} < 0$, and is unstable if $E_{bind} \geq 0$.

2.3.9.2 Virial Identities

Equilibrium configurations in Newtonian gravity satisfy the well-known virial relation

$$2T + 3(\Gamma - 1)U + W = 0,$$

that can be used to check the accuracy of computed numerical solutions. GRV2 and GRV3 are two such relativistic virial identities, valid for asymptotically flat spacetimes [88].

GRV3

GRV3 is generalization of Newtonian virial theorem in General relativity, "3" implies integral is a 3-dimensional one. For rotating star, GRV3 is expressed as

$$\begin{aligned}\int_{\Sigma_t} \quad & \{4\pi S - \frac{1}{A^2}(\partial\nu\partial\nu - \frac{1}{2AB}\partial A\partial B) + \frac{1}{2r}(\frac{1}{A^2} - \frac{1}{B^2})[\frac{1}{A}(\frac{\partial A}{\partial r} + \frac{1}{r\tan\theta}\frac{\partial A}{\partial\theta}) \\ & -\frac{1}{2B}(\frac{\partial B}{\partial r} + \frac{1}{r\tan\theta}\frac{\partial B}{\partial\theta})] + \frac{3B^2\sin^2\theta}{8r^2A^2N^2}\partial\omega\partial\omega\}A^2Br^2\sin\theta dr d\theta d\varphi = 0 \end{aligned} \tag{2.79}$$

where S is the stress tensor.

GRV2

GRV2 on contrary to GRV3 involves a 2-dimensional integral [89]. For rotating star, GRV2 is expressed as

$$\int_{r=0}^{r=+\infty}\int_{\theta=0}^{\theta=\pi}\{8\pi A^2[P + (E+P)U^2] + \frac{3B^2r^2\sin^2\theta}{4N^2}(\partial\omega\partial\omega - \partial\nu\partial\nu)\}r dr d\theta = 0. \tag{2.80}$$

Komar Angular Momentum

The Komar angular momentum is defined by

$$J = \frac{1}{16\pi}\oint_{\mathscr{S}}\nabla^\mu\psi^\nu dS_{\mu\nu}\ , \tag{2.81}$$

where $\mathscr{S}$ is any closed 2-surface(sphere) surrounding the star, $dS_{\mu\nu}$ is the area-element 2-form normal to $\mathscr{S}$ given by Eq.2.73 and ψ^ν are components of axisymmetry Killing vector $\tilde{\psi}$. Using Gauss-Ostrogradski theorem and Einstein equation, we can get a volume expression similar to Eq.2.74, after simplification the equation reduces to

$$J = \int_{\Sigma_t}(E+P)UA^2B^2r^3\sin^2\theta dr d\theta d\varphi. \tag{2.82}$$

Circumferential radius

The equatorial radius R_e is the closed line at the surface of the star defined by t = constant and $\theta = \pi/2$(equatorial plane). On the other hand, the coordinate-independent charaterization of the stellar equator is the circumferential radius, as follows:

$$R_{circ} = \frac{1}{2\pi} \oint_{r=R_e,\theta=\pi/2} ds = \frac{1}{2\pi} \oint_{r=R_e,\theta=\pi/2} \sqrt{B^2 r^2 \sin^2\theta d\varphi^2} = \frac{B(R_e,\pi/2)R_e}{2\pi} \int_0^{2\pi} d\varphi. \quad (2.83)$$

$$\Rightarrow R_{circ} = B(R_e,\pi/2)R_e. \quad (2.84)$$

At Newtonian limit, $B = 1$ hence $R_{circ} = R_e$.

Chapter 3

Properties of rapidly rotating hot neutron stars with K^- condensates

3.1 Introduction

A NS is born in a core-collapse supernovae (CCSN) explosion, which is believed to be adiabatic, i.e., the entropy per baryon (s) of each mass element remains constant during the collapse except during the passage of the shock [90]. About fifty seconds after birth, the stellar interior becomes fully transparent to the neutrinos [91]. Some processes, e.g., frictional dissipation of the rotational energy or Ohmic decay of the internal magnetic field, may reheat stellar interior thus delaying the cooling, especially at these late stages [92]. The exotic composition of the cores such as quarks or kaon/pion condensates, affects the neutrino emission mechanism and hence its cooling properties [92]. Higher the threshold density, slower will be the cooling of compact stars via kaon condensation [93]. The temporal evolution of static proto-neutron stars (PNS) has been thoroughly studied by Pons et. al. [64]. In this work, we are interested in studying a rotating NS that is born in an adiabatic environment. We assume a range of isentropic profile for the hot star. The maximum value of s reached by a PNS can be $1 - 2k_B$ [64], which may increase to $5k_B$ for high mass progenitor[94] or merger of NSs [95]. For simplicity, we have restricted ourselves to a deleptonised star at constant s [59], so that neutrinos do not contribute to the lepton number of the matter. The calculations are done for a hot star containing exotic matter such as K^- condensates and that is yet to cool down to Fermi temperature.

We consider an idealised scenario of uniform and rigid rotation about an axisymmetric axis which represents an approximation to the actual rotational state of a hot NS [59]. We study the rotating NS sequences with EoS containing exotic particles and having different entropies. These results are compared with the corresponding static configurations and also with the nucleon only matter configuration for a better understanding. Further, we study the relativistic equilibrium

configurations of rotating hot NS with different EoS and thermodynamic conditions, in terms of their fluid energy density profiles. We also study how they are affected by the change in rotation frequency (or angular momentum) upto the Keplerian limit.

We also make a rough estimate of gravitational wave (GW) amplitude emitted by a NS having strong magnetic field (B). Most NSs are the superdense remnants of supernova explosions but some are formed in binary NS merger as well. Some NS may have very high magnetic fields and are called magnetars. The origin of high B in such NS is an open ended problem. Simulations show that a magnetar which is formed after the merger of binary NS, is differentially rotating and ultraspinning with typical periods of the order of a few milliseconds and magnetic field strengths in the range of [96] $B \sim 10^{15} - 10^{16}G$. The NS magnetic field ($B \sim 10^{12}G$) is amplified by several orders of magnitude ($B \geq 2 \times 10^{15}G$) within the first millisecond after merger [97]. The differential rotation can further increase the field. Further, the long term evolution models have shown that the magnetic field can lead to a uniformly rotating NS surrounded by an accretion disk and with a collimated magnetic field [98]. On the other hand, observations have shown that the NSs that are relatively old, have strong magnetic fields which are of the order of $B \sim 10^{11}$ G to $10^{13.5}$ G, but much longer periods (P $\sim$ 1 s). Whereas, millisecond radio pulsars have ultra-fast rotation (P $\leq$ 20 ms) and much weaker magnetic fields ($B \leq 10^{10}$ G)[99]. Since we are interested in young and hot NS, we take a typical magnetar formed in a merger event for the estimation of GW amplitude.

3.2 Results

We have generated a number of isentropic EoS profiles and calculated the properties of a reasonably rapidly rotating and deleptonised NS using DD2 model. We consider nucleons-only system consisting of protons (p), neutrons (n) and leptons (l); and denote it by "np". When the matter consists of antikaon condensates (K^-) and thermal kaons (K^T), it is denoted by "npK". The potential depth of antikaons in saturated nuclear matter is given by, $U_{\bar{K}} = -g_{\sigma K}\sigma + g_{\omega K}\omega_0$. The study of kaonic atoms suggests an attractive optical potential for the antikaons. The value of $U_{\bar{K}}$ at n_0 has been calculated in a coupled-channel model and chiral analysis of K^- atomic and scattering data. However, till date, no definite consensus exists regarding the value of $U_{\bar{K}}$ [52, 71]. For our calculations, we have chosen a wide range for $U_{\bar{K}}$, from a shallow value of -60 MeV to a deeper one of -150 MeV [52]. The coupling constants for kaons at saturation density for different values of $U_{\bar{K}}$ in the DD2 model are listed in Table 2.2 [15].

In the left panel of Fig. 3.1, we plot pressure vs. baryon number density or the EoS profile for np and npK matter ($U_{\bar{K}}$ = -100 MeV) for different s values. We notice that the set of npK EoS is softer compared to that of np matter. As we go from np to npK matter, leptons in the NS core are gradually replaced first by thermal kaons and later by antikaon condensates also as the

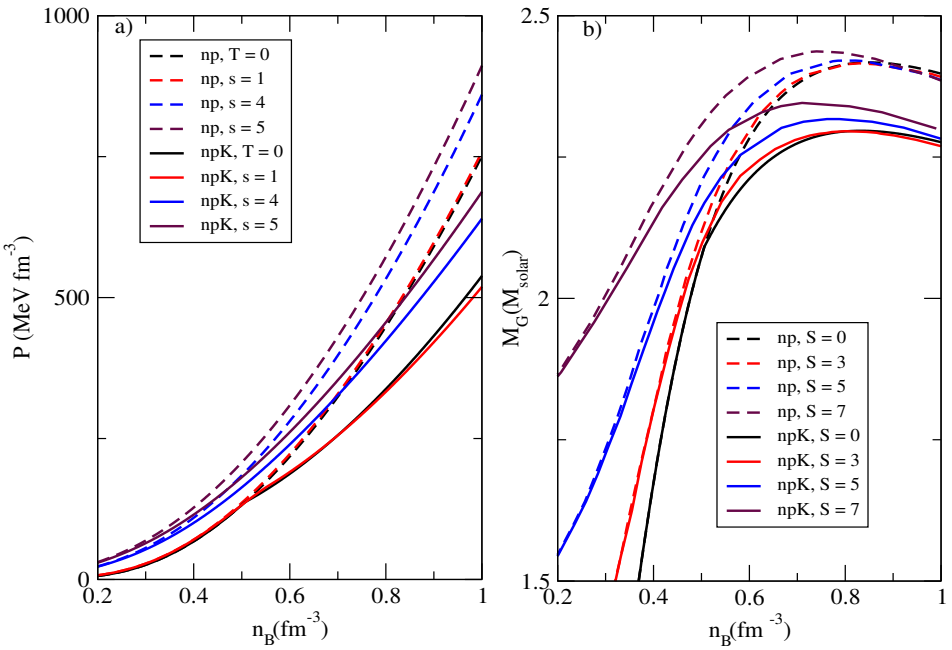

FIGURE 3.1: a) The EoS with pressure plotted against number density for np and npK ($U_{\bar{K}}$ = -100 MeV) for a NS core at zero temperature state (T = 0 MeV) and at adiabatic state (entropy per baryon s = 1, 4 and 5). b) The mass sequences against number densities for the np and npK ($U_{\bar{K}}$ = -100 MeV) EoS, for total entropy S = 0, 3, 5 and 7 M_{solar}. The dashed lines are for np matter and solid lines are for npK matter for $U_{\bar{K}} = -100$ MeV in both the panels.

core density increases. These condensates do not contribute to the pressure term but they do contribute to the net negative charge in the system and hence the overall EoS becomes softer.

We also compare the hot NS EoS having different s values (1, 4 and 5) with EoS for cold NS matter (T=0 MeV). In this thesis, we have used natural units with $k_B = 1$, wherever required. In general, for a given composition, the EoS is softer for a NS with lower s. This matches with the previous results for other model EoS [18]. At a given density, higher s matter has higher chemical potential and hence higher pressure, as is evident from the Gibbs-Duhem relation. We further notice that the EoS profiles for $s = 1$ NS matter is only slightly different than that for cold NS matter for np, but this difference between the two EoS is more evident for npK composition. The np EoS is slightly stiffer for matter at $s = 1$ than for matter at zero temperature, as expected, because kinetic pressure increases due to increase in temperature, but the potential pressure term remains the same.In contrast, for npK, $s = 1$ EoS is comparatively softer than zero temperature EoS, especially at higher densities ($n_B \geq 0.7$).

For cold NS matter, the npK EoS which was initially following the np EoS, bends at the density point when antikaon condensates start appearing at $n_B \sim 0.5$. Since there are no thermal kaons present at T= 0 MeV, it is only the presence of antikaon condensates which contributes to the softening of EoS.For $s = 1$ NS, the npK EoS follows the corresponding np EoS until thermal kaons enter, at which point the slope of the EoS curve changes slightly due to reduction in pressure. Further when the antikaon condensates appear at later density, the curve bends again

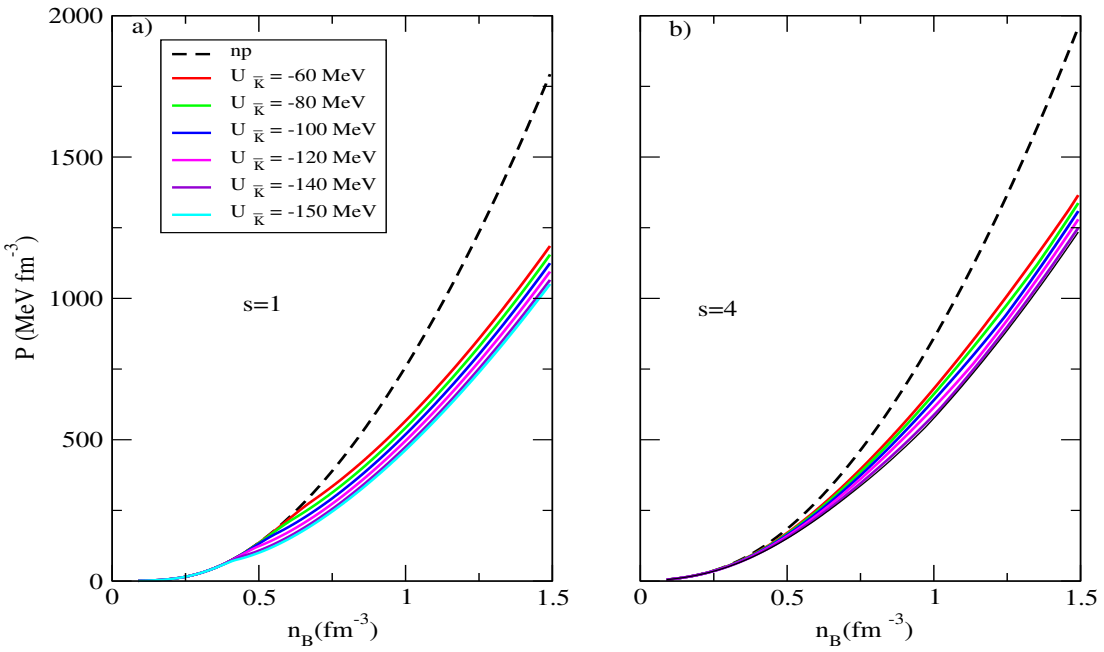

FIGURE 3.2: The EoS is plotted for a range of values of $U_{\bar{K}} = -60MeV$ to $-150MeV$ a) for lower $s = 1$ and b) for higher $s = 4$. In both the plots np EoS is also included as the dashed line for comparison.

further softening the EoS. The fraction of antikaon condensates becomes more than that of thermal kaons at about $n_B \sim 0.62$ and soon after we see EoS becoming so soft that T = 0 MeV EoS becomes stiffer than $s = 1$ EoS.

If we look at the expression for pressure in Eq. 2.18, contribution of the first three terms, i.e., the potential terms is more for a low s NS matter. Even though with the rise in temperature, contribution of the kinetic terms increases, it dominates only at sufficiently high s values ($s \geq 2$) where thermal kaons play a significant role. In contrast, the contribution of potential term decreases with an increase in s value. This decrease is maximum for low s NS and minimum for high s NS. This is because in a high s NS, the thermal kaons appear at lower density and their fraction in the system is also relatively high compared to a NS at lower s; as will be seen in Figs. 3.4 and 3.5. On the other hand the fraction of K^- is lower for a higher s NS and they appear at higher densities only. In addition, the kinetic increase in pressure is also there due to high temperatures, so the overall EoS for high s NS is stiffer than for a cold star. This, however, may become softer at higher densities where K^T overtakes K^- as was seen for the case of $s = 1$ earlier. In general, we can say that a cold EoS which is initially softer than a higher s EoS, may become stiffer at very high densities.

The EoS profile obeyed by a NS is reflected in its mass-density profile. We next study NS gravitational mass sequences for static as well as rotating stars obeying different EoS. To get mass profiles of a static NS, we solve TOV equations for the same, with our sets of EoS. For the cold NS, the maximum masses of about 2.417 M_{solar} and 2.372 M_{solar} can be attained for np

TABLE 3.1: Maximum mass reached for different np and npK EoS and the corresponding central number density at constant total entropy values of 0, 3 and 7 M_{solar}. The first row is for np EoS with no antikaon contribution and the rest five rows are for npK EoS at different $U_{\bar{K}}$s.

	$U_{\bar{K}}$	S=0M_{solar}		S=3M_{solar}		S=7M_{solar}	
		M_{max}	n_B	M_{max}	n_B	M_{max}	n_B
	MeV	(M_{solar})	(fm^{-3})	(M_{solar})	(fm^{-3})	(M_{solar})	(fm^{-3})
np		2.417	0.851	2.416	0.829	2.437	0.740
npK	-60	2.372	0.822	2.376	0.792	2.386	0.718
	-80	2.339	0.823	2.341	0.799	2.369	0.727
	-100	2.297	0.833	2.296	0.8	2.346	0.729
	-120	2.242	0.862	2.237	0.825	2.315	0.731
	-140	2.176	0.914	2.164	0.841	2.275	0.716
	-150	2.142	0.95	2.125	0.912	2.251	0.722

and npK matter respectively, after which the star becomes unstable as the slope, $\frac{dM_G}{dn_B}$, becomes negative. For hot, rotating stars, Goussard *et al.*. [59], based on the earlier papers [43, 100] have shown that a stable configuration can be distinguished from the unstable one following the gravitational mass sequences at constant total entropy $S = s \times M_B$, instead of constant s. We use this criterion to find mass sequences for np and npK ($U_{\bar{K}}$=-100MeV) EoS and plot gravitational mass-number density ($M_G - n_B$) profile for different entropy values in the right panel of Fig. 3.1. The plotted sequences are for S of 0, 3, 5 and 7 M_{solar} NS.

The sequence for a $S = 3$ M_{solar} corresponds to NS configurations with an s between 1 (for the higher M_G end of the sequence) and 2 (for lower M_G end). The maximum mass reached corresponds roughly to a NS at $s \sim 1.1$. Since the configurations at higher end are lower in s, we see very minor difference there between a cold NS sequence and a NS sequence at $S = 3$ M_{solar}, essentially reflecting the EoS nature, where we saw hardly any difference between cold EoS and $s = 1$ EoS. The higher S sequences of 5 and 7 M_{solar} correspond respectively to an s of (1.8 - 3.8) and (2.5 - 5) respectively, where the values inside parentheses correspond to higher and lower end of the sequence. These sequences are sharply different from the corresponding cold NS sequence, as the thermal effects are more dominant here. A high total entropy can sustain a higher gravitational mass as is evident from the figure. For a given constant S, we get gravitational mass values until a limiting s is reached, beyond which the sequence possibly enters the instability region. The maximum stable mass reached in a sequence as a result and the corresponding central number density for given S of 0, 3 and 7 M_{solar}, are listed in Table 3.1 for np and npK EoS with different $U_{\bar{K}}$. We observe that colder stars have a denser core than finite temperature NS. The central density further decreases as the entropy of a star increases. We see that, e.g., for a NS with $U_{\bar{K}}$ =-100 MeV, the mass increases from 2.297 M_{solar} for cold NS to 2.346 M_{solar} for a NS at $S = 7M_{solar}$, whereas its central density decreases from 0.833 fm^{-3} to 0.729 fm^{-3}. We refrain from quoting radius values for finite temperature stars as the surface pressure never really goes to zero.

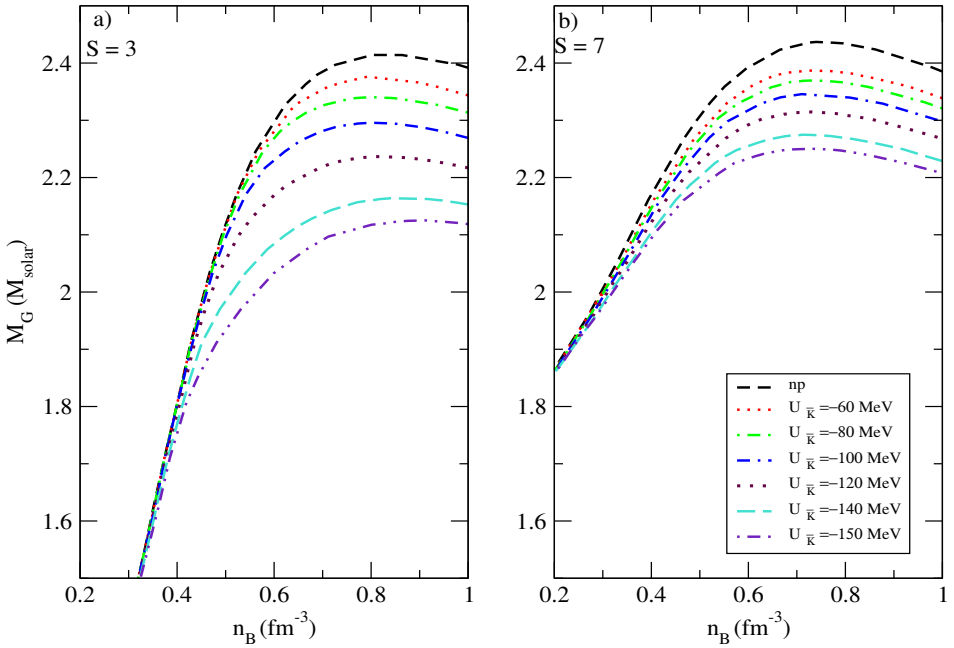

FIGURE 3.3: The mass-number density profiles for EoS with np and npK matter at different optical potentials at for a) S=3M_{solar} and b) S = 7M_{solar}.

We next study the EoS profiles of hot NS having different $U_{\bar{K}}$ values. In Fig. 3.2, we compare np and npK EoS profiles for two different values of s: 1 and 4. The npK lines are plotted for a range of $U_{\bar{K}}$ from -60 MeV to -150 MeV for K^- condensates in a nuclear medium. We notice that as soon as the thermal kaons enter the system, the slope of corresponding EoS changes. The EoS gets further softened at higher densities when the antikaon condensates appear. The densities at which the thermal kaons and the condensates appear in the NS core, for different $U_{\bar{K}}$ values, are listed in Table 3.2. For a given value of $U_{\bar{K}}$, K^- condensates appear at lower density for a cold NS whereas their appearance is delayed to higher densities for hot NS. Thermal kaons are not present in cold NS. For finite temperature NS, not only the K^T's appear much earlier than K^- but for higher s they appear at lower densities. The condensates do not appear in the system even at very high densities ($n_B \sim 1.3 fm^{-3}$) for a high s (~ 5) NS, unless the optical potential is deep enough, $\left|U_{\bar{K}}\right| \geq 100$ MeV. Hence, in a NS core, an increase in s delays the K^- onset in the system but advances the onset on K^T, thereby making the EoS stiffer. It is to be noted that np EoS is the stiffest among all considered here because neither K^- nor K^T exist in the system ever. In contrast, for a NS at given s, as the depth of optical potential increases, the condensates as well as thermal kaons start populating the core earlier, thereby making the corresponding EoS softer.

Next, we study the NS mass sequences at constant S for np and npK EoS. The $M_G - n_B$ profiles are compared in Fig. 3.3 for constant total entropy of 3 M_{solar} and 7 M_{solar} in the two panels, which roughly translates to an s of $\sim$ 1.1 and 2.7, respectively, for the higher M_G end of a sequence. As before, nature of the EoS is reflected in the corresponding mass profile. For the

TABLE 3.2: The value of baryon density (n_B) in fm^{-3} when K^T and K^- condensate start appearing in the NS core. They are for different values of $U_{\bar{K}}$ and also for different thermodynamic states inside the NS core.

$U_{\bar{K}}$ MeV	T=0 MeV	s=1		s=2		s=3		s=4		s=5	
	K^-	K^T	K^-	K^T	K^-	K^T	K^-	K^T	K^-	K^T	K^-
-60	0.613	0.427	0.687	0.282	0.868	0.191	1.129	0.131	1.396	0.092	-
-80	0.558	0.393	0.622	0.264	0.777	0.18	1.006	0.125	1.245	0.089	-
-100	0.507	0.362	0.559	0.246	0.690	0.171	0.889	0.121	1.097	0.089	1.312
-120	0.459	0.334	0.502	0.231	0.608	0.162	0.777	0.115	0.957	0.089	1.126
-140	0.416	0.308	0.449	0.218	0.535	0.155	0.674	0.11	0.828	0.089	0.969
-150	0.395	0.297	0.425	0.21	0.449	0.15	0.626	0.109	0.765	0.089	0.896

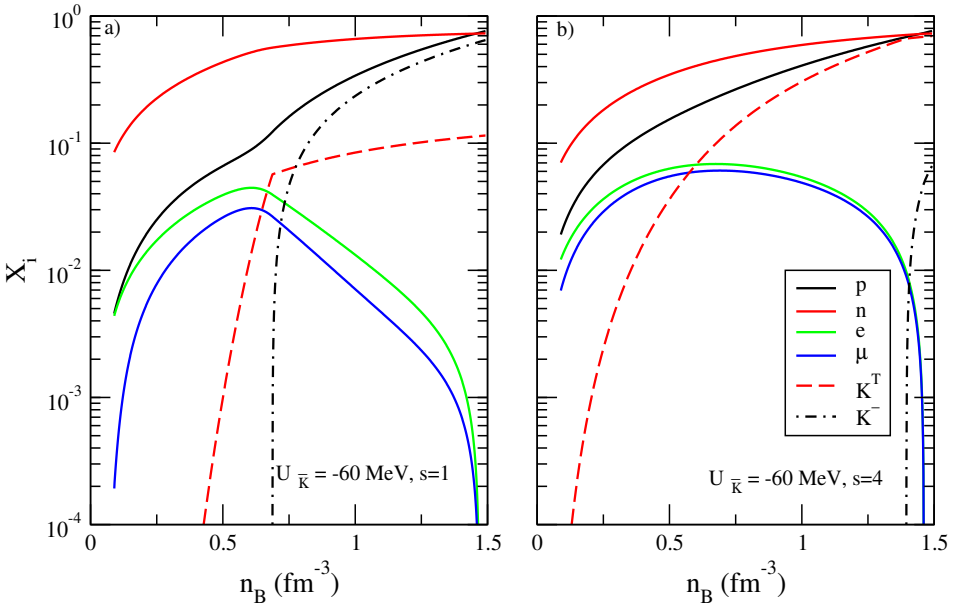

FIGURE 3.4: Particle densities of n, p, e, μ and antikaon condensates of K^- and K^T in β-equilibrated NS matter; for $U_{\bar{K}} = -60$ MeV; plotted as a function of the baryon density for a) $s = 1$ and b) $s = 4$.

same thermodynamic condition, a softer EoS (deeper $U_{\bar{K}}$) makes a lower maximum mass star, The maximum masses reached by NS obeying a given EoS are listed in Table 1. This trend matches with earlier results [19, 64], however, the maximum mass values for cold NS are much higher and well above the observational constraint of $2M_{solar}$ [7, 8, 32].

We next study the particle densities present in the NS core for EoS with different values of $U_{\bar{K}}$ and s. At low densities, the NS contains n, p, e and μ. As higher densities are reached in a NS core, the threshold condition; $\mu_{K^-} = \mu_n - \mu_p = \mu_e$ is satisfied and K^- appears in the system. The lepton fraction falls off as soon as the negatively charged condensates populate. The Bose-Einstein condensates do not contribute to the pressure and it is energetically favourable to have them in the system as compared to the leptons. We compare particle fractions in a hot NS with shallower $U_{\bar{K}} = -60MeV$, for an s value of 1 and 4 in the two panels of Fig. 3.4.

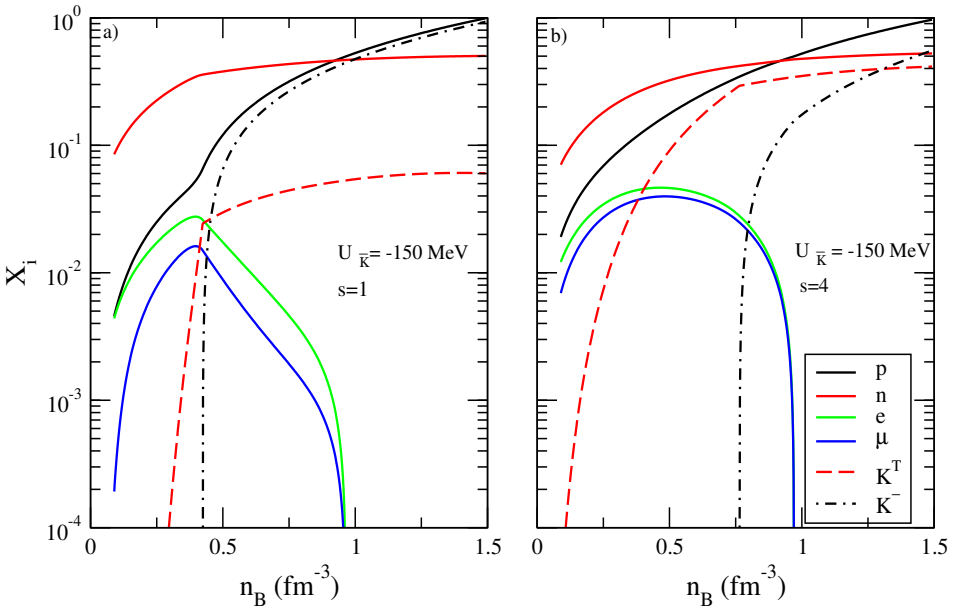

FIGURE 3.5: Particle densities of n, p, e, μ and antikaon condensates of k^-, K^T as a function of baryon number density as in Fig 3.4, but for a deeper $U_{\bar{K}} = -150$ MeV for a) $s = 1$ and b) $s = 4$.

Interestingly, in a low s NS core, as soon as K^- condensates appear, they quickly outnumber the already existing thermal kaons K^T. On the other hand, in a higher s NS, the negatively charged K^T appear at relatively lower density, pushing the onset of K^- condensates to much higher n_B values. K^T was also noted to partially inhibit the appearance of the K^- condensates in Pons et. al. [64]. In Fig. 3.5, the particle fraction is plotted for a deeper $U_{\bar{K}} = -150MeV$. A similar trend is noticed here as well. However, here the K^- populates at lower densities compared to NS with shallower EoS. The threshold densities for onset of K^T as well as for K^- condensation for different s and $U_{\bar{K}}$ values were listed earlier in Table 3.2.

Next we study the relation between temperature and number density (T vs. n_B) in a NS obeying different EoSs. We plot T vs. n_B in the two panels of Fig. 3.6 for a NS with an s of 1 and 4 respectively. In each panel, we compare np with npK matter at shallow and deep optical potentials. For a fixed s, the temperature increases with increase in baryon density. In other words, the temperature falls off from the core of a NS to its surface. This nature of temperature curve was earlier reported in Banik et al. [101] as well. At a given s, temperature is nearly the same at low densities for different EoS, but in the high density region prominent difference can be seen between them which occurs because the thermal kaons and antikaon condensates start to populate the matter at these densities. We notice kinks in the npK lines which mark the appearance of K^- condensates. For an isentropic NS with a high s of 4, the temperature can rise up to 150 MeV compared to 50 MeV for a star with low s of 1. Also, in a lower s NS, the core temperature is less for np matter as compared to that for npK matter.

For a lower s NS, the antikaons not only appear at lower density, their fraction is higher for

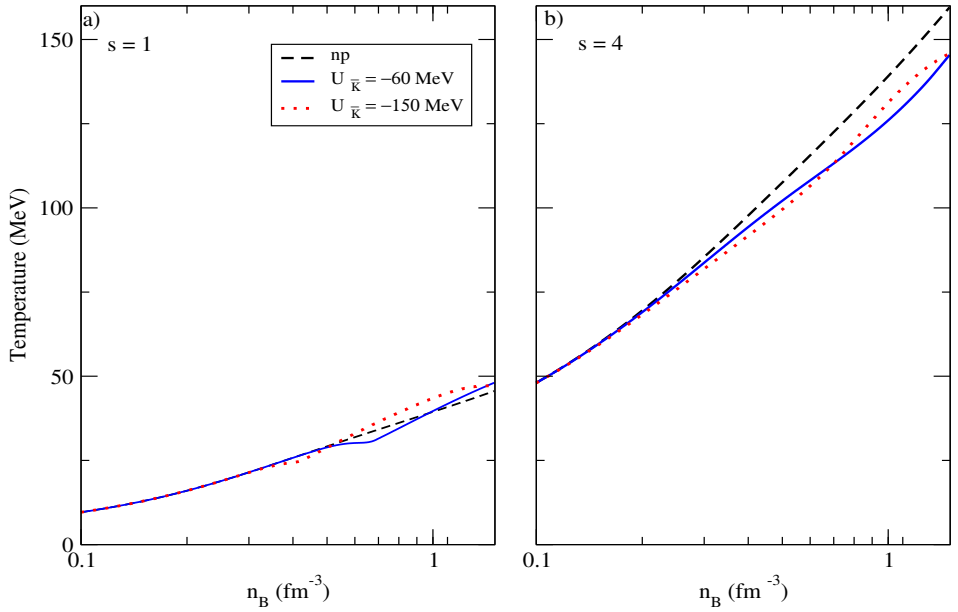

FIGURE 3.6: Temperature in a NS is plotted as a function of baryon density n_B, for a given thermodynamic state, a) $s = 1$ and b) $s = 4$.

deeper potential EoS. Thus the core temperature rises for npK EoS with $U_{\bar{K}} = -150$ MeV, than for that of np EoS or npK EoS at $U_{\bar{K}} = -60$ MeV. For npK at $U_{\bar{K}} = -60$ MeV and $s = 1$, leptons depletion starts at the onset of thermal kaons (at $n_B = 0.427 fm^{-3}$) and the temperature curve of npK is lower than that for np EoS. The lepton depletion is accelerated when condensates appear (at $n_B = 0.687 fm^{-3}$) and the temperature curve surpasses that for np. For a higher s star the nature of temperature curve is quite the opposite. Here, the core temperature of NS with np EoS is higher than that of npK. At higher s, the K^- condensates appear at very high densities (see Table 3.2). Similar behavior is noted when additional fermionic degrees of freedom, such as hyperons are involved. In the absence of any variation of hyperon effective mass, it was shown that at a given baryon density a system with more components has lower temperature [102].

Having discussed the properties of a static NS with np and npK EoS, we now study the rotating NS configurations using *Lorene/nrotstar*. We certainly don't claim to give a completely realistic picture of a NS. This simplified picture of uniformly rotating isentropic, neutrino-less star at beta equilibrium is sufficient for the purpose of present work which is to study the influence of antikaon condensates on the properties of hot, rotating NS. A more complete study of neutrino-trapped PNS with our density-dependent EoS is left for future work. Keeping in consideration the observational pulsar frequency data, we study the change in the NS configuration for different angular momentum values.

Fig. 3.7 shows the evolution of gravitational mass−number density relation of a NS with change in its angular momentum. We plot the $M_G - n_B$ profiles of a NS for different angular momentum

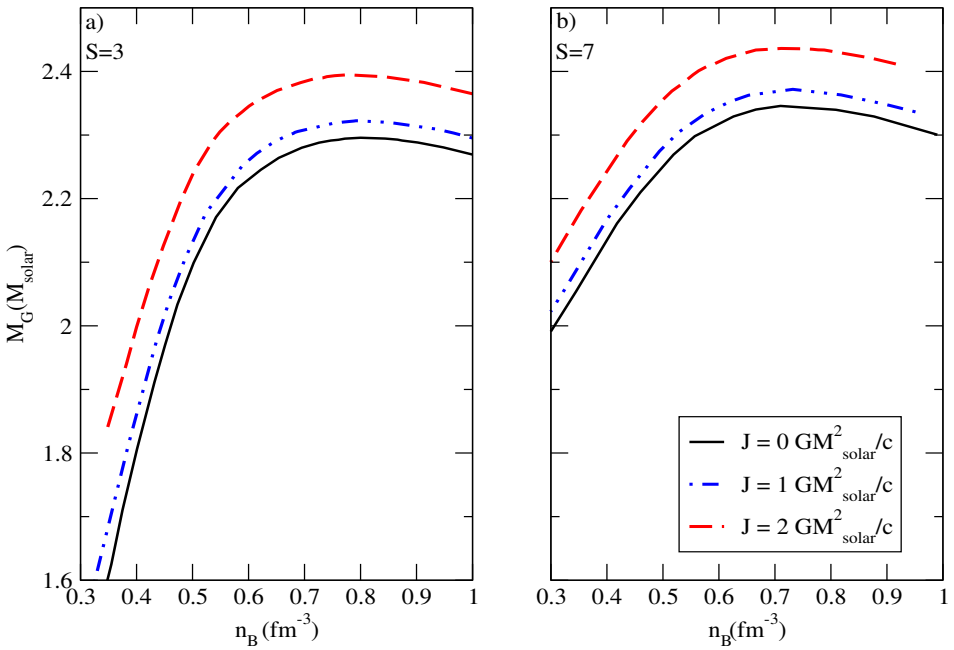

FIGURE 3.7: The evolution of mass with rotation for a NS with npK ($U_{\bar{K}} = -100$ MeV) and at a) S = $3M_{solar}$ and b) S = $7M_{solar}$. The sequences are plotted for NS rotating with different angular momenta starting from J=0 (static case) to $J = 1GM^2_{solar}/c$ and $2GM^2_{solar}/c$.

values ($J = 0, 1$ and $2GM^2_{solar}/c$). The mass sequences for EoS with npK for a moderate optical potential ($U_{\bar{K}} = -100MeV$) plotted in the two panels are for a NS with an S of 3 and $7M_{solar}$, respectively. We see that a rotating star can support more mass compared to a static one. As the angular momentum changes from 0 to $1GM^2_{solar}/c$, the corresponding increase in M_G is not very significant. But the relative change in M_G for a NS with $J \sim 1GM^2_{solar}/c$ to $2GM^2_{solar}/c$ is significant, as is evident from both the panels of Fig. 3.7. The star with total entropy $7M_{solar}$ can support a maximum mass star which is more massive than that with total entropy $3M_{solar}$. The difference is independent of its angular momentum. However, we notice that the relative increase in NS mass from a lower J to higher J state is higher for a NS with lower S. The percent increase in NS mass was about 4.5 for S=3 NS sequence as we go from non rotating state to $J \sim 2GM^2_{solar}/c$ state, whereas it was only 3.85 percent for S=7 NS for the same change in angular momentum state.

We next study the change in shape of a NS for an increase in s and for a change in its angular momentum. In Fig. 3.8 we compare a NS rotating at 300 Hz for two extreme npK EoS (with shallower $U_{\bar{K}} = -60MeV$and with deeper $U_{\bar{K}} = -150MeV$). The iso-contours lines drawn are of constant fluid energy density in the meridional plane, $\phi = 0$. The vertical direction (y) is aligned with the stellar angular momentum. The thick solid line marks the stellar surface. The coordinates (x, z) are defined by $x = rsin\theta$ and $z = rcos\theta$, where θ is the polar angle. They represent the coordinate radii in x and z directions. The upper slice of the Fig. 3.8 is for a NS with shallower EoS and bottom slice for EoS with deeper potential. Both NS are at a constant s

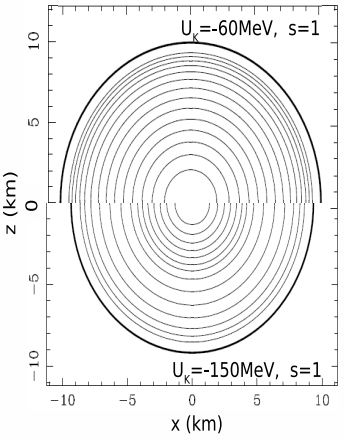

FIGURE 3.8: Energy density iso-contours of a rotating NS with baryon mass of $2M_{solar}$. Top(bottom) panel shows static NS with EoS for $U_{\bar{K}} = -60(-150)$ MeV,with $s = 1$.

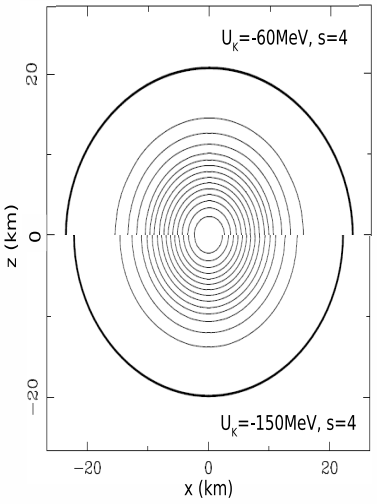

FIGURE 3.9: Energy density iso-contours of a rotating NS as in Fig 3.8, but with higher entropy per baryon state $s = 4$

.

of 1 and have same baryon mass of $2M_{solar}$. As we can see from the figure, a deeper potential tends to make the NS more compact. Further, in both the cases, the NS are nearly spherically symmetric with the ratio of polar to equatorial radius ~ 0.97. Fig. 3.9 gives contour plots for a NS with same EoSs (with shallower and deeper $U_{\bar{K}}$) as in the previous figure but with a higher s of 4. We notice that at higher s the NS becomes bulkier, its size being almost double to that of a star with an s of 1. We also notice a slight deviation from the spherical shape for higher s star with the ratio of polar to equatorial radius now ~ 0.7. Thus, we conclude that the shape of a NS depends on its EoS and thermodynamic state. A NS with lower s has a denser core and is more compact. Hence a higher s star which is less compact deforms more when subjected to rotation as it gets bulged in the equatorial plane and is flattened in the vertical direction, which incidentally is also the direction of the stellar angular momentum.

Next we study the effect of rotation on a particular NS configuration. Top slice of Fig. 3.10 shows a NS with npK matter at deeper potential and low s ($U_{\bar{K}} = -150$ MeV, $s = 1$. The NS is rotating slowly at 11 Hz and has an angular momentum J$\sim 0.02\ GM^2_{solar}/c$. NS shown in bottom slice rotates slightly faster at 280 Hz and has J$\sim 0.5\ GM^2_{solar}/c$. Fig. 3.11 has the same NS with J$\sim$1.8 (top slice) and 2.23 M^2_{solar}/c (bottom slice) and rotating with a frequency of 830 Hz and 930 Hz (Keplerian) respectively. The NS is fairly spherical at low angular momenta, but gets deformed at higher J. At Keplerian frequency, the NS becomes elongated in an effort to keep itself from falling apart. Thus the rigid rotation of a NS changes its shape as well as its equatorial radius. In the final contour plot of Fig. 3.12 we check the deformation of the star

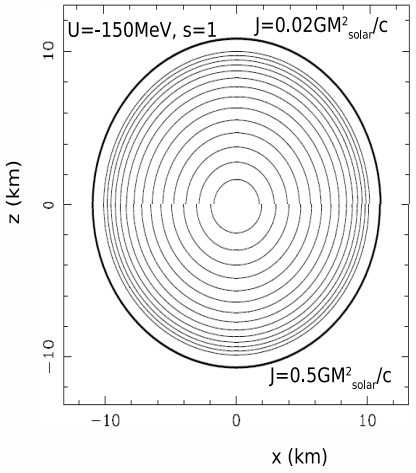

FIGURE 3.10: Effect of rotation on NS shape. Energy density iso-contours for a NS with npK ($U_{\bar{K}} = -150$MeV, $s = 1$) rotating at J=$0.02GM^2_{solar}/c$ (top panel) and $0.5GM^2_{solar}/c$ (lower panel).

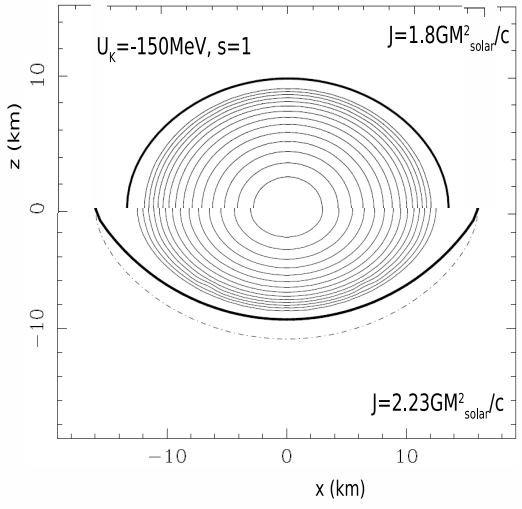

FIGURE 3.11: Energy density iso-contours for a NS as in Fig 3.10 rotating at J=$1.8GM^2_{solar}/c$ (top panel) and $2.23GM^2_{solar}/c$ (lower panel).

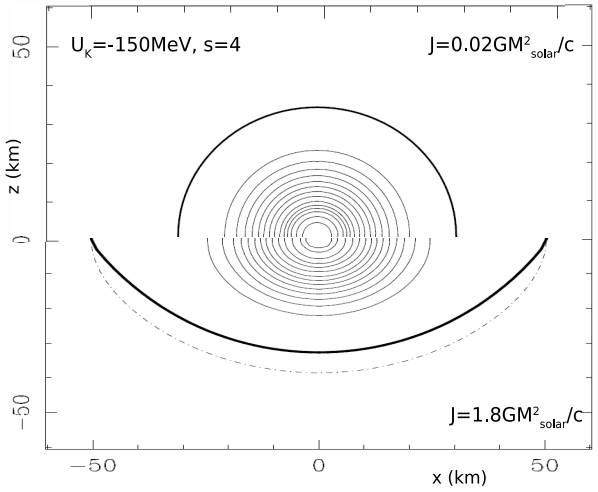

FIGURE 3.12: Fluid energy density iso-contours for NS ($U_{\bar{K}} = -150$ MeV, $s = 4$) rotating at J=$0.02GM^2_{solar}/c$ (top panel) and at J=$1.8GM^2_{solar}/c$ (lower panel)

with npK EoS at higher s of 4. We compare a slowly rotating star having $J = 0.02GM^2_{solar}/c$ with a fast rotating star having $J = 1.8GM^2_{solar}/c$. We observe the same pattern of deformation in shape at higher angular momentum as was noted for Figs. 3.10 and 3.11. However, the deviation from spherical symmetry is much more pronounced in this case. This can again be attributed to the lower density of the core for a higher s NS.

In a NS, the deviation from spherical symmetry due to the anisotropy of energy-momentum

tensor in the presence of strong magnetic fields has been reported by several authors. It has also been shown that the inclusion of magnetic field effects in the EoS and the interaction between the magnetic field and matter (or magnetisation) does not affect the stellar structure considerably [103, 104]. Without considering the magnetic field effects in our EoS, we made an order estimation for the GW emitted due to non-axisymmetric deformation or the ellipticity in a magnetized NS with baryon mass $2M_{solar}$.

We consider a typical NS with dipolar magnetic field that is uniform inside the star. For an estimation of GW amplitude, we assume that the magnetic and rotational axes are not aligned. Also, the star is assumed to be rotating at a frequency of 200 Hz which is much lower than its mass shedding limit, such that the deformation is primarily due to the strong magnetic field. Further, we assume that the magnetic energy is much less than the rotational kinetic energy as it is considered to be a realistic case. The NS then becomes a triaxial ellipsoid and emits GW as a result [105]. With this, a numerical estimate of the GW amplitude can be made using the following relation [105],

$$h_0 = 4.21 \times 10^{-24} \Big[\frac{ms}{P}\Big]^2 \Big[\frac{kpc}{D}\Big] \Big[\frac{I}{10^{38} kgm^2}\Big] \Big[\frac{\epsilon}{10^{-6}}\Big]. \tag{3.1}$$

Here, P is the rotation period of the NS, D is the distance to the NS, I is its moment of inertia with respect to its rotation axis and ϵ characterises the ellipticity of the NS due to magnetic field induced distortion. For a NS with polar magnetic field B_{pole}, the ellipticity is given by [105]

$$\epsilon = \frac{45}{64\pi} \frac{B_{pole}^2}{\mu_0 G \rho^2 R^2}. \tag{3.2}$$

To make an order of magnitude estimate, we consider a typical magnetar formed in a binary merger event that is at a distance of $D = 40Mpc$[35]. We assume that the NS has a polar magnetic field, $B = 10^{15}$ G. Using Eqs. 3.1 and 3.2 we then obtain a GW amplitude $h_0 \sim 9.3 \times 10^{-30}$ for a cold NS (T= 0 MeV). It increases marginally to 1.09×10^{-29} for hot NS with $s = 1$ and 4.18×10^{-27} for NS with $s = 4$. Since all the above calculations assume the same B, the difference in GW amplitude is due to the thermal effect on EoS only. The GW emission from such a NS occurs at frequencies of f and $2f$ (where f is the rotation frequency of the NS). The strength of the two components is determined by the angle α between the distortion axis (axis of magnetic field induced distortion) and the rotation axis of the NS. For small α, f is the dominant component and for large α, $2f$ component dominates [105]. For our case, the GWs from the distorted NS will be emitted at 200 Hz and 400 Hz, with the relative strength of each component being determined by the angle α.

3.3 Discussion and Conclusion

In the present chapter we studied the set of NS EoS that contain thermal kaons (K^T) and K^- condensates in its core. This is done within the framework of relativistic mean-field theoretical model with density dependent couplings. We also compare these EoS with nucleon-only EoS. All of these have been studied for a set of constant s NS. The finite s NS is then compared with NS at zero temperature.

The EoS with exotic matter tends to be softer as compared to np EoS. Moreover, among the npK EoS with antikaon condensates at different $U_{\bar{K}}$, the EoS with deeper potential makes K^- condensates appear at lower densities in the core than that for a shallower $U_{\bar{K}}$, thereby resulting in softer EoS for matter at deeper optical potential. In general, the npK EoS also appears to stiffen as the entropy per baryon of a NS core increases. Our static results are qualitatively consistent with earlier work of Pons et al. [102], where the EoS of kaon-condensed matter including the effects of temperature and trapped neutrinos were throughly studied [102]. The set of cold EoS we studied, however, fall within the required observational limit of 2 M_{solar} star unlike theirs.

We also studied the fraction of various particles in a NS core obeying a given EoS and noticed that the fraction of thermal kaons increases with an increase in s but decreases slightly with an increase in potential depth, whereas the fraction of antikaon condensates decreases with s but increases with an increase in the depth of antikaon optical potential.

We next studied the mass sequences for NS at constant total entropy S and found that the EoS behaviour is closely reflected in these mass sequences. It was observed that maximum mass of a NS sequence increases with an increase in S. In contrast, the maximum mass attained in a sequence decreases as the depth of optical potential increases. We next studied the evolution of the mass-number density relation with various angular momenta for different EoS. The maximum mass of a given sequence was found to increase with an increase in the corresponding angular momentum.

We also observed the fall of temperature from the core to the surface of a NS. The core and the surface temperature depend on the EoS and the thermodynamic state of matter or low s, the temperature in NS rises in the presence of antikaons. However, the temperature is more for np matter compared to npK matter for higher s NS. In the presence of other exotic fermions, such as hyperons, this trend was reported in earlier work [102] as well.

Further, we studied the effect of rotation on the equilibrium structure of a NS in the form of iso-contours of its fluid energy density. A NS obeying an exotic EoS with deeper potential tends to be more compact as compared to a NS with an EoS with shallow $U_{\bar{K}}$. In both the cases, we find that at low J, a NS tends to be nearly spherically symmetric but starts to deviate from

spherical symmetry as its J increases. The NS deforms considerably as its reaches the Keplerian limit. The deformation was found to be more for a higher s NS. Also, a higher s star has less dense core and thus bulges more in the equatorial plane when subjected to fast rotation along the polar axis.

Finally, we made a crude estimate of the GW amplitude for a highly magnetised NS whose magnetic axis is not aligned with its rotation axis. The GW amplitude for a hot NS with high s was found to be considerably larger than that for a cold NS. Still its strength is not large enough to come in the range of the present day detectors, but might just come within the grasp of next generation of GW observatories.

Chapter 4

Signatures of strangeness in differentially rotating NS-NS merger remnants

4.1 Introduction

The merger of binary NS leaves a hot, massive and differentially rotating NS. A differentially rotating star can have a rapidly rotating core without attaining the mass-shedding limit on the surface. Thus it can sustain an angular momentum, much larger than that supported by uniformly rotating stars. The large angular momentum on the other hand supports a significantly higher mass against gravitational collapse. If two component NSs have masses $\sim$ 1.3–1.5 times the maximum mass of nonrotating stars (M_{TOV}), the binary-merger configuration is known as hyper-massive neutron star (HMNS). The detection of GWs from GW170817 and the delayed emission of gamma-ray after $\simeq 1.74s$ provide the best confirmation towards a HMNS remnant, that ultimately collapses to a black hole surrounded by a magnetized accretion disk.

Recently Weih et al. [45] and Bozzola et al. [106] have performed stability analysis of differentially rotating relativistic stars against prompt gravitational collapse to a black hole. They study the secular instability in HMNS and proposed a "quasi-universal" relation between the maximum mass of the remnant and its scaled angular momentum independent of the EoS. The EoSs considered for the sequences of differentially rotating equilibrium models using the j-constant law, were polytropes, zero-temperature hadronic EoSs or strange star EoSs. Several recent investigations have also probed the threshold mass beyond which the merger remnant collapses to a black hole and the collapse time. However, their estimates and methodology vary widely [48, 107, 108, 109]. Further, many of the assumptions that go into such calculations (e.g.

slow rotation, spin down via electromagnetic radiation only, consistent treatment of thermal contribution in the EoS) must be carefully reconsidered.

In the case of differential rotation with the j-constant law, solutions for a given maximum energy density can be classified into four different types (A-D) depending on the degree of differential rotation[44]. The A types consist of spheroidal configurations with a relatively low degree of differential rotation. These sequences start at a static and spherical body and always end at a mass shedding limit. Type B sequences start at the mass shedding limit and have a continuous parametric transition to a regime of bodies with toroidal topology. Sequences of type C start at a static and spherical body and possess a transition to arbitrarily thin rings. Finally, sequences of type D exist only in a narrow range of differential rotation parameter, and are typically highly pinched at the equator and quasi-toroidal [106]. In this work, we investigate the role of strangeness in the NS core on the stability of the hyper-massive NS merger remnant. We consider only the most realistic solutions of differentially rotating stars that belong to the class "A" [44]. The signature of the presence of strangeness containing matter such hyperons and antikaon condensates, on the secular instability is investigated, as well as the universality of the proposed relations. We consider differential rotation and include thermal effects, which are crucial properties of a NS merger remnant. We also estimate the threshold mass of the merger remnant for prompt collapse to a black hole and the corresponding collapse time.

4.2 Numerical scheme

Differential rotation may support hot HMNS merger remnants against collapse. In order to study the stability of the merger remnants, one must obtain equilibrium NS configurations for the EoSs discussed in (Sec. 2.2.2). There are already existing numerical schemes that compute equilibrium solutions of uniform and differentially rotating cold NSs, see e.g. the numerical library LORENE [60]. Within this scheme, calculations are performed solving general relativistic equations of hydrostatic equilibrium of rotating, axially symmetric stars. The first attempts towards equilibrium models including thermal effects in uniformly and differentially rotating NSs were introduced by Goussard et al. [21, 59] for realistic EoSs. It was shown that for finite temperature, the integrability of the equation of stationary motion requires an isentropic (constant entropy) or isothermal (constant temperature) solution. Rapidly (uniformly) rotating hot NS configurations were also computed within this framework in [67] for realistic EoSs including hyperons.

In this study we compute equilibrium solutions of hot (isentropic) differentially rotating NSs within the same numerical scheme. Equilibrium equations are solved with Einstein equations, with the assumptions of stationarity, axisymmetry and circularity (absence of meridional convective currents). An EoS is required to close the system of equations. For finite temperature, the EoS

depends on temperature as well as on the particle number densities. The partial differential Einstein equations are solved using a multidomain spectral method [60].

In order to investigate the role of differential rotation, we employ the usual KEH [110] or j-constant rotation law defined by the velocity profile:

$$F(\Omega) = R_0^2 \, (\Omega_c - \Omega)$$

where Ω_c is the central angular frequency and R_0 is a free parameter with dimensions of length that determines the degree of differential rotation [41]. We consider the dimensionless parameter $a = R_e/R_0$, where R_e is the equatorial NS radius. Thus the limit of uniform rotation is obtained when $a \to 0$ and increasing a denotes increasing degree of differential rotation. The advantage of the j-constant law is that it approximately reproduces the rotation-profile obtained in 2D-simulations, and is a "simple" law, with the minimum number of free parameters. Although the j-constant rotation law is the most widely used, alternative rotation laws have been discussed in the literature [106] and should be investigated. However, such a task is beyond the scope of this work, and we leave it for a future study. It should be noted that the previously obtained stationary state equilibrium solutions for hot differentially rotating (proto-)NSs were also investigated by Goussard et al. [59] using the j-constant rotation law.

4.3 Results

We consider the following different compositions for the NS core:
(i) pure nucleonic matter (np)
(ii) matter with Λ-hyperons (np$\Lambda\phi$)
(iii) matter with antikaon condensates (npK).
Newly born protoneutron stars at finite temperature as well as hot merger remnants have been studied elaborately in the literature [35]. One may consider either isothermal or isentropic configurations. Isentropic configurations are quantified by the value of entropy per baryon s. We take $k_B = 1$. We have seen for a fixed entropy per baryon of $s = 2$, a NS can shoot a central temperature of 50-100 MeV [111]. Therefore, it is important to study the role of thermal effects on the stability of the NS. In this study, therefore, we compare two cases:
(i) Zero temperature ($s = 0$) EoSs
(ii) The same EoSs with thermal effects included ($s = 2$).

The above EoSs (discussed in Sec. 2.2.2) and the corresponding mass-density relations for the non-rotating as well as the mass-shedding cases are shown in Fig. 4.1. In the left panel pressure P (in $MeVfm^{-3}$) is plotted against the baryon number density n_B (in fm^{-3}). The np EoS is the stiffest of the three, which softens with the advent of extra degrees of freedom in the form of

strange particles, K^- condensates and Λ-hyperons. Again, the EoSs are stiffer for stars with finite entropy per baryon compared to the cold ones for all the three cases, the difference arising from the thermal contribution to the pressure. We use solid lines for T=0 and dashed ones for stars at $s = 2$.

Solving the TOV (Tolman Oppenheimer Volkov) equations of relativistic hydrostatic equilibrium, we obtain the macroscopic structure properties (mass and radius) of the NS. The solutions for the static star corresponding to the different EoSs are plotted in the lower right panel of Fig. 4.1. As expected, strange EoS yields a lower maximum mass star compared to that of np EoS. A stiffer EoS can support larger mass. However, all the sets of EoS yield maximum mass above the observational $2M_{solar}$ limit [7, 8].

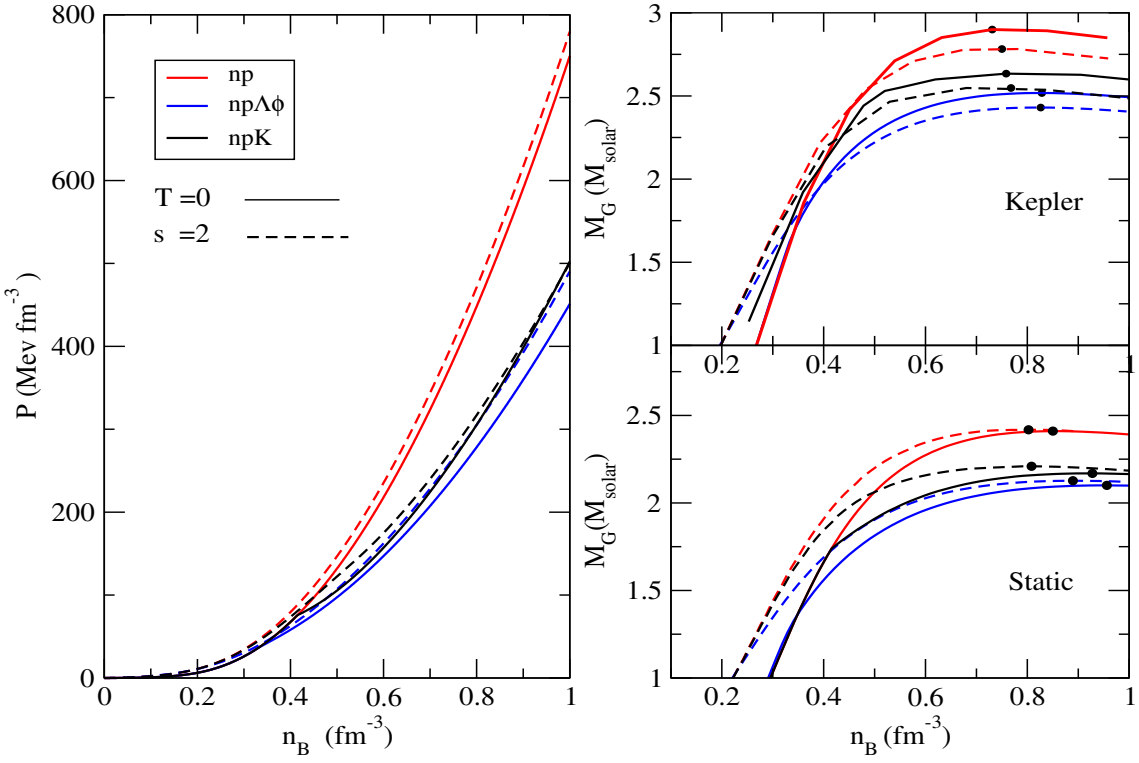

FIGURE 4.1: EoSs (left panel) and corresponding gravitational mass -baryon density sequences (static & uniformly rotating Kepler) are plotted in the right panel. solid lines are used for cold star (T=0), while dashed lines are used for finite entropy per baryon $s = 2$.

Let us follow a NS with similar compositions. Between a cold ($T = 0$) and hot ($s = 2$) EoS, the latter being stiffer can support a static star of larger mass, compared to its cold counterpart. However, this trend is reversed for the mass-shedding sequences. We plot the mass of sequences of uniformly rotating stars at the Keplerian limit in the upper right panel of Fig. 4.1. The maximum masses for the Keplerian sequences increase by ∼20-23% more than their static ones for the cold stars, whereas for the stars with $s = 2$ the differences are ∼12-15%. The values of maximum mass and other relevant properties are given in Table 4.1. The thermal pressure contribution can sustain a heavier NS. But it is evident from the table that the Keplerian

frequency for a hot NS is not as high as that of the cold star. Hence the difference in maximum mass is lower for hotter stars.

4.3.1 Onset of secular instability

The onset of the secular instability is determined by the "Turning point" (TP) criterion i.e. the maximum of the gravitational masses as a function of central density [43]. The TP criterion for secular stability in hot rigidly rotating stars was obtained in [59, 67] for isentropic (or isothermal) solutions. Considering sequences of differentially rotating equilibrium models using the j-constant law, it was shown that a stability criterion for differentially rotating neutron stars exists similar to the one of their uniformly rotating counterparts [45, 106]. The onset of dynamical instability for differentially rotating stars is marked by the neutral-stability line (where the eigenfrequency of the fundamental mode of oscillation vanishes). The neutral-stability and TP curves coincide for nonrotating neutron stars, but their difference grows with increasing angular momentum. Along a sequence of constant angular momentum, dynamical instability sets in for central rest-mass densities slightly lower than that of secular instability at the TP.

In order to investigate the effect of the NS core composition on the stability of the NS merger remnant, one must construct relativistic equilibrium sequences and calculate the extra mass supported by the rotating star compared to the static star for the EoSs considered. However it has already been shown that sequences at constant rotation frequency do not allow one to distinguish between stable and unstable solutions [67], but rather sequences of constant angular momentum must be compared. We therefore generate equilibrium sequences at constant angular momentum for given degree of differential rotation a.

In Fig. 4.2, we display gravitational mass M_G (in solar masses) as a function of central energy density ρ_c (in units of $\rho_{nuc}c^2$, where $\rho_{nuc} = 1.66 \times 10^{17} kg/m^3$) for the nucleonic np EoS. The nonrotating limit are denoted by the red "static" curves while mass-shedding limit by black "kepler" curves for uniformly rotating NSs. Also plotted (in colour) are constant angular momentum sequences (labeled by their angular momentum values "J") for a given degree of differential rotation ($a = 0.2$). In order to study the thermal effects, different values of entropy are considered, $T = 0$ in the left panel and $s = 2$ in the right panel.

In Fig 4.3, we show the static and mass-shedding limit for uniformly rotating equilibrium sequences for np$\Lambda\phi$ EoS. Constant angular momentum sequences for differential rotation parameter $a = 0.2$ are also included in between the static and Kepler sequences. The left panel displays the zero temperature case while the right panel includes thermal effects ($s = 2$). As before, the different parameters are summarized in Table 4.2.

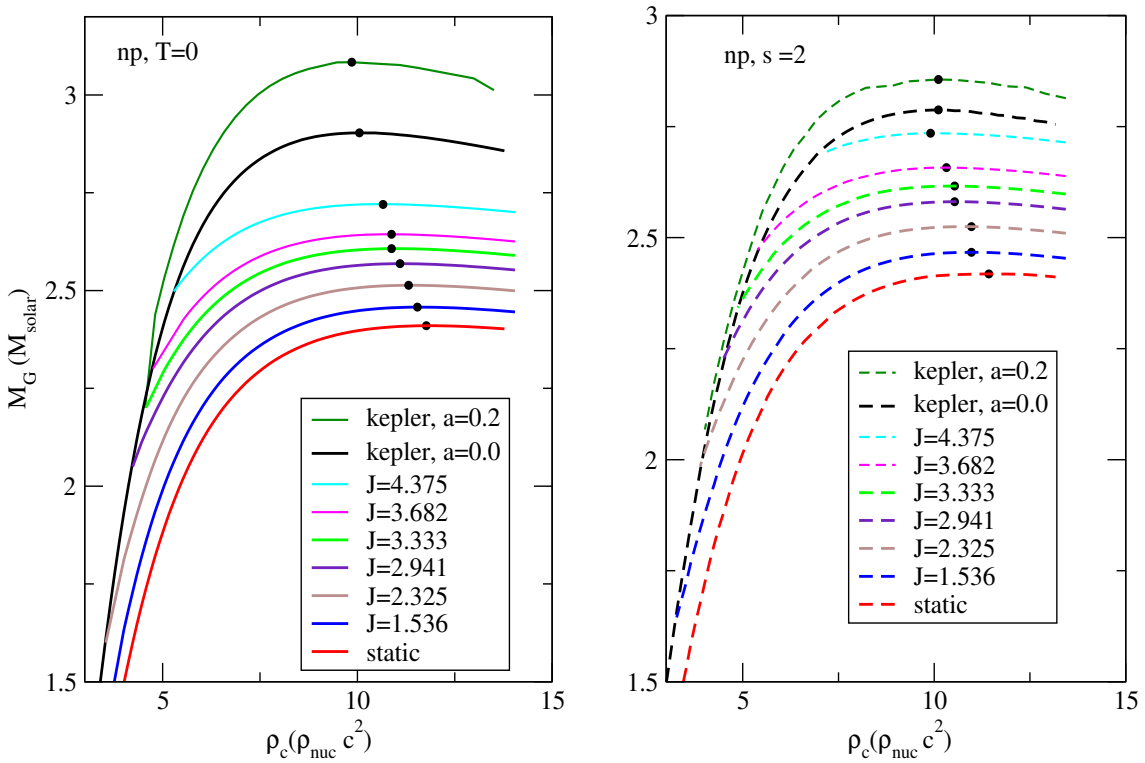

FIGURE 4.2: Equilibrium sequences for nucleonic EoS for nonrotating (red "static" curve) and mass-shedding or "kepler" limits of uniformly rotating NSs (black curve) and differentially rotating NSs at degree of differential rotation $a = 0.2$ (dark-green curve). Also plotted (in colour) are constant angular momentum sequences (labeled by their "J" values) for $a = 0.2$. Left panel is for $T = 0$, right panel is for entropy per baryon $s = 2$. The black dots denote the turning points.

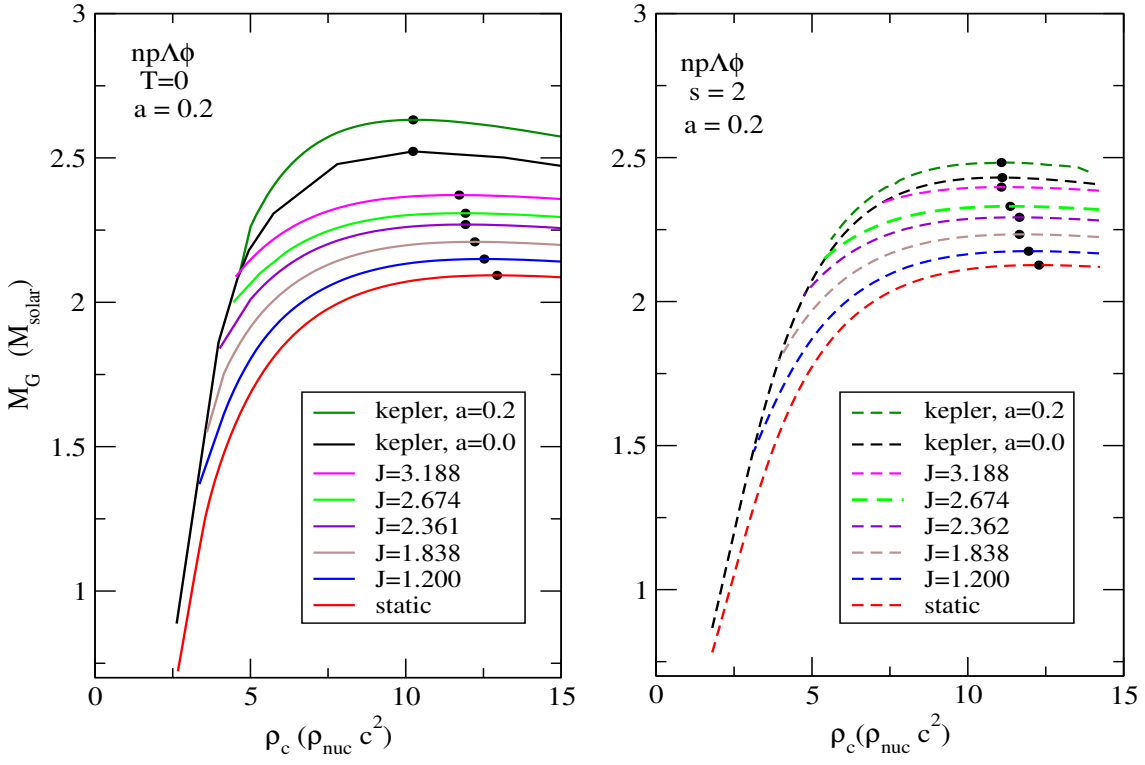

FIGURE 4.3: Same as Fig 4.2, but for npΛϕ EoS

In Tables 4.1, 4.2 and 4.3, we study the TP criterion, considering np, npΛϕ and npK EoSs for $s = 0$ and $s = 2$ respectively. The columns represent respectively the angular momentum J (in GM^2_{solar}/c), central energy density ρ_c (in $\rho_{nuc}c^2$), gravitational mass M_G (in M_{solar}), central frequency f_c in Hz, ratio of polar and equatorial radii R_p/R_e, ratio of central and equatorial angular frequencies Ω_c/Ω_e, circumferential radius R_{circ} (in km) and the ratio of kinetic to gravitational energy T/W. The upper panels of the tables are for differential rotation with $a = 0.2$, which have been arranged in ascending order of J, the top row denoting the maximally rotating ones. For comparison we added data for a static star and a star rotating uniformly at Keplerian frequency at the bottom panels of the tables. One can observe the increase of M_G as the star starts rotating from zero to higher J values. It can accommodate more mass when it rotates differentially, also the central frequency of rotation and the ratio of T/W increase. However, faster the star, more is the deformation as is evident from the ratio R_p/R_e i.e. the star becomes oblate and flattened. This trend is same for all Tables 4.1, 4.2 and 4.3. Due to strangeness degree of freedom, the maximum mass goes down for static and mass-shedding limits, as we have seen in Fig. 4.1. The mass for differential rotation with $a = 0.2$ also reduces accordingly in the presence of Λ hyperons and K^- condensates.

Also, we have put the values in the parenthesis for finite entropy density stars i.e. s=2. We already discussed at the beginning of the Results section that thermal pressure can be crucial to support a larger mass in case of static stars. However, the frequency of the hot star is comparatively less than the cold ones. Hence the stars rotating at its mass-shedding limits may not be as massive as the colder counterparts. Hence the hotter stars are less deformed.

[np, $T = 0$ ($s = 2$)]						
J	ρ_c	M_G	f_c	R_p/R_e	R_{circ}	T/W
7.36(5.39)	9.86(10.11)	3.08(2.86)	1820.78(1532.18)	0.48(0.60)	16.51(16.12)	0.167(0.119)
4.38	10.66(9.91)	2.72(2.74)	1510.12(1387.25)	0.74(0.70)	13.39(14.97)	0.095(0.093)
3.68	10.88(10.32)	2.64(2.66)	1367.54(1272.82)	0.79(0.76)	12.29(14.30)	0.075(0.074)
3.33	10.88(10.53)	2.61(2.62)	1278.70(1191.50)	0.82(0.80)	12.85(13.99)	0.065(0.063)
2.94	11.09(10.53)	2.57(2.58)	1176.64(1101.74)	0.85(0.82)	12.64(13.79)	0.054(0.053)
2.33	11.32(10.75)	2.51(2.53)	983.05(925.88)	0.89(0.88)	12.37(13.42)	0.036(0.036)
1.54	11.77(10.97)	2.46(2.47)	693.18(652.35)	0.95(0.94)	12.0(13.07)	0.017(0.017)
5.91(4.82)	10.05(10.11)	2.90(2.79)	1537.86(1354.41)	0.68(0.58)	13.74(16.92)	0.13(0.10)
0(0)	11.77(11.43)	2.41(2.42)	0(0)	1(1)	11.86(12.72)	0(0)

TABLE 4.1: TP criterion for stars rotating differentially (a=0.2) for zero temperature np EoS. The values in parenthesis are for $s = 2$. Among them, the topmost row is for stars spinning at Kepler frequency. The last two rows are for uniformly rotating star at Keplerian frequency and for static star respectively.

[npΛϕ, $T = 0$ ($s = 2$)]						
J	ρ_c	M_G	f_c	R_p/R_e	R_{circ}	T/W
5.02(3.82)	10.24(11.08)	2.63(2.48)	1583.14(1297.45)	0.51(0.54)	16.67(17.48)	0.143(0.103)
3.19	11.72(11.08)	2.38(2.40)	1395.82(1303.96)	0.73(0.69)	13.29(14.95)	0.087(0.832)
2.67	11.92(11.36)	2.31(2.33)	1272.70(1192.95)	0.79(0.76)	12.85(14.21)	0.069(0.066)
2.36	11.63(11.66)	2.27(2.29)	1174.38(1111.55)	0.82(0.80)	12.63(13.81)	0.057(0.055)
1.84	12.22(11.66)	2.21(2.23)	988.34(927.662)	0.88(0.86)	12.26(13.37)	0.039(0.037)
1.20	12.53(11.95)	2.15(2.18)	698.29(656.40)	0.94(0.93)	11.89(12.91)	0.019(0.017)
4.28(3.44)	10.24(11.10)	2.52(2.43)	1413.10(1277.04)	0.56(0.58)	15.93(16.88)	0.122(0.091)
0(0)	12.84(12.26)	2.10(2.13)	0(0)	1(1)	11.52(12.5)	0(0)

TABLE 4.2: TP criterion for zero temperature npΛϕ EoS. The values in parenthesis are for $s = 2$.

[npK, $T = 0$ ($s = 2$)]						
J	ρ_c	M_G	f_c	R_p/R_e	R_{circ}	T/W
5.54(4.33)	9.65(9.59)	2.74(2.61)	1586.44(1356.46)	0.50(0.54)	16.94(18.15)	0.149 (0.109)
3.02	11.41(9.86)	2.40(2.44)	1307.14(1140.28)	0.77(0.75)	13.09(14.94)	0.075(0.07)
2.89	11.41(10.13)	2.39(2.42)	1273.24(1122.21)	0.79(0.77)	13.00(14.76)	0.070(0.066)
1.71	11.96(10.41)	2.26(2.30)	882.16(773.57)	0.90(0.90)	12.23(13.75)	0.031(0.029)
1.13	11.94(10.98)	2.21(2.25)	620.09(550.58)	0.95(0.95)	11.94(13.31)	0.015(0.014)
4.65(3.84)	10.13(9.60)	2.62(2.55)	1429.12(1210.26)	0.56(0.58)	16.08(17.79)	0.126(0.095)
0(0)	12.53(10.98)	2.17(2.21)	0(0)	1(1)	11.69(13.07)	0(0)

TABLE 4.3: TP criterion for zero temperature npK EoS. The values in parenthesis are for $s = 2$.

4.3.2 Universal Relations

In this work, we investigate whether the presence of strangeness affects the universality of the relations proposed recently [45, 106]. In Fig 4.4, the maximum or TP masses of differentially rotating sequences $M_{max,dr}$ for a given degree of differential rotation ($a = 0.2$) normalized to the corresponding TOV mass M_{TOV} is plotted as a function of normalized dimensionless angular momentum $j/j_{max,0}$ for the different EoSs discussed in Sec. 2.2. Here $j = J/M^2$ while $j_{max,0}$ is the maximum value of j at the mass-shedding limit for a uniformly rotating NS. It is evident from the figure that thermal effects spoil the universality of the relations. This is interesting because the hyper-massive NS merger remnant is hot (temperature ~ 80 MeV) and hence thermal effects cannot be ignored. However we find that the behaviour of the cold and hot EoSs individually do not vary qualitatively. In both cases, for differential rotation $a = 0.2$, the curves are independent of the different EoSs considered in this work. So we fit the curves for the cold and hot EoSs with a simple polynomial function of the form

$$\frac{M_{max,dr}}{M_{TOV}} = 1 + b_1(a)(\frac{j}{j_{max}})^2 + b_2(a)(\frac{j}{j_{max}})^4 \tag{4.1}$$

where the coefficients are found to be $b_1 = 0.30735(0.1964)$ and $b_2 = -0.10671(-0.04671)$ for cold(hot) stars respectively for differential rotation parameter a=0.2. For comparison with

previous works [45], in Fig. 4.5 we show the maximum masses of differentially rotating sequences $M_{max,dr}$ for differential rotation $a = 0.2$, but this time as a function of the normalized dimensional angular momentum $j/j_{max,a}$ for the mass-shedding limit of differentially rotating stars. It is obvious that in this case, the maximum masses at $j = j_{max,a}$ are higher, but the spread of the curves for different EoSs is also larger.

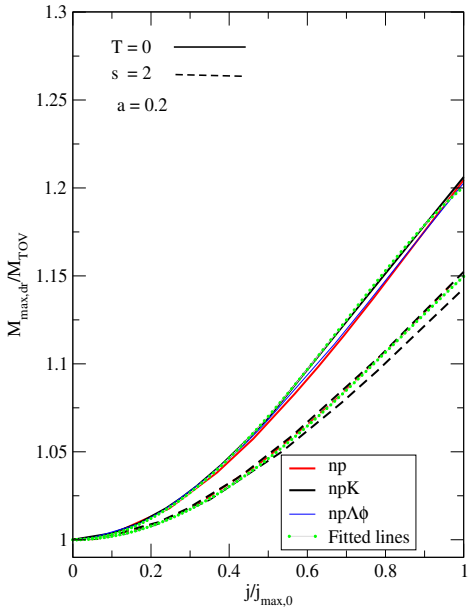

FIGURE 4.4: Maximum or TP mass normalized to TOV mass of differentially rotating sequences for a degree of differential rotation ($a = 0.2$) as a function of normalized dimensionless angular momentum for different EoSs.

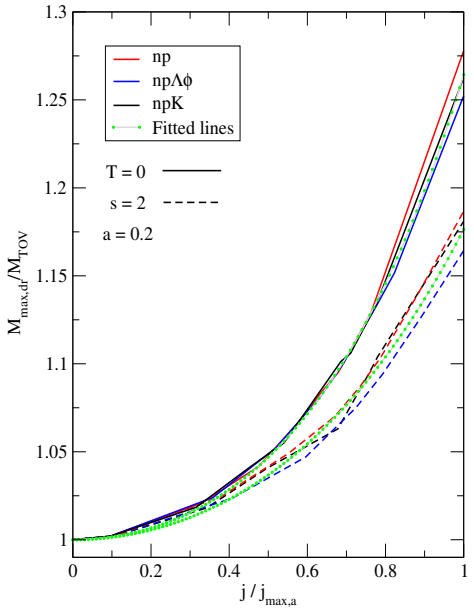

FIGURE 4.5: Maximum or TP mass normalized to TOV mass of differentially rotating sequences ($a = 0.2$) as in Fig. 4.4, angular momentum is however, normalized by the corresponding differential rotation value for different EoSs.

We have just established that irrespective of the EoS, there are two families of curves of hot ($s = 2$) and cold ($T = 0$) stars for a differentially rotating star with a=0.2. We now investigate whether this holds true for other values of differential rotation a. In Fig 4.6, the maximum or TP masses normalized to the corresponding TOV mass of differentially rotating sequences for different degrees of differential rotation a are plotted as a function of normalized dimensionless angular momentum $j/j_{max,0}$ with one representative EoS (np) for the two families $T = 0$ and $s = 2$. We find that curves in the two families coincide for all the values of a considered ($0 < a < 1$). This also holds true for the other EoSs considered in this study (npΛϕ and npK). Therefore the fit relation proposed in Eq. 4.1 also holds true for other values of a independent of the EoSs considered in this work.

In order to determine the absolute maximum mass of a hot or a cold differentially rotating star, one needs to compute equilibrium configurations with increasing j until the mass-shedding limit for each a is reached. Now if the fit relation of $j_{max,a}/j_{max,0}$ with a is known (see Fig. 4.7), then one may determine the absolute maximum mass using the universal fit function Eq. 4.1.

However, it is numerically very challenging to generate Kepler sequences for large values of differential rotation. In Fig. 4.7, we could obtain mass-shedding configurations up to differential rotation $a = 0.3$ for both hot and cold stars, but for higher a the uncertainties are large. For the equilibrium configurations we could obtain (see Fig. 4.6), the maximum mass obtained was M_{max}/M_{TOV}= 1.23 (1.19) for the cold (hot) star. The value corresponding to the cold star is lower than the value 1.54 ± 0.05 obtained by Weih et al. [45] and comparable to the value 1.2 of Bozzola et al. [106].

4.3.3 Collapse time of the merger remnant

The value of the total progenitor mass of the NS binary in GW170817 is derived to be 2.74 M_{solar}. The mass of the remnant of the BNS merger has been estimated to be $\sim$ 2.7-2.8 M_{solar}. There are various possible outcomes of a NS merger that have been conjectured [112]:
(i) a uniformly rotating stable NS (if the progenitor mass $M_P \leq M_{TOV}$). If the EoS is stiff enough, this scenario could be possible [113].
(ii) a uniformly rotating supramassive NS (if $M_P > M_{TOV}$). In this case the remnant survives collapse as long as there is enough centrifugal support from rotation.
(iii) a hot differentially rotating hyper-massive NS (if M_P is greater than the maximum mass supported by uniform rotation).

A dynamically unstable HMNS remnant may be supported against collapse by the strong differential rotation and thermal pressure. If the remnant is strongly magnetized (protomagnetars with $B \sim 10^{15}G$), differential rotation is damped on the Alfven timescale ($\gtrsim$ 100 ms). Subsequent dissipation of the differential rotation and thermal energy by neutrinos (on the neutrino cooling timescale $\sim$ s) may result in a collapse of the HMNS merger remnant to a black hole on a timescale $\simeq$ 1 s, depending on the total mass, mass ratio and EoS of the NS binary. This may correspond to the 1.74s delay between the merger chirp signal and GRB170817A. The collapse time of the remnant has important implications on multi-messenger astronomy (electromagnetic, GW or neutrino signal). The observation of the blue kilonova and *La*-rich ejecta associated with GW170817 may indicate the formation of HMNS [114]. In the future GW observations from the post-merger remnant with the third generation of interferometers (LIGO India, Kagra, Einstein Telescope) might help to constrain the EoS of merger remnants.

Numerical simulations indicate that the HMNS is formed after the merger with a rapidly rotating highly non-axisymmetric bar-like structure [107]. This should result in a time-varying quadrupole moment, with strong emission of GW dominating the spindown. Once the differential rotation is damped, the HMNS may become a supramassive NS configuration, with a spindown dominated by magnetic braking. If the merger remnant is a supramassive NS, the large rotational energy

released in the isotropic MHD wind produce a large spin down luminosity $L_{SD} > 10^{42}$ erg s^{-1}. But the observed bolometric luminosity is lower than 10^{42} erg s^{-1} and no afterglow emission has been seen. Hence the possibility of a supramassive NS remnant may be ruled out. Thus the only possibility to be considered would be that of a hyper-massive NS merger remnant.

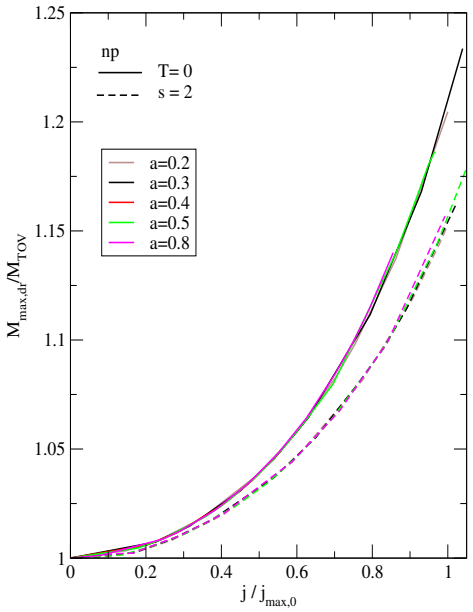

FIGURE 4.6: Maximum or TP mass normalized to TOV mass of differentially rotating sequences for the np EoS for different degrees of differential rotation a as a function of normalized dimensionless angular momentum of uniformly rotating stars.

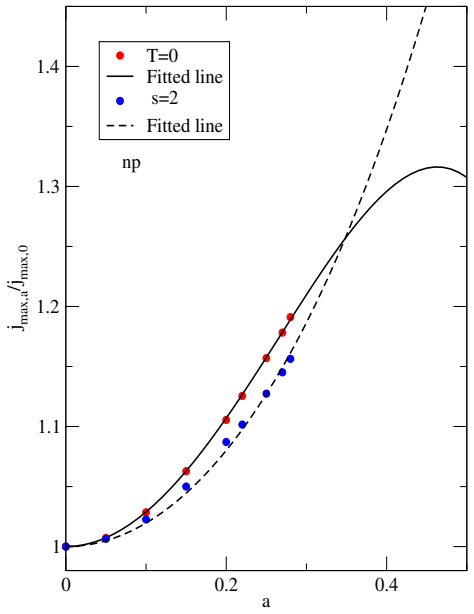

FIGURE 4.7: Ratio of normalized angular momenta for differentially rotating stars to uniformly rotating stars as a function of differential rotation a for the np EoS for hot stars (red circles) and cold stars (blue circles). The fit to these curves is also shown.

As we are interested in the stability of the HMNS merger remnant, we would like to make an estimate of the collapse time for the EoSs investigated in this work. However, the collapse time estimates and calculations that exist in the literature vary widely in their formalism and predictions and are far from reaching a consensus [48, 107, 108, 109]. We follow some of the recent suggested methods to obtain estimates of the collapse time and the threshold mass for prompt collapse for the EoSs considered in this work.

Assuming slow rotation and spindown of a possible SupraMassive NS (SMNS) merger remnant via electromagnetic radiation, [112, 115] analytically obtained estimates for collapse time using observations of SGRBS (short γ-ray bursts) by *Swift* telescope. However as observational evidence [107] now points to the fact that the remnant of the merger GW170817 may be a rapidly differentially rotating HMNS spinning down via gravitational radiation rather than a SMNS, the validity of such relations become questionable.

In the recent work of Köppel et al. [108], collapse times were computed using hydrodynamical simulations for five zero-temperature EoSs, adding a "thermal contribution" via an ideal-fluid

EoS [116]. But this approach of "hybrid EoS" is known to be non self-consistent. Among the EoSs considered were np and npΛϕ, which we have also been employed in this investigation for both zero temperature ($s = 0$) and finite temperature ($s = 2$). The calculation of threshold mass M_{th} above which the merger remnant promptly collapses to form a black hole was also explored in this work. Extending a previously proposed linear EoS-independent universal relation [117, 118]

$$M_{th}/M_{TOV} = 3.38\, C_{TOV} + 2.43$$

where the compactness $C_{TOV} = M_{TOV}/R_{TOV}$, they suggested the following non-linear fit formula

$$M_{th} = a - \frac{b}{1 - c\, C_{TOV}}$$

where $b = 1.01$, $c = 1.34$ and $a = \frac{2b}{2-c}$, taking into account the expected black hole limit $M_{th}/M_{TOV} \to 0$ for $C_{TOV} \to 1/2$.

Recently, the results from simulations (see e.g. [108]) and observations (e.g. [112, 115]) were combined to derive a radius-independent fit relation between the initial mass of the single NSs M_{NS} and the collapse time t_{coll} [48] :

$$\log(t_{coll}) = e_0 + e_1 \log\left(\frac{M_{NS}}{M_{TOV}}\right) \ , \tag{4.2}$$

where $e_0 = -5.45 \pm 0.40$ and $e_1 = -38.9 \pm 1.7$. The robustness of such a relation was tested and proposed as a useful tool to constrain NS EoSs [48]. npΛϕ ($s = 0$) EoS was also one of the EoSs considered.

In order to compare with the results discussed above, we consider the same values of initial data as in [108] namely initial masses M_{NS}=1.53, 1.55 and 1.57 M_{solar} for the np EoS and 1.62,1.63 and 1.65 M_{solar} for $np\Lambda\phi$ EoS. Using the formula for M_{th} suggested in [108], we calculated the threshold mass for prompt collapse in units of M_{TOV}. The results for $s = 0$ as well as $s = 2$ case are summarized in Table 4.4. For comparison with previous works, we also provide the maximum static mass M_{TOV}, corresponding radius R_{TOV}, compactness C_{TOV} and the free-fall timescale

$$\tau_{TOV} = \frac{\pi}{2}\sqrt{\frac{R_{TOV}^3}{2M_{TOV}}} \ . \tag{4.3}$$

We then apply Eq.(4.2) to calculate collapse times t_{coll} for comparison with the results of [48]. The estimated values of t_{coll} (taking only the mean values for the fit coefficients e_0 and e_1) corresponding to the different M_{NS} are provided in the Table 4.4.

TABLE 4.4: The maximum static mass, corresponding radius, compactness, free-fall timescale, threshold mass for prompt collapse and collapse time for each EoS.

EoS	M_{NS} (M_{solar})	s (k_B)	M_{TOV} (M_{solar})	R_{TOV} (km)	C_{TOV}	t_{coll} (ms)	τ_{TOV} (μs)	M_{th} (M_{TOV})
np	1.62	0	2.41	11.86	0.30	18.2	80.2	1.37
	1.63					14.29		
	1.65					8.89		
np	1.62	2	2.418	12.72	0.28	20.72	88.9	1.44
	1.63					16.31		
	1.65					10.15		
$np\Lambda\phi$	1.53	0	2.10	11.52	0.27	0.79	82.26	1.48
	1.55					0.48		
	1.57					0.29		
$np\Lambda\phi$	1.53	2	2.127	12.5	0.25	1.31	92.36	1.54
	1.55					0.79		
	1.57					0.48		

4.4 Discussions

Since the detection of GWs from the NS binary merger event GW170817, the fate of the binary remnant remains a mystery. As no evidence of a remnant has yet been found from post-merger searches by the LIGO-VIRGO collaboration, one may study the different possibilities theoretically. One likely outcome of the merger is a metastable differentially rotating hot hyper-massive neutron star. As the stability (dynamical and secular) and time of subsequent collapse of the remnant depend on its rotation profile and its interior composition, it opens the possibility to constrain the dense matter EoS from its stability analysis.

In this chapter, we explored the onset of secular instability for different EoSs with and without strangeness. Using the Turning Point (TP) criterion, we investigated the maximum mass that may be supported by differential rotation and thermal effects for the different EoSs considered. We found that inclusion of thermal effects reduced the maximum mass of the differentially rotating configurations. This is interesting as the hyper-massive remnant is conjectured to be hot, and hence thermal effects cannot be neglected.

When studying the maximum mass supported by a hyper-massive NS remnant, previous works considered cold stars or a very restricted sets of EoS, e.g. polytropic EoSs or only nucleonic matter. With realistic EoSs including hyperonic and kaonic degrees of freedom we investigated the influence of these new degrees of freedom on the maximum supported mass. We found that the maximum mass obtained depends both on the EoS and the degree of differential rotation. In order to calculate the highest possible value of the maximum mass, we followed the method for obtaining a "universal relation" proposed by [40] for uniform rotation, extended for the case of differential rotation by [45, 106]. However for the EoSs considered, we found the universal relation to be practically independent of the EoS and the degree of differential rotation. The

highest mass obtained in our analysis was $M_{max} = 1.23 M_{TOV}$ for cold NSs and 1.19 M_{TOV} for hot NSs.

We further investigated the effect of strangeness on the collapse time of the merger remnant. We considered the scenario in which the hyper-massive NS merger remnant rapidly loses angular momentum due to loss of energy by GW emission and collapses to a black hole before the Alfven timescale, i.e. before the differential rotation is damped by magnetic dissipation. This scenario is currently favoured by the combined multi-messenger astrophysical observations [107]. We estimated the collapse time and threshold mass for prompt collapse for the EoSs with and without strangeness, using recently proposed fit formulas [48, 108] obtained using observations of short gamma ray bursts [115] and hydrodynamical simulations [108].

Post-merger MM searches may be able to answer the question about the fate of the merger remnant in GW170817, by ruling out some of the proposed scenarios. Future GW events from other NS mergers along with MM observations will provide further information about the stability of NS merger remnants as well as the dense matter EoS. An exciting journey in MM astronomy has only begun.

Chapter 5

Summary and Conclusion

In our work, we studied properties of hot rotating NS and compared them to cold rotating NS. We estimated the properties of NS rotating rigidly ($\Omega = const$) and differentially. To compute and compare the equilibrium configurations of rotating NS with DD2 EoS, we use NROTSTAR and ROTSTAR codes of the numerical relativity software library called LORENE, which implements the multi-domain spectral method for calculating accurate models of rotating NS in full general relativity.

DD2 EoS is developed within the framework of relativistic mean field model, in this model baryon-baryon interaction is mediated by exchange of σ, ω, and ρ mesons. The model also includes hyperon-hyperon interaction through ϕ mesons. Leptons are treated as non-interacting particles. Antikaon-baryon interaction has been studied in similar fashion as baryon-baryon interaction. Finite entropy EoS is constructed by solving equations of motion for the interacting mesons numerically along with the charge neutrality and baryon number conservation constraints. In this model, the meson-nucleon couplings are density dependent and they are adjusted to reproduce properties of symmetric and asymmetric nuclear matter and finite nuclei such as nuclear compressibility, symmetry energy and binding energy at saturation density.

In chapter 3 We studied the rotating NS sequences with DD2 EoS containing antikaon particles. We have generated a number of DD2 EoS profiles with neutrons, protons, leptons(np) and K^- condensates(npK) as constituent particles for different values of specific entropy. We plotted pressure vs baryon density curves for those EoS sets. We observed that np EoS with higher entropy has higher pressure at particular baryon density than np EoS with lower entropy, npK EoS followed the same trend. NS gravitational mass (M_G) sequences for static configuration are obtained by solving TOV equations for the same EoS sets. Increase in the pressure of any EoS will result in higher value of gravitational mass. For the cold NS the maximum masses are about $2.417 M_{solar}$ for np EoS whereas for npK EoS the maximum masses range from 2.372 to $2.142 M_{solar}$ with optical potential $U_{\bar{K}}$ = -60 to -150 MeV respectively. We plotted gravitational

mass vs baryon density for finite entropy density also. In this plot we observed that higher the entropy of the EoS, more is the gravitational mass because of the thermal pressure. We have summarised the maximum mass values for np and npK EoS in a table covering a range of total entropy from 0 to $7M_{solar}$ as well as the entire range of $U_{\bar{K}}$. To understand the softness of the EoS in the presence of thermal kaons and the K^- condensates we plotted the particle population density for a low entropy density and a high entropy density star. The threshold density for the kaons are tabulated for a clear comparison. For a lower entropy star, the threshold density of K^- condensates is low, which is further lowered for a deeper $U_{\bar{K}}$. However, for a star with higher entropy density K^- condensation does not occur at all in the core of the NS owing because of the appearance of thermal kaons at a low density of $\sim 0.09n_0$. We also study the temperature profile of the star at different entropy densities and observe that thermal pressure of NS at higher specific entropy is more than NS with lower specific entropy. For a finite entropy density star the temperature rises from the surface and can reach 50 -150 MeV at the core depending upon the value of entropy density. Another interesting observation was the higher value of core temperature in the np matter compared to npK. For lower entropy density star the core temperature is more for npK matter.

In the second part of the chapter the effect of uniform rotation on the NS is studied extensively for np and npK matter and at different entropy densities. For this we use the numerical library LORENE. A rotating star can support more mass compared to a static one. Also a NS with total entropy $7M_{solar}$ can support a maximum mass star which is more massive than that with total entropy $3M_{solar}$. The difference is independent of its angular momentum. However, we notice that the relative increase in NS mass from a lower J to higher J state is higher for a NS with lower total entropy. Next we draw the iso-contours of fluid energy density to study the equilibrium configurations of the stars in the presence of antikaons. As the star rotates fast, the spherical symmetry is broken. The deformation is maximum for a star rotating near its keplerian frequency. We also notice the deformation is more for higher entropy stars owing to its less dense core.

Finally we estimate the gravitational wave amplitude of a NS with a high magnetic field, which is not aligned with its rotation axis. The amplitude is more for a higher entropy star, still not within the limit of present generation detectors.

NS mergers can be observed using multi-messenger astronomy, astrophysical observations from the multimessenger astronomy provides rich information about fundamental physics. One of the possibilities of NS merger is a differentially rotating hot hypermassive neutron star. The stability of the merger remnant depends crucially on the underlying EoS and thus provides a method to probe the nature of dense matter in NSs. In chapter 4 we investigated signatures of strangeness containing constituents of the NS interior(such as hyperons or antikaon condensates) on the stability of the NS merger remnant. Further, in chapter 3 we have seen high temperatures (> 50

MeV) can be reached in the core of NS, implying that thermal effects on the EoS cannot be ignored. We consider zero-temperature($s = 0$) as well as finite temperature($s = 2$) EoSs based on the phenomenological Relativistic Mean Field(RMF) with density-dependent coefficients.

Here we again used numerical relativity software called Lorene for obtaining equilibrium sequences of differentially rotating NS for different EoS's (i) pure nucleonic matter (np)(ii) matter with λ-hyperons (np$\Lambda\varphi$) (iii) matter with antikaon condensates (npK). Using Lorene we constructed equilibrium sequences for nucleonic EoS for nonrotating and mass-shedding limits of uniformly rotating NSs and differentially rotating NSs obeying j-constant rotation law defined by the velocity profile, $F(\Omega) = R_0^2\,(\Omega_c - \Omega)$ at different degrees of differential rotation represented by the parameter $a = R_e/R_0$. We plot various equilibrium sequences for stars at constant angular momenta with a=0.2. We see the maximum gravitational masses increase from static to rotating stars. For comparison we also plot the uniformly rotating sequence and find that a differentially rotating star can accommodate more mass compared to its static counterpart (M_{TOV}). We do the same exercise for the strange EoS as well and summarise the findings for the three different EoS in tabular form. The np EoS not only can support a massive star, it can also rotate at a faster speed (keplerian) compared to the stars with strange constituents. Hence they are the most deformed of the three. From these sequences we determined the "Turning points" of the differentially rotating stars, i.e. the points on the equilibrium sequence from where NS enters unstable region. Using these turning points we obtained universal relation between $M_{max,dr}/M_{TOV}$ and $j/j_{max,a}$, which can expressed in mathematical form as $M_{max,dr}/M_{TOV} = 1 + b_1(a)(j/j_{max,a})^2 + b_2(a)(j/j_{max,a})^4$. Using this equation we calculated maximum mass of differentially rotating cold(hot)NS. We got two distinct universal curves for the cold and hot stars, the maximum mass supported by them being $1.23M_{TOV}$($1.19M_{TOV}$ respectively). The fitted curves are independent of the constituents of the NS and also do not change with the degree of differential rotation.

We generated the keplerian sequences for the differential rotation. However, this was numerically challenging and we could obtain up to a=0.3 only, larger degrees of differential rotation produced uncertainties in the results. We compared the ratio of normalised angular momenta for differentially to uniformly rotating stars as a function of 'a' for np EoS, both cold and hot. Finally in Chapter 4, we calculated the collapse time of the hypermassive neutron stars merger remnant (HMNS). Following the latest observation of GW170817, it is believed that the unstable HMNS, whose mass is estimated to be $2.74M_{solar}$ might be stable against collapse by differential rotation and thermal effect. We calculate the threshold mass for prompt collapse in units of M_{TOV} and collapse time (in milliseconds) of the HMNS for various initial masses of the coalescing NS.

Chapter 6

Future Perspective

In Chapter 3, we estimate the GW amplitude $h_0 \sim 9.3 \times 10^{-30}$ for a uniformly rotating cold NS (T= 0 MeV) that increases marginally to 1.09×10^{-29} for hot NS with $s = 1$ and 4.18×10^{-27} for NS with $s = 4$. From the sensitivity curve of the present day detectors [119], it can be seen that the possibility of detecting a GW of this amplitude is severely limited. VIRGO and aLIGO, for example, have the range from about 10 Hz to a few kHz and the characteristic strain window of $\sim 10^{-22}$ to few times 10^{-24}. The next generation of ground based interferometers such as the Einstein Telescope are predicted to have a sensitivity that will bring down the characteristic strain down to about a few times 10^{-25} [119]. Our calculations assume a rigidly rotating NS that is made of incompressible fluid and that has a uniform magnetic field inside the star. Relaxing these assumptions may lead to a greater value of ellipticity and hence a higher GW amplitude, which will have a high probability of being detected by the future generation of GW interferometers.

On the other hand, many studies of CCSN simulations of PNS evolution have shown that during the early phase of PNS evolution after core collapse, the GWs are emitted via quasi normal modes and are expected to have frequencies of about a kHz and amplitude that lies well within the range of ground based detectors [120, 121, 122, 123]. Also, many multidimensional CCSN simulations [124, 125] have shown g-modes as an important imprint of PNS oscillations in the early stages after bounce. The GW emitted as a result are expected to be about a few hundred Hz in frequency [126] having amplitude that should be in the grasp of current and upcoming GW observatories. However, CCSN explosion is a rare event, for example, in our galaxy it happens at the rate of about two to three times per century. It has also been shown by numerical simulations that short-lived but supra-massive neutron stars can be formed by the coalescence of low compactness NS of nearly equal mass [127]. These rapidly rotating and highly non-axisymmetric products of merger are supported by differential rotation and would emit quasi-periodic GW with typical frequencies of about 2-3 kHz with substantially higher

amplitude[106, 40]. Simulations have shown that up to $0.01M_{solar}$ could be radiated in GW via this mechanism [121]. We intend to study these scenarios in future.

The simultaneous detection of both gravitational waves (GW) and electromagnetic (EM) signals originating from the merger of binary neutron stars (NS-NS) by Ligo/Virgo collaboration has opened a new door for multi-messenger astronomy. These systems had been hypothesized as progenitors of the same central engines that power short-hard gamma-ray bursts (sGRBs). This line of thought is supported by the first detection of a Kilonova associated with the sGRB "GRB130603B". The support for this hypothesis comes from the incipient jet launch from the suitably magnetized NS, in the Magneto-hydrodynamic Simulations of Binary Neutron Star Mergers in General Relativity(GRMHD). Nevertheless, the detection of GW170817 coincident with a sGRB(event GRB170817A), as well as its association with Kilonova, indicate that some sGRBs are indeed powered by NS-NS mergers. It has been suggested that binary neutron star mergers can create highly magnetized, millisecond NSs.

This thesis explores the properties of rotating, hot NS. In future we would like to include the effect of magnetic field to understand the properties of HMNS remnants. Observations indicate that the magnetic field on NS ranges from 10^8 G in millisecond pulsars to 10^{15} G in magnetars. Magnetic field plays an important role by accelerating particles and channelising the accretion flows. It is believed to be one of the main mechanism to account the angular momentum loss in pulsars. The electromagnetic field and magnetization modify the energy–momentum tensor, breaking the spherical symmetry of the star and resulting in an anisotropy. However, it was reported by many authors that the magnetic field does not modify the EoS or as a matter of fact the macroscopic parameters of the NS.

NS can be classified into Rotation Powered Pulsars, Accretion Powered Pulsars and Internal Energy Powered Neutron Stars according to the nature of their energy generation processes. Over the years, many research groups are trying to links these different observational classes through unique evolutionary pathways. Thus, evolution of magnetic field study is crucial towards finding a unified scheme.

We have successfully used the library LORENE through out the thesis, where Poisson-like partial differential equations appearing in the Einstein–Maxwell system have been solved using spectral methods. New magnetization terms modify these equations when magnetic field is considered. We can continue our investigations with LORENE for (i)Magnetized NS with non-magnetized EoS, (ii)Magnetized NS with magnetized EoS but no magnetisation and (iii)Magnetized NS with magnetized EoS including magnetisation, for static as well as a rotating star. This can be followed by studying the evolution of magnetic field, that should conform to the observational facts- a relatively little decay of magnetic field in isolated radio pulsar, and dramatic reduction the surface magnetic field strength by several orders of magnitude in the binary accretion phase. There are several well-developed evolution formalism of NS magnetic fields, e.g., the Ohmic

dissipation, Hall-drift effect, screening by diamagnetism of accreting matter, and accretion flow to cause the decay of the magnetic field. The evolutionary pathways would definitely enrich our understanding about magnetic field formation, structure and evolution. The advent of multi-messenger astronomy and future telescopes with better sensitivity and wider frequency coverage will definitely facilitate the quest.

Bibliography

[1] W. Baade and F. Zwicky. "Remarks on super-novae and cosmic rays". *Physical Review* 46.1 (1934), p. 76.

[2] T. Gold. "Rotating neutron stars as the origin of the pulsating radio sources". *Nature* 218.5143 (1968), p. 731.

[3] G. Baym, C. Pethick, and P. Sutherland. "The ground state of matter at high densities: equation of state and stellar models". *The Astrophysical Journal* 170 (1971), p. 299.

[4] D. Bandyopadhyay. "Neutron Stars: Laboratories for fundamental physics under extreme astrophysical conditions". *Journal of Astrophysics and Astronomy* 38.3 (2017), p. 37.

[5] M. Hempel and J. Schaffner-Bielich. "A statistical model for a complete supernova equation of state". *Nuclear Physics A* 837.3-4 (2010), pp. 210–254.

[6] V. A. Ambartsumyan and G. S. Saakyan. "The degenerate superdense gas of elementary particles". *Soviet Astronomy* 4 (1960), p. 187.

[7] P. B. Demorest, T. Pennucci, S. M. Ransom, M. S. E. Roberts, and J. W. T. Hessels. "A two-solar-mass neutron star measured using Shapiro delay". *Nature* 467.7319 (2010), p. 1081.

[8] J. Antoniadis, P. C. C. Freire, N. Wex, T. M. Tauris, R. S. Lynch, M. H. van Kerkwijk, M. Kramer, C. Bassa, V. S. Dhillon, T. Driebe, et al. "A massive pulsar in a compact relativistic binary". *Science* 340.6131 (2013), p. 1233232.

[9] S. Weissenborn, D. Chatterjee, and J. Schaffner-Bielich. "Hyperons and massive neutron stars: The role of hyperon potentials". *Nuclear Physics A* 881 (2012), pp. 62–77.

[10] V. Dexheimer and S. Schramm. "Proto-neutron and neutron stars in a chiral SU (3) model". *The Astrophysical Journal* 683.2 (2008), p. 943.

[11] I. Bednarek, P. Haensel, J. L. Zdunik, M. Bejger, and R. Mańka. "Hyperons in neutron-star cores and a 2 M pulsar". *Astronomy & Astrophysics* 543 (2012), A157.

[12] L. Lopes and D. Menezes. "Hyperon threshold and stellar radii". *Journal of Cosmology and Astroparticle Physics* 2018.05 (2018), p. 038.

[13] M. Oertel, C. Providência, F. Gulminelli, and Ad. R. Raduta. "Hyperons in neutron star matter within relativistic mean-field models". *Journal of Physics G: Nuclear and Particle Physics* 42.7 (2015), p. 075202.

[14] K. A. Maslov, E. E. Kolomeitsev, and D. N. Voskresensky. "Solution of the hyperon puzzle within a relativistic mean-field model". *Physics Letters B* 748 (2015), pp. 369–375.

[15] P. Char and S. Banik. "Massive neutron stars with antikaon condensates in a density-dependent hadron field theory". *Physical Review C* 90.1 (2014), p. 015801.

[16] Y. Yamamoto, T. Furumoto, N. Yasutake, and Th. A. Rijken. "Multi-Pomeron repulsion and the neutron-star mass". *Physical Review C* 88.2 (2013), p. 022801.

[17] D. B. Kaplan and A. E. Nelson. "Strange goings on in dense nucleonic matter". *Physics Letters B* 175.1 (1986), pp. 57–63.

[18] M Prakash, I Bombaci, Manju Prakash, P J Ellis, J M Lattimer, and R Knorren. "Composition and structure of protoneutron stars". *Physics Reports* 280.1 (1997), pp. 1–77.

[19] S. Banik and D. Bandyopadhyay. "Third family of superdense stars in the presence of antikaon condensates". *Physical Review C* 64.5 (2001), p. 055805.

[20] S. Banik and D. Bandyopadhyay. "Antikaon condensation and the metastability of protoneutron stars". *Physical Review C* 63.3 (2001), p. 035802.

[21] J. O. Goussard, P. Haensel, and J. L. Zdunik. "Rapid differential rotation of protoneutron stars and constraints on radio pulsars periods". *Astron. Astrophys* 330 (1998).

[22] C. D. Ott, A. Burrows, T. A. Thompson, E. Livne, and R. Walder. "The spin periods and rotational profiles of neutron stars at birth". *The Astrophysical Journal Supplement Series* 164.1 (2006), p. 130.

[23] N. D. Lyford, T. W. Baumgarte, and S. L. Shapiro. "Effects of differential rotation on the maximum mass of neutron stars". *The Astrophysical Journal* 583.1 (2003), p. 410.

[24] J. L. Friedman and N. Stergioulas. *Rotating relativistic stars*. Cambridge University Press, 2013.

[25] G. B. Cook, S. L. Shapiro, and S. A. Teukolsky. "Spin-up of a rapidly rotating star by angular momentum loss-Effects of general relativity". *The Astrophysical Journal* 398 (1992), pp. 203–223.

[26] G. B. Cook, S. L. Shapiro, and S. A. Teukolsky. "Rapidly rotating polytropes in general relativity". *The Astrophysical Journal* 422 (1994), pp. 227–242.

[27] S. S. Lenka, P. Char, and S. Banik. "Critical mass, moment of inertia and universal relations of rapidly rotating neutron stars with exotic matter". *International Journal of Modern Physics D* 26.11 (2017), p. 1750127.

[28] A. Hewish, S. J. Bell, J. D. H. Pilkington, P. F. Scott, and R. A. Collins. "Observation of a rapidly pulsating radio source". *Nature* 217.5130 (1968), p. 709.

[29] R. N. Manchester, G. B. Hobbs, A. Teoh, and M. Hobbs. "VizieR Online Data Catalog: ATNF Pulsar Catalogue (Manchester+, 2005)". *VizieR Online Data Catalog* 1 (2016).

[30] A. G. Lyne, R. N. Manchester, D. R. Lorimer, M. Bailes, N. D'Amico, T. M. Tauris, S. Johnston, J. F. Bell, and L. Nicastro. "The Parkes southern pulsar survey—II. Final results and population analysis". *Monthly Notices of the Royal Astronomical Society* 295.4 (1998), pp. 743–755.

[31] L. Burderi, F. D'Antona, T. di Salvo, and A. Riggio. "Evolution of binary millisecond pulsars with light companions: the case of PSR J1748-2446ad". *COSP* 36 (2006), p. 1812.

[32] E. Fonseca, T. T. Pennucci, J. A. Ellis, I. H. Stairs, D. J. Nice, S. M. Ransom, P. B. Demorest, Z. Arzoumanian, K. Crowter, T. Dolch, et al. "The NANOGrav nine-year data set: Mass and geometric measurements of binary millisecond pulsars". *The Astrophysical Journal* 832.2 (2016), p. 167.

[33] G. Raaijmakers, T. E. Riley, A. L. Watts, S. K. Greif, S. M. Morsink, K. Hebeler, A. Schwenk, T. Hinderer, S. Nissanke, S. Guillot, et al. "A NICER view of PSR J0030+ 0451: Implications for the dense matter equation of state". *The Astrophysical Journal Letters* 887.1 (2019), p. L22.

[34] C. A. Raithel, F. Özel, and D. Psaltis. "Model-independent inference of neutron star radii from moment of inertia measurements". *Physical Review C* 93.3 (2016), p. 032801.

[35] B. P. Abbott, R. Abbott, T. D. Abbott, F. Acernese, K. Ackley, C. Adams, T. Adams, P. Addesso, R. Adhikari, V. B. Adya, et al. "GW170817: observation of gravitational waves from a binary neutron star inspiral". *Physical Review Letters* 119.16 (2017), p. 161101.

[36] LIGO Scientific Collaboration et al. "GW190425: observation of a compact binary coalescence with total mass $\sim 3.4 M_{\odot}$". *Astrophysical Journal Letters* 892.1 (2020), p. L3.

[37] D. Bandyopadhyay and D. Chatterjee. "Bulk viscosity of strange matter and r-modes in neutron stars". *Proceedings of 10th Symposium on Nuclei in the Cosmos*. Vol. 53. SISSA Medialab. 2008, p. 181.

[38] B. P. Abbott, R. Abbott, T. D. Abbott, F. Acernese, K. Ackley, C. Adams, T. Adams, P. Addesso, R. Adhikari, V. B. Adya, et al. "Search for gravitational waves from a long-lived remnant of the binary neutron star merger GW170817". *The Astrophysical Journal* 875.2 (2019), p. 160.

[39] B. P. Abbott, R. Abbott, T. D. Abbott, S. Abraham, F. Acernese, K. Ackley, C. Adams, R. X. Adhikari, V. B. Adya, C. Affeldt, et al. "GWTC-1: A gravitational-wave transient catalog of compact binary mergers observed by LIGO and Virgo during the first and second observing runs". *Physical Review X* 9.3 (2019), p. 031040.

[40] L. Baiotti and L. Rezzolla. "Binary neutron star mergers: a review of Einstein's richest laboratory". *Reports on Progress in Physics* 80.9 (2017), p. 096901.

[41] T. W. Baumgarte, S. L. Shapiro, and M Shibata. "On the maximum mass of differentially rotating neutron stars". *The Astrophysical Journal Letters* 528.1 (1999), p. L29.

[42] D. Gondek-Rosińska, I. Kowalska, L. Villain, M. Ansorg, and M. Kucaba. "A new view on the maximum mass of differentially rotating neutron stars". *The Astrophysical Journal* 837.1 (2017), p. 58.

[43] J. L. Friedman, J. R. Ipser, and R. D. Sorkin. "Turning-point method for axisymmetric stability of rotating relativistic stars". *The Astrophysical Journal* 325 (1988), pp. 722–724.

[44] M. Ansorg, D. Gondek-Rosińska, and L. Villain. "On the solution space of differentially rotating neutron stars in general relativity". *Monthly Notices of the Royal Astronomical Society* 396.4 (2009), pp. 2359–2366.

[45] L. R. Weih, E. R. Most, and L. Rezzolla. "On the stability and maximum mass of differentially rotating relativistic stars". *Monthly Notices of the Royal Astronomical Society: Letters* 473.1 (2018), pp. L126–L130.

[46] C. Breu and L. Rezzolla. "Maximum mass, moment of inertia and compactness of relativistic stars". *Monthly Notices of the Royal Astronomical Society* 459.1 (2016), pp. 646–656.

[47] S. S. Lenka, P. Char, and S Banik. "Properties of massive rotating protoneutron stars with hyperons: evolution and universality". *Journal of Physics G: Nuclear and Particle Physics* 46.10 (2019), p. 105201.

[48] M. Lucca and L. Sagunski. "The lifetime of binary neutron star merger remnants". *Journal of High Energy Astrophysics* 27 (2020), pp. 33–37.

[49] J. D. Walecka. "Theoretical nuclear and subnuclear physics". *World Scientific* (2004), pp. 1–628.

[50] B. D. Serot and J. D. Walecka. "The Relativistic Nuclear Many-Body Problem". *Advances in Nuclear Physics, edited by J. W. Negele and E. Vogt, Plenum Press, New York* 16 (1986).

[51] N. K. Glendenning. *"Compact stars: Nuclear Physics, Particle Physics and General Relativity"*. Springer-Verlag New York, 1997.

[52] S. Banik and D. Bandyopadhyay. "Density dependent hadron field theory for neutron stars with antikaon condensates". *Physical Review C* 66.6 (2002), p. 065801.

[53] S. Typel. "Relativistic model for nuclear matter and atomic nuclei with momentum-dependent self-energies". *Physical Review C* 71.6 (2005), p. 064301.

[54] S. Typel, G. Röpke, T. Klähn, D. Blaschke, and H. H. Wolter. "Composition and thermodynamics of nuclear matter with light clusters". *Physical Review C* 81.1 (2010), p. 015803.

[55] C. Fuchs, H. Lenske, and H. H. Wolter. "Density dependent hadron field theory". *Physical Review C* 52.6 (1995), p. 3043.

[56] H. Lenske and C. Fuchs. "Rearrangement in the density dependent relativistic field theory of nuclei". *Physics Letters B* 345.4 (1995), pp. 355–360.

[57] T. Fischer, M. Hempel, I. Sagert, Y. Suwa, and J. Schaffner-Bielich. "Symmetry energy impact in simulations of core-collapse supernovae". *The European physical journal A* 50.2 (2014), p. 46.

[58] J. M. Lattimer and Y. Lim. "Constraining the symmetry parameters of the nuclear interaction". *The Astrophysical Journal* 771.1 (2013), p. 51.

[59] J. O. Goussard, P. Haensel, and J. L. Zdunik. "Rapid uniform rotation of protoneutron stars". *Astron. Astrophys* 321 (1997), pp. 822–834.

[60] S. Bonazzola, E. Gourgoulhon, M. Salgado, and J. A. Marck. "Axisymmetric rotating relativistic bodies: A new numerical approach for'exact'solutions". *Astronomy and Astrophysics* 278 (1993), pp. 421–443.

[61] J. Schaffner and I. N. Mishustin. "Hyperon-rich matter in neutron stars". *Physical Review C* 53.3 (1996), p. 1416.

[62] J. Schaffner, C. B. Dover, A. Gal, C. Greiner, D. J. Millener, and H. Stöcker. "Multiply strange nuclear systems". *Annals of Physics* 235.1 (1994), pp. 35–76.

[63] S. Typel and H. H. Wolter. "Relativistic mean field calculations with density-dependent meson-nucleon coupling". *Nuclear Physics A* 656.3-4 (1999), pp. 331–364.

[64] J. A. Pons, S. Reddy, P. J. Ellis, M. Prakash, and J. M. Lattimer. "Kaon condensation in proto-neutron star matter". *Physical Review C* 62.3 (2000), p. 035803.

[65] N. K. Glendenning and J. Schaffner-Bielich. "First order kaon condensate". *Physical Review C* 60.2 (1999), p. 025803.

[66] S. Banik, M. Hempel, and D. Bandyopadhyay. "New Hyperon Equations of State for Supernovae and Neutron Stars in Density-dependent Hadron Field Theory". *The Astrophysical Journal Supplement Series* 214.2 (2014), p. 22.

[67] M. Marques, M. Oertel, M. Hempel, and J. Novak. "New temperature dependent hyperonic equation of state: Application to rotating neutron star models and I- Q relations". *Physical Review C* 96.4 (2017), p. 045806.

[68] M. Fortin, C. Providência, Ad. R. Raduta, F. Gulminelli, J. L. Zdunik, P Haensel, and M Bejger. "Neutron star radii and crusts: uncertainties and unified equations of state". *Physical Review C* 94.3 (2016), p. 035804.

[69] C. B. Dover and A. Gal. "Hyperon-nucleus potentials". *Progress in Particle and Nuclear Physics* 12 (1984), pp. 171–239.

[70] R. E. Chrien and C. B. Dover. "Nuclear systems with strangeness". *Annual Review of Nuclear and Particle Science* 39.1 (1989), pp. 113–150.

[71] V. K. Magas, J. Yamagata-Sekihara, S. Hirenzaki, E. Oset, and A. Ramos. "Latest results for the antikaon-nucleon optical potential". *Few-Body Systems* 50.1-4 (2011), pp. 343–345.

[72] R. C. Tolman. "Static solutions of Einstein's field equations for spheres of fluid". *Physical Review* 55.4 (1939), p. 364.

[73] J. R. Oppenheimer and G. M. Volkoff. "On massive neutron cores". *Physical Review* 55.4 (1939), p. 374.

[74] J. A. Wheeler. "Geometrodynamics and the issue of the final state". *Relativity, Groups and Topology,* ed. by DeWitt C. DeWitt B. Gordon and Breach, New York, 1964, pp. 317–522. DOI: 10.1063/1.3047166.

[75] M. Alcubierre. *Introduction to 3+ 1 numerical relativity.* Vol. 140. Oxford University Press, 2008.

[76] E. Gourgoulhon. *3+ 1 formalism in general relativity: bases of numerical relativity.* Vol. 846. Springer Berlin, Heidelberg, 2012.

[77] A. Papapetrou. "Champs gravitationnels stationnaires à symétrie axiale". *Annales de l'IHP Physique théorique.* Vol. 4. 2. 1966, pp. 83–105.

[78] W. Kundt and M. Trümper. "Orthogonal decomposition of axi-symmetric stationary spacetimes". *Zeitschrift für Physik A Hadrons and nuclei* 192.4 (1966), pp. 419–422.

[79] B. Carter. "Killing horizons and orthogonally transitive groups in space-time". *Journal of Mathematical Physics* 10.1 (1969), pp. 70–81.

[80] B. Carter. "The commutation property of a stationary, axisymmetric system". *Communications in Mathematical Physics* 17.3 (1970), pp. 233–238.

[81] B. Carter. "Black hole equilibrium states". *General Relativity and Gravitation* 41.12 (2009), p. 2873.

[82] E. Gourgoulhon. "An introduction to the theory of rotating relativistic stars". *arXiv:1003.5015* (2010).

[83] M. Salgado, S. Bonazzola, E. Gourgoulhon, and P. Haensel. "High precision rotating neutron star models 1: Analysis of neutron star properties". *Astronomy and Astrophysics* 291 (1994), pp. 155–170.

[84] G. Pappas and T. A. Apostolatos. "Revising the multipole moments of numerical spacetimes and its consequences". *Physical Review Letters* 108.23 (2012), p. 231104.

[85] L. B. Szabados. "Quasi-local energy-momentum and angular momentum in general relativity". *Living Reviews in Relativity* 12.1 (2009), p. 4.

[86] J. B. Hartle and K. S. Thorne. "Slowly rotating relativistic stars. II. Models for neutron stars and supermassive stars". *The Astrophysical Journal* 153 (1968), p. 807.

[87] R. Arnowitt, S. Deser, and C. W. Misner. "The dynamics of general relativity". *General Relativity and Gravitation* 40.9 (2008), pp. 1997–2027.

[88] E. Gourgoulhon and S. Bonazzola. "A formulation of the virial theorem in general relativity". *Classical and Quantum Gravity* 11.2 (1994), p. 443.

[89] S. Bonazzola. "The virial theorem in general relativity". *The Astrophysical Journal* 182 (1973), pp. 335–340.

[90] M. Liebendörfer. "A simple parameterization of the consequences of deleptonization for simulations of stellar core collapse". *The Astrophysical Journal* 633.2 (2005), p. 1042.

[91] M. Prakash, I. Bombaci, M. Prakash, P. J. Ellis, J. M. Lattimer, and R. Knorren. "Composition and structure of protoneutron stars". *Physics Reports* 280.1 (1997), pp. 1–77.

[92] D. G. Yakovlev and K. P. Levenfish. "Modified URCA process in neutron star cores." *Astronomy and Astrophysics* 297 (1995), p. 717.

[93] C. Schaab, F. Weber, M. K. Weigel, and N. K. Glendenning. "Thermal evolution of compact stars". *Nuclear Physics A* 605.4 (1996), pp. 531–565.

[94] M. Hempel, T. Fischer, J. Schaffner-Bielich, and M. Liebendörfer. "New equations of state in simulations of core-collapse supernovae". *The Astrophysical Journal* 748.1 (2012), p. 70.

[95] W. Kastaun, R. Ciolfi, and B. Giacomazzo. "Structure of stable binary neutron star merger remnants: A case study". *Physical Review D* 94.4 (2016), p. 044060.

[96] B. Giacomazzo and R. Perna. "Formation of stable magnetars from binary neutron star mergers". *The Astrophysical Journal Letters* 771.2 (2013), p. L26.

[97] D. J. Price and S. Rosswog. "Producing ultrastrong magnetic fields in neutron star mergers". *Science* 312.5774 (2006), pp. 719–722.

[98] M. D. Duez, Y. T. Liu, S. L. Shapiro, M. Shibata, and B. C. Stephens. "Evolution of magnetized, differentially rotating neutron stars: Simulations in full general relativity". *Physical Review D* 73.10 (2006), p. 104015.

[99] S. Konar, M. Bagchi, D. Bandyopadhyay, S. Banik, D. Bhattacharya, S. Bhattacharyya, R. T. Gangadhara, A. Gopakumar, Y. Gupta, B. C. Joshi, et al. "Neutron Star Physics in the Square Kilometre Array Era: An Indian Perspective". *Journal of Astrophysics and Astronomy* 37.4 (2016), p. 36.

[100] R. D. Sorkin. "A Stability criterion for many parameter equilibrium families". *The Astrophysical Journal* 257 (1982), p. 847.

[101] S. Banik, W. Greiner, and D. Bandyopadhyay. "Critical temperature of antikaon condensation in nuclear matter". *Physical Review C* 78.6 (2008), p. 065804.

[102] J. A. Pons, S. Reddy, M. Prakash, J. M. Lattimer, and J. A. Miralles. "Evolution of proto-neutron stars". *The Astrophysical Journal* 513.2 (1999), p. 780.

[103] D. Chatterjee, T. Elghozi, J. Novak, and M. Oertel. "Consistent neutron star models with magnetic-field-dependent equations of state". *Monthly Notices of the Royal Astronomical Society* 447.4 (2015), pp. 3785–3796.

[104] B. Franzon, R. O. Gomes, and S. Schramm. "Effects of the quark-hadron phase transition on highly magnetized neutron stars". *Monthly Notices of the Royal Astronomical Society* 463.1 (2016), pp. 571–579.

[105] S. Bonazzola and E. Gourgoulhon. "Gravitational waves from pulsars: Emission by the magnetic field induced distortion". *Astronomy Astrophysics* 312 (1996), pp. 675–690.

[106] G. Bozzola, N. Stergioulas, and A. Bauswein. "Universal relations for differentially rotating relativistic stars at the threshold to collapse". *Monthly Notices of the Royal Astronomical Society* 474.3 (2018), pp. 3557–3564.

[107] R. Gill, A. Nathanail, and L. Rezzolla. "When Did the Remnant of GW170817 Collapse to a Black Hole?" *The Astrophysical Journal* 876.2 (2019), p. 139.

[108] S. Köppel, L. Bovard, and L. Rezzolla. "A general-relativistic determination of the threshold mass to prompt collapse in binary neutron star mergers". *The Astrophysical Journal Letters* 872.1 (2019), p. L16.

[109] D. Radice, A. Perego, K. Hotokezaka, S. A. Fromm, S. Bernuzzi, and L. F. Roberts. "Binary neutron star mergers: mass ejection, electromagnetic counterparts, and nucleosynthesis". *The Astrophysical Journal* 869.2 (2018), p. 130.

[110] H. Komatsu, Y. Eriguchi, and I. Hachisu. "Rapidly rotating general relativistic stars-I. Numerical method and its application to uniformly rotating polytropes". *Monthly Notices of the Royal Astronomical Society* 237.2 (1989), pp. 355–379.

[111] N. D. Batra, K. P. Nunna, and S. Banik. "Properties of rapidly rotating hot neutron stars with antikaon condensates at constant entropy per baryon". *Physical Review C* 98.3 (2018), p. 035801.

[112] V. Ravi and P. D. Lasky. "The birth of black holes: neutron star collapse times, gamma-ray bursts and fast radio bursts". *Monthly Notices of the Royal Astronomical Society* 441.3 (2014), pp. 2433–2439.

[113] S. Ai, H. Gao, Zi-Gao. Dai, Xue-Feng. Wu, A. Li, B. Zhang, and Mu-Zi. Li. "The allowed parameter space of a long-lived neutron star as the merger remnant of GW170817". *The Astrophysical Journal* 860.1 (2018), p. 57.

[114] H. Tong, C. Yu, and L. Huang. "A magnetically driven origin for the low luminosity GRB 170817A associated with GW170817". *Research in Astronomy and Astrophysics* 18.6 (2018), p. 067.

[115] P. D. Lasky, B. Haskell, V. Ravi, E. J. Howell, and D. M. Coward. "Nuclear equation of state from observations of short gamma-ray burst remnants". *Physical Review D* 89.4 (2014), p. 047302.

[116] L. Rezzolla and O. Zanotti. *Relativistic Hydrodynamics*. Oxford University Press, 2013.

[117] A. Bauswein, T. W. Baumgarte, and H. T. Janka. "Prompt merger collapse and the maximum mass of neutron stars". *Physical Review Letters* 111.13 (2013), p. 131101.

[118] A. Bauswein, O. Just, H. T. Janka, and N. Stergioulas. "Neutron-star radius constraints from GW170817 and future detections". *The Astrophysical Journal Letters* 850.2 (2017), p. L34.

[119] C. J. Moore, R. H. Cole, and C. P. L. Berry. "Gravitational-wave sensitivity curves". *Classical and Quantum Gravity* 32.1 (2014), p. 015014.

[120] Y. S. Shibata and Y Sekiguchi. "Gravitational waves from axisymmetric rotating stellar core collapse to a neutron star in full general relativity". *Physical Review D* 69.2 (2004), p. 084024.

[121] V. Ferrari, G. Miniutti, and J. A. Pons. "Gravitational waves from newly born, hot neutron stars". *Monthly Notices of the Royal Astronomical Society* 342.2 (2003), pp. 629–638.

[122] V. Morozova, D. Radice, A. Burrows, and D. Vartanyan. "The gravitational wave signal from core-collapse supernovae". *The Astrophysical Journal* 861.1 (2018), p. 10.

[123] G. Camelio, A. Lovato, L. Gualtieri, O. Benhar, J. A. Pons, and V. Ferrari. "Evolution of a proto-neutron star with a nuclear many-body equation of state: Neutrino luminosity and gravitational wave frequencies". *Physical Review D* 96.4 (2017), p. 043015.

[124] T. Foglizzo, R. Kazeroni, J. Guilet, F. Masset, M. González, B. K. Krueger, J. Novak, M. Oertel, J. Margueron, J. Faure, et al. "The explosion mechanism of core-collapse supernovae: progress in supernova theory and experiments". *Publications of the Astronomical Society of Australia* 32 (2015).

[125] H. T. Janka, T. Melson, and A. Summa. "Physics of core-collapse supernovae in three dimensions: a sneak preview". *Annual Review of Nuclear and Particle Science* 66 (2016), pp. 341–375.

[126] H. Sotani and T. Takiwaki. "Gravitational wave asteroseismology with protoneutron stars". *Physical Review D* 94.4 (2016), p. 044043.

[127] M. Shibata and K. Kiuchi. "Gravitational waves from remnant massive neutron stars of binary neutron star merger: Viscous hydrodynamics effects". *Physical Review D* 95.12 (2017), p. 123003.

List of Publications

For Thesis Work

1. Krishna Prakash Nunna, Sarmistha Banik, Debarati Chatterjee "Signatures of strangeness in neutron star merger remnants", The Astrophysical Journal, 896 (2020), P.109.

2. Neelam Dhanda Batra, Krishna Prakash Nunna and Sarmistha Banik, "Properties of Rapidly Rotating hot neutron stars with antikaon condensates at constant entropy per baryon", *Physical Review C* **98,** 035801, 2018**.**

Participation in Seminar and Workshops

1. Oral presentation on "Stability analysis of differentially rotating hot, hypermassive Neutron star merger remanant" during 38^{th} meeting of The Astronomical Society of India held at IISER Tirupati, India, February-2020.

2. Poster Presentation in Frontier in Particle Physics and Cosmology, at Univ. of Hyderabad, January, 2019.

3. Poster Presentation at the 30^{th} meeting of the Indian Association for General Relativity and Gravitation(IAGRG) on "Eras in Cosmology and Multi-messenger Astronomy" held at BITS-Pilani, Hyderabad, India, January-2019.

4. Attended 'Pulsar Astronomy with uGMRT Boot-Camp and Multi-wavelength Neutron Star' Workshop held at BITS-Pilani, Hyderabad Campus, India, January -2018.

5. Participated in 'National school on Gravitational waves', from December 2015 - January 2016, held at M A College of Engineering Kothamangalam, Kochi, India.

6. Attended General Relativity Centennial "1915-2015" December, 2015 at Jamia Milia Islamia University, New Delhi

7. Attended Winter School on Nuclear astrophysics held at VECC, Kolkata, India, January-2015.

Biography of KrishnaPrakash Nunna

Mr. Krishna Prakash Nunna completed his Bachelor of Technology (Electrical and Electronics Engineering) from Pondicherry University, Puducherry, India. He joined Departmnet of Physics, Birla Institute of Technology and Science-Pilani, Hyderabad Campus as Junior Reserach Fellow in SERB Funded project in the year 2014, to carry out his doctoral research work under the supervision of Prof. Sarmistha Banik. He presented his research work in different scientific conferences and attended various workshops related to his research area. Mr. Krishna Prakash has published his results in two highly reputed journals i.e., Physical Review C and The Astrophysical Journal. Finally, he was one of the key persons to successfully organise a national level workshop in 2018 at BITS-PILANI, Hyderabad Campus that was attended by the stalwarts of NS physics community from all over India.

Biography of Prof. Sarmistha Banik

Prof. Sarmistha Banik is presently working as an Associate Professor in the Department of Physics, Birla Institute of Technology and Science, Pilani, Hyderabad Campus. She has also been a visiting associate at the Inter-University Center for Astronomy & Astrophysics (IUCAA), Pune, India since 2015. She got PhD degree from Calcutta University and pursued her postdoctoral studies at School of Physics & Astronomy, University of Manchester, UK. Prof. Banik is an Alexander von Humboldt Fellow and worked as a guest scientist at Frankfurt Institute for Advanced Studies, Germany with Humboldt fellowship. She is involved in neutron star research for the last 20 years. She has published more than 30 research articles and delivered invited lectures at various national and international conferences. Prof. Banik has visited many reputed institutes in the world and established joint collaborations. Her small research group comprising of research scholars and postdoctoral fellows have successfully hosted national level workshop on neutron stars. Teaching physics is a passion that Prof. Banik takes a keen interest in.